Design, Fabrication and Process Modelling of a Near Field Electrospinning Test Bench

by

Victor CERDA-CARVAJAL

THESIS PRESENTED TO ÉCOLE DE TECHNOLOGIE SUPÉRIEURE IN PARTIAL FULFILLEMENT FOR A MASTER'S DEGREE WITH THESIS IN MECHANICAL ENGINEERING
M.A.Sc.

MONTREAL, JANUARY 15, 2020

ÉCOLE DE TECHNOLOGIE SUPÉRIEURE
UNIVERSITÉ DU QUÉBEC

BOARD OF EXAMINERS

THIS THESIS HAS BEEN EVALUATED

BY THE FOLLOWING BOARD OF EXAMINERS

Mrs. Nicole R. DEMARQUETTE, Thesis Supervisor
Department of Mechanical Engineering at École de Technologie Supérieure

Mr. Ricardo J. ZEDNIK, Thesis Co-supervisor
Department of Mechanical Engineering at École de Technologie Supérieure

Mr. Eric David, President of the Board of Examiners
Department of Mechanical Engineering at École de Technologie Supérieure

Mr. Luke Boyer
Carpenter Technology Corporation

THIS THESIS WAS PRENSENTED AND DEFENDED

IN THE PRESENCE OF A BOARD OF EXAMINERS AND PUBLIC

JANUARY 10 2020

AT ÉCOLE DE TECHNOLOGIE SUPÉRIEURE

ACKNOWLEDGMENT

I would like to start off by expressing my gratitude by giving my kindest regards to several people and institutions that have helped me through this project either it be by their resourcefulness or knowledge.

First and foremost, I would like to thank my advisor and co-advisor Nicole R. Demarquette and Ricardo J. Zednik respectively, for their support in this lengthy and complex project.

I also want to thank NSK as a sponsor for their generous contribution of linear motion components, for which this project would never have taken place without. I specially wish thank Mr. Sean Baron for believing in the project and giving me some valuable recommendations in the provided components that were chosen for the test bench.

Thanks to all the technical personnel at École de Technologie Supérieure, for their valuable insight in fabrication methods and techniques. To allow me to use the high-end equipment's this institute has to offer. To all my work colleagues that helped me resolve certain issues and supported me throughout these last years.

I would like to give a special thanks to Dr. Cesar M. Cerda, scientist and father. Without him I would not have been able to understand the intricacies of this field and for his most valuable knowledge in sorting out some of the most difficult aspects in the theoretical approach proposed in this thesis.

Last but not least, to my family, my mother and her husband. For their continued support and for always believing in me. I would also like to give a special thanks to a good friend of mine, Dominique Grogg, I hope that you found peace in a better world, I will always remember you.

Conception, fabrication et modélisation d'un banc d'essai d'électrofilage à champ rapproché

Victor CERDA-CARVAJAL

RÉSUMÉ

Ce mémoire présente la conception, fabrication et modélisation du procédé d'électrofilage à champ rapproché. Ayant comme mandat initial d'améliorer le placement de fibres produites par électrofilage, une analyse de l'état de l'art a été faite. Celle-ci a permis d'établir les requis machine ainsi que de dresser les lignes directrices liées à la conception du banc d'essai. L'objectif principal étant l'optimisation du procédé ainsi que la paramétrisation des variables machine.

Le banc d'essai final combine des composantes de haute précision tel que des roulements linéaires, vis à billes et paliers fournis par NSK. Également combiné à des composantes intermédiaires de haute précision, celui-ci propose aussi une plateforme versatile en termes de futurs développements. Ayant un fonctionnement similaire à une machine à commande numérique, les trajectoires sont pilotées par code g dans un environnement LABVIEW. Trois moteurs pas à pas sont combinés pour obtenir des déplacement linéaires (x-y-z). Intégrant un assemblage unique de contrôle du haut voltage, le champ électrique est focalisé à l'aide d'un système pointe à pointe.

Une modélisation complète a été faite pour évaluer de manière séparée, tous les phénomènes physiques. Tout le procédé est ramené à un modèle solide équivalent pour évaluer le régime permanent. Afin de simplifier certaines analyses, le fluide est considéré comme étant newtonien ainsi qu'à propriétés électriques constantes. Une solution aqueuse de 4% de PVA est utilisé sur toute la ligne. Ayant une permittivité relative près de celle de l'eau, ceci suppose que la majorité de forces agissant sur le fluide se situent à l'interface air-liquide. Ces forces incluent celles liées à la tension de surface, le champ électrostatique, viscosité du fluide et gravité quoique cette dernière joue un rôle secondaire. Une approche novatrice est utilisée pour l'estimation des forces visqueuses. Utilisant un modèle numérique de dynamique des fluides, des conditions frontières mobiles avec une vitesse tangentielle constante est imposée à la zone de transition du cône de Taylor ainsi que le jet produit. En variant les propriétés physiques et conditions aux frontières, une équation linéaire contenant la viscosité et vitesse en surface est obtenue pour estimer les forces visqueuses d'un cas spécifique.

Somme tout, les forces visqueuses représentent des forces négligeables (moins de 2%). Un modèle d'évaporation unique a été développé pour estimer la distance de solidification des fibres produites. Basé sur le modèle de Langmuir, une valeur approximative de 1mm est utilisée. Par la suite, une analyse par éléments fini utilisant un solveur simplifié, les équations de Maxwell sont réduites aux lois de Faraday et Gauss. Suite à la variation du potentiel électrique, une relation est établie entre la force électrostatique et le champ électrique produit. Par la combinaison de toutes les forces, liées par les équations prédictives mentionnées plus haut, les paramètres machines sont calculés. Ces paramètres étant : le débit, distance du

collecteur, vitesse et voltage appliqué. Quoique les fibres produites n'étaient pas organisées, la production de fibres a eu lieux très près des paramètres calculés.

Finalement, les observations, modèles numériques et banc d'essai fabriqué dans cet ouvrage, contribuent à une meilleure compréhension de la complexité du procédé d'électrofilage.

Mots-clés : Électrofilage, champ rapproché, banc d'essai, analyse par éléments finis, dynamique de fluides numérique, évaporation, modélisation, PVA

Design, fabrication and modeling of a near field electrospinning test bench

Victor CERDA-CARVAJAL

ABSTRACT

This thesis presents a full test bench design, process modelling and some experimental work on near-field electrospinning. With the original objective of precisely controlling fiber placement with the electrospinning technique, a full analysis of existing techniques was done. Findings revealed design parameters, guidelines and choice technology for a proposed test bench. The main focus being optimization and parametrisation of a near-field electrospinning (NFES) experimentation.

The final test bench design implements high precision components. Linear bearings, preloaded ball screws and associated pillow blocks were provided by NSK. Intermediate mounting structures and motors were sized accordingly to machine requirements. High precision drives were coupled to stepper motors to create a 3 stage (x-y-z axis) programmable deposition surface. A computer numerical control (CNC) g-code oriented interface was fully created in the LabVIEW environment. Coupled to this is a novel high voltage NFES design that has a needle to needle setup to focalise the electric field.

Full process was modeled by separating and evaluating each physical phenomenon. The overall process, when the fluid shape is in steady state, is simplified to an equivalent solid model. Only linear behaviors such as Newtonian fluid characteristics and constant electric properties were taken into account. A 4% PVA solution was used throughout. A high relative permittivity, in the present case is the majority of the acting forces are at the air-fluid interface. Main forces include: surface tension and electrostatic pull with viscous forces and gravity playing a secondary role. A novel approach was used to estimate viscous forces by using computational fluid dynamics (CFD). Using a moving boundary with a constant tangential speed applied to the transition zone of the Taylor cone all along the formed jet, emulating an electrostatic pull. By varying CFD conditions, a simple linear function was obtained with viscosity and surface speed as variables to estimate overall viscous forces for a specific case.

Overall, the viscous forces were so low (under 2%), that they are negligible for similar fluids and setups. A unique evaporation model was developed to estimate solidification distance based on the Langmuir model, which predicts a value of around 1mm of jet length. Finally, a finite element analysis (FEA) with a simplified electrostatic solver reduces the Maxwell equations to Gauss's and Faraday's law. A relationship between a resulting pulling force and an electric field for the unique high voltage geometry was determined. Combining all forces by a sum, machine controllable parameters were extracted. These parameters are: flow rate, collector distance, speed and voltage. Although fibers did not produce the desired patterns, within a few tries their production occurred.

The observations, numerical simulations and the apparatus made (developed) in this work contribute to a better understanding of the complexity of the electrospinning processes.

Key-words: Near Field electrospinning, Test bench, Finite element analysis, computational fluid dynamics, Evaporation, Modeling, PVA

TABLE OF CONTENTS

Page

LIST OF TABLES

Page

LIST OF FIGURES

Page

LIST OF ABREVIATIONS

CAD	Computer assisted design
CAM	Computer assisted manufacturing
CFD	Computational fluid dynamics
CNC	Computer numerical control
FEA	Finite element analysis
G-Code	General-Code
NFES	Near-Field electrospinning
PEO	Polyehtylene oxide
PVA	Polyvinyl alcool
PVDF	Polyvinylidene fluoride
SEM	Scanning electron microscope

LIST OF SYMBOLS

γ	Surface tension of polymer solution
$\vec{F}_{es}$	Resulting force related to electrostatic pull
$\vec{F}_{esC}$	Electrostatic pulling force with charged dispensing needle
$\vec{F}_{esG}$	Electrostatic pulling force with charged dispensing needle
$\vec{F}_{g}$	Resulting force related to gravity
$\vec{F}_{\gamma 1}$	Resulting force related to surface tension at the taylor cone end
$\vec{F}_{\gamma 2}$	Resulting force related to surface tension from jet-collector end
$\vec{F}_{\mu}$	Resulting force related to viscous forces
$\vec{D}$	Electric displacement field
D_{min}	Minimum dielectric distance
$\vec{E}$	Electric field
E_f	Electric field
$\vec{P}$	Polarisation field
P_p	Water partial pressure
P_v	Water vapor pressure
R_{fiber}	Radius of produced fiber
V_c	Critical voltage
$\vec{V_s}$	Surface velocity
$\vec{g}$	Gravity field
$\vec{v}$	Velocity field
v_r	Radial velocity component

v_x	x direction velocity component
ε_0	Free space permittivity
θ_T	Angle of Taylor cone
μ_r	Viscosity
$\bar{\bar{\tau}}$	Stress tensor (Navier-stokes)
χ_e	Electric susceptibility
a	Activity coefficient
H	Computer numerical control
k	Boltzmann constant
L	Needle to collector length
m	Molecular mass
P	Electrostatic pulling force (Taylor notation)
R	Dispensing needle radius
R	Ideal gas constant
T	Temperature
V	Applied voltage
w	Surface mobile charge fraction
Γ	Surface excess of solute
I	Unit tensor
M	Quantity of vapor molecules
r	r direction or evaluated radius position
t	Time
x	x direction or evaluated x position
ε	Solution relative permittivity

μ	viscosity
ρ	Density of solution

INTRODUCTION

Electrospinning is a technique that was patented in the beginning of the 20th century by J.F. Cooley (US692631). The theoretical aspect came in 1969 with Sir G.I. Taylor's paper, 'Electrically driven jets' (Taylor, 1969). Until recently the very similar technique, electrospraying, was the most popular. The first technique, being able to produce sub-micron sized jets was never really exploited due to its limited application at the time. The second method gathered more interest because of the broad range of spraying and coating applications. Lately, by the end of the 1990s, electrospinning gained a lot of interest due to advances in polymers and their applications. A recent analysis in historical trends (Nascimento et al. 2015) would suggest a nearly non-existent (pre-2000) electrospinning title match on Scopus to nearly 3500 by the year 2013 for related publications.

In an effort to provide an opening in this field, ÉTS's industrial research chair" Thermoplastic blends and nanocomposites", held by Professor Nicole Demarquette. was searching for a method to produce polymer nanofibers in a controllable fashion.

First and foremost, the technique consists of producing an electric field that pulls the fluid, which is usually a polymer solution. A simplified electrospinning setup (Figure 0.1), shows an applied voltage between a dispensing needle and a grounded collector plate creating an electrostatic force on a polymer solution. We notice two different types of flow and fiber formation: the fluidic portion (blue) being linear and somewhat predictable and the solidified portion which is, a randomly oriented polymer fiber (red).

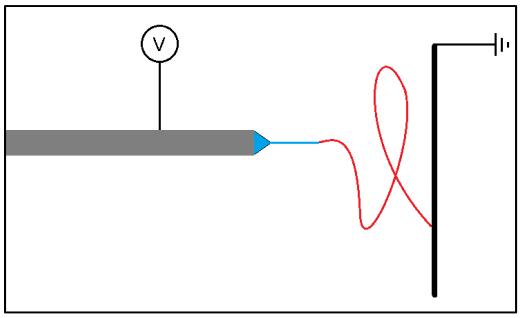

Figure 0.1: Simplified electrospinning setup

The main issue occurs when the polymer solution solidifies; it loses its carrier (solvent) due to evaporation. This significantly reduces the acting distributed electrostatic force that pulls the fluid due to the dielectric nature of most polymers. Once solidification sets in, the fiber spirals randomly onto the collector which is usually a grounded conductive plate (Figure 0.1). It is generally accepted that fibers tend to repel each other due to residual charges left in the polymer which tends to even out fiber spreading. The produced fiber mat will have a random orientation making any sort of subsequent and consistent characterization very difficult (fiber orientation, uneven spacing, thickness and fiber diameter). One step into improving fiber orientation is the use of different collector geometries and shapes. A common method used includes a rotating collector drum that spool fibers.

A logical step forward, in order to obtain precise fiber placement, is to avoid the chaotic portion of the process. In other words, catching the fiber at the phase transition (liquid-solid) allows for a more predictable result. Given the pulling nature of the solidified portion of the process or the rotating drum's turning speed, a substitution for this effect is desired so that not only a mechanical pull is added but also to create fibres that don't pile up. A great substitute, is a moving collector that allows for a 3D printing like process. This last iteration is called near-field electrospinning and represents some of the latest advancements of the electrospinning technique and is also the main focus of this master's project.

Given the previous information, the objective of this project is to design and build a test bench with all variants integrated into a flexible platform. It can accommodate most variants and also

monitor other variables which are rarely taken into account, such as atmospheric pressure and temperature.

A full overview of the mechanical system is done with all dependencies and motion parameters determined in order to carefully select actuators, sensors and electrical components. In parallel to this, a user interface and software platform was chosen to precisely control experimental parameters. In this case, a National Instruments control card was selected and full interface was programmed with a reliable g-code oriented trajectory system. Similar to a CNC machine, this test bench runs standardized file formats with some function equivalences to control different parameters (e.g. precise voltage initiation). Furthermore, a full rundown of available technologies is done in order to properly choose components according to the design criteria. Most specifications are based on data available in the literature. The sizing and overall design respects all determined criteria and every layout decision is either based on functional parameters or done in order to minimize unwanted effects.

On top of a unique machine design, this thesis proposes a step-by-step analysis of the main physical parameters involved in near-field electrospinning (NFES). Through this analysis, key physical parameters and their variation are taken into account to properly understand their roles in the overall process. Afterwards, the process is parameterized with a force summation method. A superposition method was used to evaluate the main forces that contribute to the whole process. In this case, surface tension, gravity, electrostatic and viscous forces are combined. Experiments were performed using the designed test bench with results suggesting the validity of the theoretical approach.

Some final thoughts are provided in the conclusion of this thesis, in the hope that this test bench will give other researchers the opportunity to develop and tailor new materials in the ever-growing world of polymer and materials science.

CHAPTER 1

ELECTROSPINNING & VARIANTS

1.1 Overview

In this section, a review of the basic electrospinning technique is provided. The objective is to understand the influent parameters and also determine functional ranges of machine parameters, followed by how different collector variants may improve or change fiber production.

1.2 Fixed setup

To begin with, an electric field deforms a fluid from a dispensing needle, to a point where it breaks away in the form of a jet (Figure 0.1).However, in order to maintain steady state, one last element needs to be added to the system, a syringe pump (Figure 1.1).

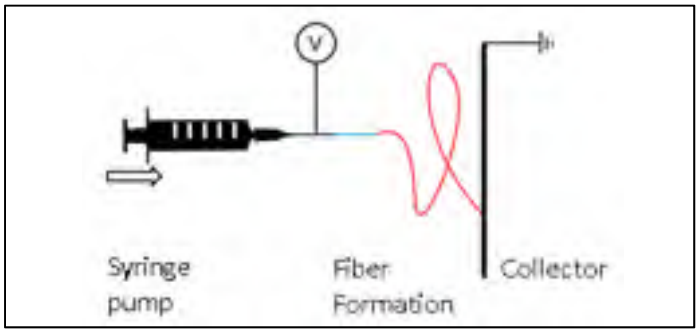

Figure 1.1: Basic electrospinning setup consisting of; a syringe pump, dispensing metallic needle, high voltage supply and a grounded collector.

The fine balancing between all these elements allows the steady production of a continuous jet. In typical applications the fluid is a polymer solution that once the jet forms, solidifies when the solvent has evaporated and produces very small fibers, with diameters as low as 150nm (Zhu et al 2017). One of the most difficult aspects of this technique is the fluid

formulation because of the interdependencies that the physical properties have in relation to the process. In fact, this is a very complex electro-hydrodynamic process. In some cases, some formulations are not “electrospinnable” and certain methods are used to modify some physical properties. One example is the addition of salts to increase the conductivity of the fluid (Electrospin Tech, 2019 and Qin et al. 2007). Some other cases involve adding surfactants to modify the fluids surface tension (Zheng et al. 2014). However, the scope of this thesis is not a specific formulation or application, the focus is on the process itself and machine parameters. The following items are related to the experimental setup:

1. Syringe dimensions;
2. Needle size;
3. Flow rate (syringe dispensing rate);
4. Applied voltage;
5. Collector distance;
6. Collector shape;

In terms of machine design and variable control, the first two parameters can actually be eliminated since they make an ensemble to create the flow rate. Preselecting the proper needles and syringes is important for a successful experiment as a first step. On the one hand, some formulations require larger sized needles to avoid jamming or restrict too much the flow. On the other hand, syringe size selection is critical for the proper flow rate due to equipment limitations. The last two are geometrical factors that are directly related to the electric field. So, we end up having 3 machine-controlled parameters:

1. Flow rate;
2. Applied voltage;
3. Collector distance;

1.3 Electric field

The vast majority of papers published, suggests that successful experiments are commonly achieved with similar setups to the one in Figure 1.1. For instance, target collectors are situated

between 5 to 20 cm and a maximum voltage before breakdown seems to correspond to a value around 30 kV. Given this, a simple electrostatic finite element analysis (FEA) model (description in APPENDIX I) was prepared in order to illustrate the electric field distribution (Figure 1.2).

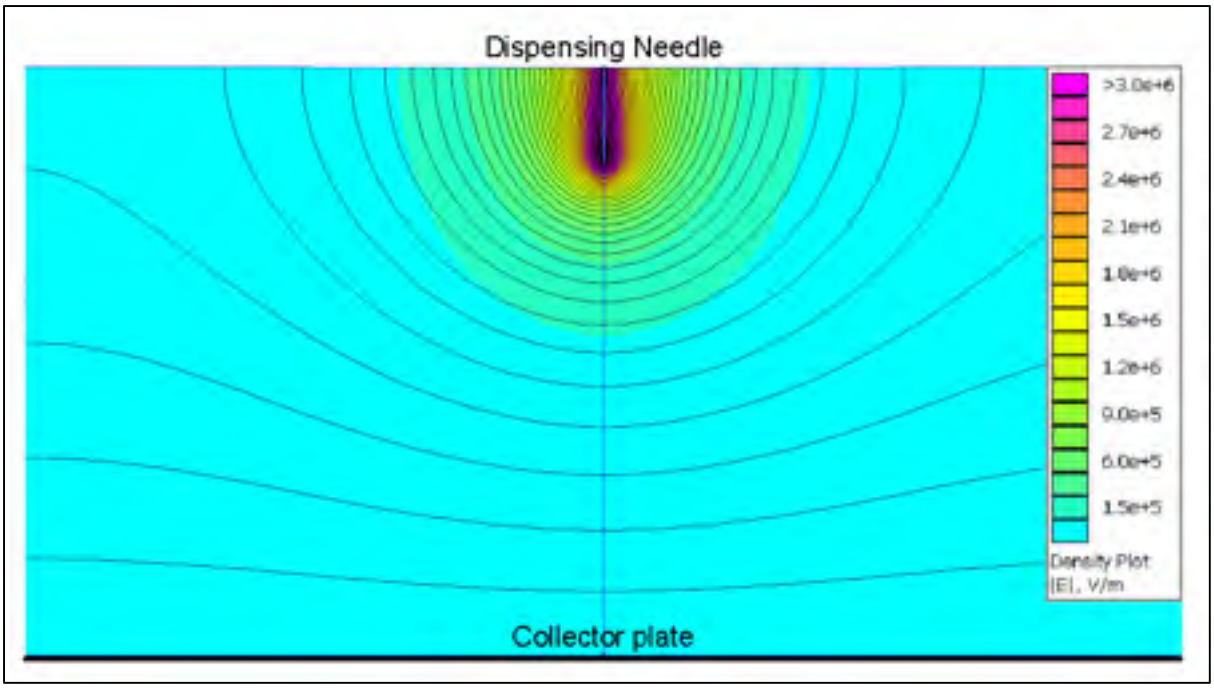

Figure 1.2: Voltage distribution of a fixed collector setup

The fuchsia coloured upper part corresponds to the application of a positive voltage of 30 kV on a 10mm long dispensing needle (vertical setup). The calculation was performed with an axisymmetric boundary condition at the origin's vertical axis. The complete lower segment is grounded and the equipotential lines show the field's voltage distribution. The uniformity of the electric field near the collector plate illustrates the difficulty in accurately placing a fiber onto a specific location of the collector plate and explains the randomly oriented "mat" of fibers produced. The typical appearance of such a mat of randomly oriented fibers is shown in Figure 1.3.

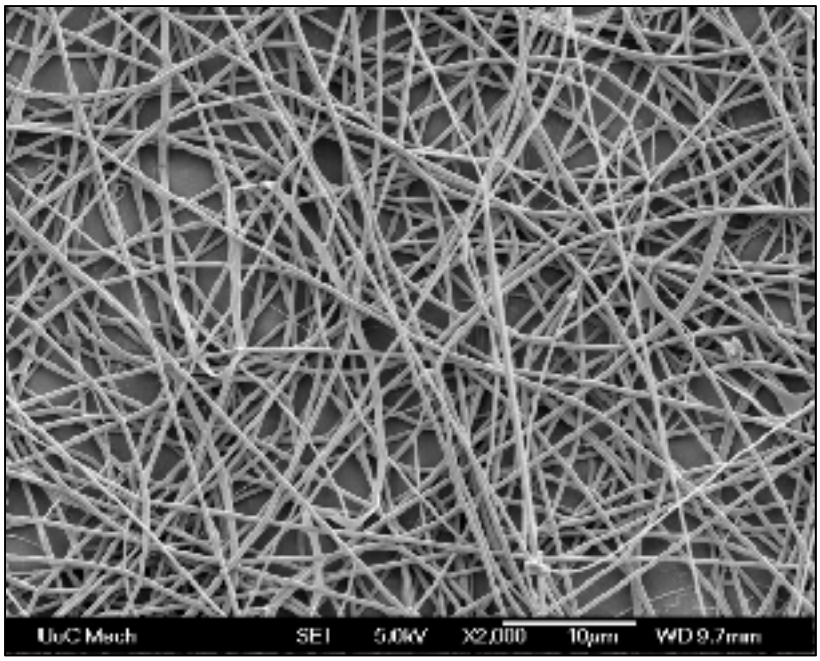

Figure 1.3: Typical electrospun mat (after Bhattacharya et al., 2014)

Fibers randomly pile up and the consistency of the fiber diameter is difficult to maintain. Since the fibers spiral onto the deposition site, the resulting pulling forces are also variable due to random pulling directions.

1.4 Complex collector geometries

In an effort to control fiber deposition, some complex collector geometries have been tested in the literature (Zander 2013). The idea behind this is to modify the electric field to force fiber deposition onto a specific region to create a pattern.

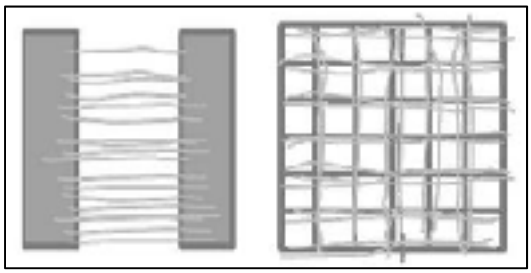

Figure 1.4: Complex collector geometry examples (after Zander 2013)

A simple electrostatics FEA analysis of the electric field shows the effect of placing two grounded conductive regions instead of the collector plate (Figure 1.5).

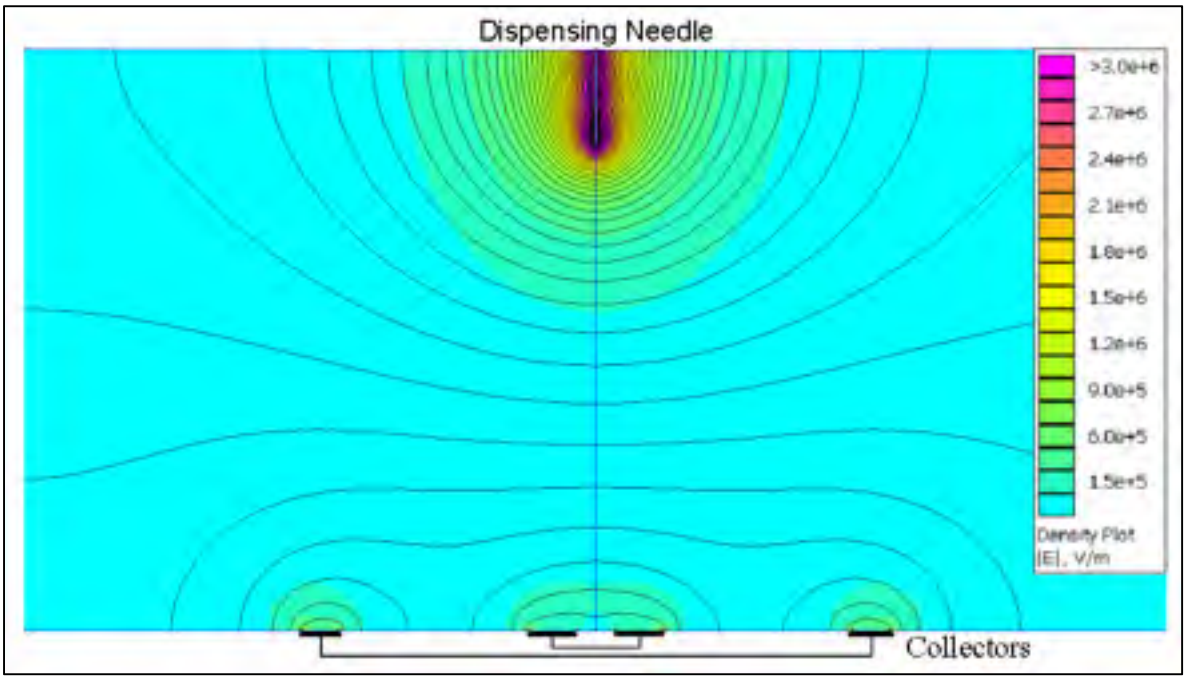

Figure 1.5: Multiple grounded collectors (2D axisymmetric)

The modeled electric field shows a case were two grounded segments, replace a flat collector plate (these correspond to the equivalent of two flat rings). We can clearly see the electric field focalizing around these segments and we can take advantage of the spiralling effect of the fiber to randomly alternate between these 2. In this case, we can predict a result analogous to the first geometry in Figure 1.4. This raises the question of how easy it is to distort the electric field around the process (or around the space of fiber formation). By doing so and adding different collector geometries we can effectively control overall fiber deposition patterns. This is also a clear indication of some precautions that need to be taken during the design phase of the test bench. Since conductive materials and their geometrical positioning around the electric field can change the sites of the deposited fibers.

For example, a simple modification, like adding an external grounding element in the vicinity of the electric field (sides of Figure 1.6). The electric field is distorted in a such a way that it will easy to modify the trajectory of the fibers.

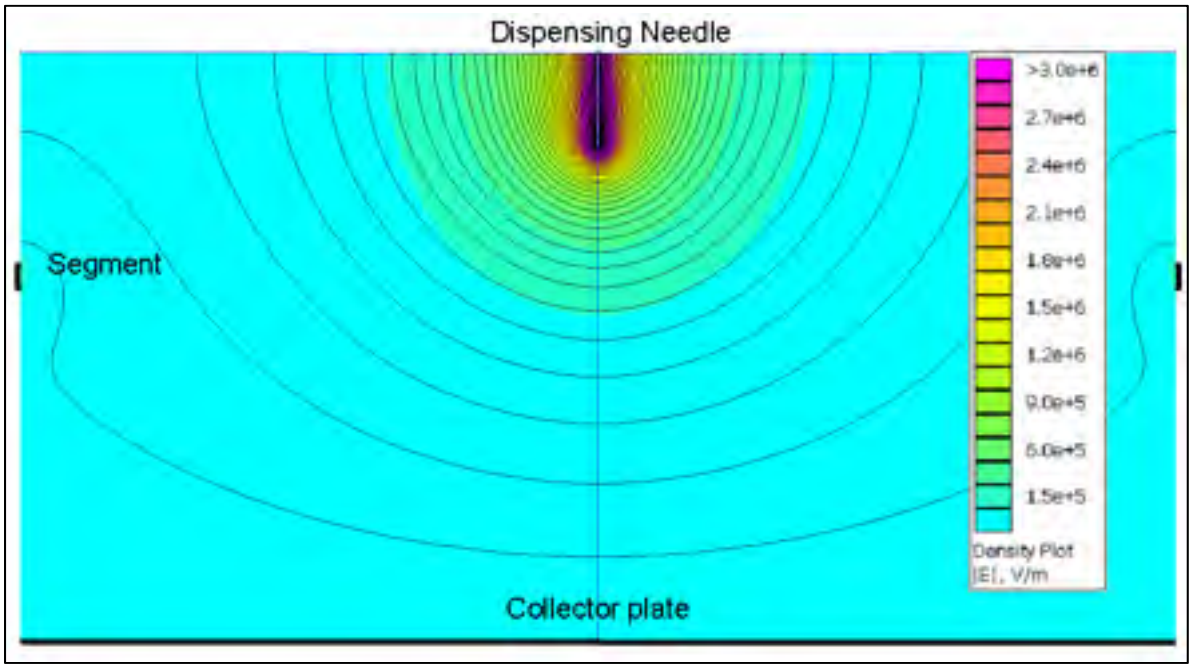

Figure 1.6: Intrusion of a grounded element in the electric field

In this FEA analysis, adding a single grounding segment at the right location demonstrates that the field will be a little stronger on this portion and most certainly will attract some of the fibers. This could be analogous to a mounting bracket or any type of support to hold certain elements in place. In order to prevent any further distortions, it will be preferable to use dielectric components in the surrounding areas of the process. This serves as an important guideline during the design phase of the test bench.

1.5 Rotating collectors

Two configurations are possible for rotating collectors, but the most popular method of aligning fibers is the use of a rotating drum collector (left image of Figure 1.7).

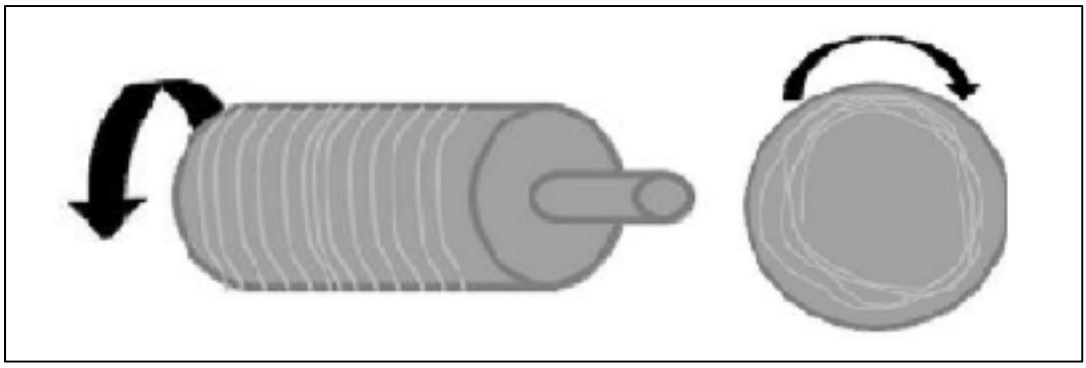

Figure 1.7: Rotating collector types (after Zander2013)

On top of fiber alignment, spooling fibers provides an additionnal control paramater which is the speed of the collector. This additional control also implies the ability to mechanically stretch the fiber. In essence, compared to a fixed collector configuration, the solidification of the fiber has a lot less influence on the deposition pattern since its physically forced to a certain position. Similar to a yarn spooling device, to properly spool the fibers, a linear guide is required to distribute the fibers more evenly over the drum (Figure 1.8).

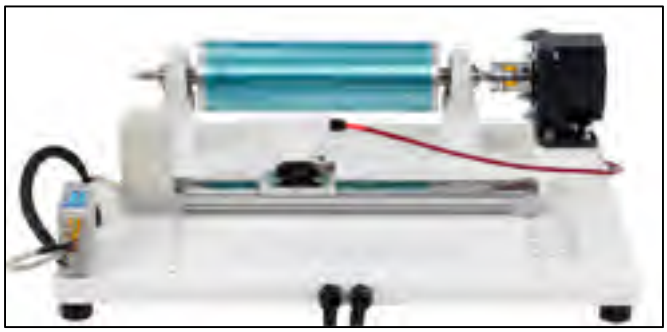

Figure 1.8: Typical drum collector setup Spraybase®

This electrospinning unit from Spraybase® shows a programmable unit that will spool fibers while simultaneously moving the needle across the rotating drum. After some calibration of the machine parameters, we can expect to produce fibers that are similar to those shown in Figure 1.9.

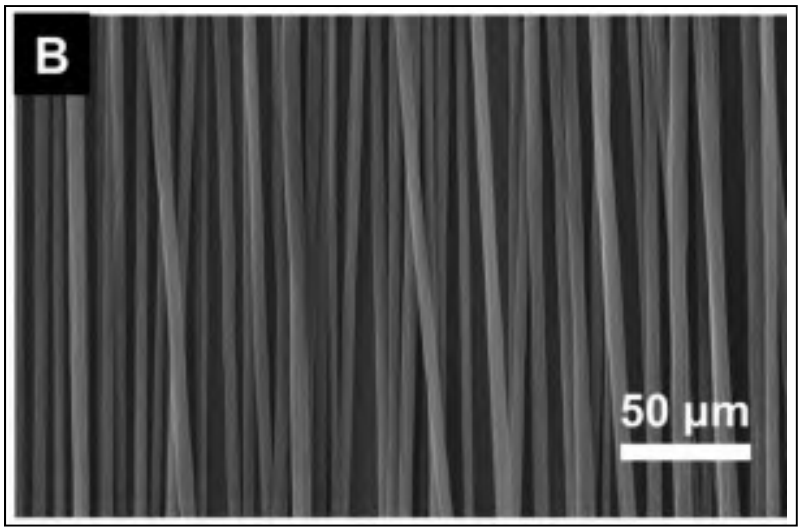

Figure 1.9: Example of fibers obtained with a rotating collector setup. Scanning electron microscope (SEM) micrograph of Polystyrene fibers (after Dotivala, A.C. et al 2019)

1.6 Near field electrospinning

Combining all elements and information of the previous electrospinning variants we have concluded that first: the geometrical shapes that influence the electric field play a critical role in fiber deposition. Secondly, with the introduction of a rotating collector we also add the mechanical pulling effect from the drums rotating speed. Both of these facts serve as an important design and control criteria.

Although successful experiments are achieved from the 2 previous variants of electrospinning (Fixed and rotating collectors), there is rarely any literature where the distance is fully minimized. After all, following Coulomb's law on a 2-point charge, $F = kq_1q_2r^{-2}$, the electrostatic force is a function over a squared distance. Translated to our case, it is better to treat this as an electric field (a voltage over a distance). And when relating to the 1965 paper by G.I. Taylor, the force exerted by an electric field on a cylinder with a hemispherical tip (Taylor 1965), he defined a relation where P is an exerted force depending on the voltage (V) and distance (H) with the length of a cylinder being (L) and its radius (R) as shown in equation 1.1.

$$P = \frac{V^2 L^2}{4H^2} \frac{1}{\ln\left(\frac{2L}{R}\right) - \frac{3}{2}} \tag{1.1}$$

So, combining both voltage and distance we get $\left(\frac{V}{H}\right)^2$. To take advantage of this distance to reduce the voltage we should be able to minimize it. However, there are few examples in literature (Pillay et al.2013) where the distance is minimized with a fixed collector. It is therefore difficult to understand the underlying nature of this case.

Looking deeper into it, distance increase acts as an accelerating ramp mimicking a mechanical pulling effect. Essentially, the fiber has a longer exposure to an overall pulling force helping it gain velocity. In general, with an increase in the distance between the needle and the collector the diameter of electrospun nanofibers decreases (Doshi et al. 1995). At smaller distances, the solvent does not have sufficient time to evaporate completely resulting in nanofibers with flattened structures due to inadequate drying. It is therefore difficult to understand the underlying nature of this parameter. The electrospinning process is a very complex subject and as a consequence it is hard to isolate and evaluate the effect of a simple parameter relation. Worst yet, nobody in the literature has developed mathematical tools to see what are the most important variables. There exists a statistical approach developed by Kiefer in 1986 (Kiefer,1986, and Atkinson later on, 1996) in order to design an experimental process to estimate a good starting point. So, one of the objectives of the present work is the development of simplified mathematical tools that combine numerical analyses in order to provide logical starting experimental values.

Given all this, near-field electrospinning (NFES) is a variant where the distance is minimized and a moving collector acts as an additional pulling force. Collector speed is then an important factor for a successful experiment as much as the distance of solidification process.

1.6.1 3D printing technology

Similar to a 3D printing process, retrofitting components onto an existing platform seems like a quick solution. Logically, the objective is similar which is to produce a pattern at a specific speed. Unfortunately, there are several constraints that prevent the use of 3D printing platforms.

The first is the software. Most 3D printing machines come with a proprietary method of treating stl geometry file formats. Through preprogrammed algorithms, the geometrically estimated shapes are produced with trajectories that satisfy shape filling ratios and specific spacing's. The process being gravity fed molten polymer, initiation, heating rates and flow control are directly integrated to pattern generation and spacing. This creates the issue that only the particular physical platform for which the proprietary software was designed for can be used.

The second issue at hand is the precision and resolution of offered systems. Increased system resolution and precision rapidly increases cost. Unfortunately, these higher end units also combine other unnecessary expensive modules which serve no purpose in electrospinning. Most high-end models sell for over $15000, for example a Solidscape® brand 3D printer.

The third issue is the most important, which is related to high voltage management. There is no 3d printer available that manages high voltage discharges. If the system ever had a high voltage short, it would most likely destroy most of the precision electronics. It would then require a full modification of an existing unit to replace and modify some of the axis and mounting brackets with insulating components. As mentioned previously (1.3), the electric field is easily distorted by any conducting element in its vicinity.

The last issue at hand is the deposition speed; most 3D printers require a rather slow linear speed to print structures. Most printers have deposition speeds around 60 mm/s (Anycubic, Makerbot brands) and a travel of around 150 mm. Faster options are currently not available at a reasonable price and precision.

Several authors suggest linear speeds of around 100 mm/s with some going up to 200 mm/s for near-field electrospinning (Fryer, C., et al 2018). All things considered, building a test bench specifically designed for near-field electrospinning guarantees a robust and reliable experimental process. The proposed design in this thesis not only provides a well thought out basis but also the flexibility of modification for future implementations.

1.6.2 Parameters and control

As established previously the controllable parameters are enumerated in the following chart:

Table 1.1 : Test bench parameters

Parameters	
Flow	Syringe needle
Electric field	Temperature
Deposition speed	Pressure & Humidity

As a first iteration of machine design, environmental parameters are only to be measured and not yet controlled. Further improvements or add-ons can later be implemented and this option is considered in the systems capabilities. One of the most difficult aspects of this test bench is the combination of high voltage electric field control with nearby sensitive electric components coupled to high precision/high speed assemblies.

1.6.3 Flow control

Various forms of flow control are proposed through different manufacturers of syringe pumps. Most will use syringe diameters and flow rates to calculate linear syringe displacement speeds. Fortunately, it is all integrated into a functional package and depending on the choice of dispensing units, most will provide a minimum and maximum dispensing rate. Linear speeds can be fine-tuned through different syringe diameters if the linear speeds fall out of range. The most affordable and suitable units are from the NewEra® brand syringe pumps. They also

provide instrument communication compatibility and with some programming, can communicate with a PC.

1.6.4 Electric field (Voltage and distance)

Electrospinning will only occur when the supplied electric field creates a pulling force that is higher than the force holding the exposed fluid to its adjacent structure. This applied electric field varies a lot from one author to another and even though a unique setup is desired, several other factors need to be accounted for. Varied polymer formulations make it so that from one solution to another fine-tuning distance and voltage creates optimised results in function of a specific case. Typical values used in a simple electrospinning setup range from 5 kV to around 35 kV (Robb et al. 2011). Collector distance is usually around 5 to 20 cm for the same collector setup. Design parameters are set at twice the highest values encountered in most literature. Since the proposed design accounts for most setups of the electrospinning technique, this large range allows for process flexibility.

Since the most complex technique of the test bench is the near-field setup, it is also the one that requires the shortest distance (typically 1-3 mm) and consequently, the lowest voltage (as low as 800 volts). Inversely, the range being much smaller, proper system resolution is also a requirement. All things considered, combining the previously discussed elements of this chapter, there are no available electrospinning units that encompass all criteria and the flexibility of having every setup in one unit.

CHAPTER 2

TEST BENCH DESIGN

2.1 Overview

This chapter focuses on the process of component selection with the scope of integrating all requirements in the simplest form possible. Process control is also discussed and implemented in the final design. (See APPENDIX II0, for machine details)

Given the size of produced fibres (submicron), solutions that offer this type of resolution are expensive and do not provide the required combination of deposition speeds and travel distances. For these reasons, the chosen components are not able to offer this level of resolution. The objective is to provide a platform that allows the process to be fine tuned and create wider spaced structures. Once the process is better understood, the resolution can be increased through a combination of actuators and motorisation upgrades (e.g. gearboxes, higher step counts, better encoder feedback.). The idea is to provide; a high precision, high stability platform that allows for future modifications, as necessary. As mentioned in the previous chapter, any electrically conductive or grounded component in the vicinity of the process can alter the deposition process by affecting the electric field. For this reason, linear motors which offer a compact and very high-performance solution are discarded. Since the magnetized portion would be near the deposition zone, it can easily modify the electric field. Therefore, more traditional actuators are used, including ball screws.

The simplified machine requirements are shown in Table 2.1, fall into 3 categories and represent the overall test bench design considerations.

Table 2.1 : Test bench design requirements

Requirement	Type	Challenge	Category
Combined movement	Linear actuator	High speed and precision are difficult to combine	mechanical
Collector travel	Length of linear actuator	Longer is expensive and reduced overall precision	mechanical
High voltage capability	High voltage assemblies and cables	Insulation and sensitive component localisation	electrical
Standard electrospinning	Overall space and geometry	Field distortion due to nearby components,	Mechanical
Rotating drum collector	Add-on	Space and electrical connection interface	Mechanical and electrical
User safety and components	Security elements	Programming and additional procedures	Mechanical and electrical
Mechanical precision	Machine structure	Precision cost and weight (inertia)	mechanical
System interface	Programming	Ease of use	Logic and control
System connectivity	interface	Control interfaces, wiring and protocols	Logic and control

Given the importance of fully controlling the electric field, where the process takes place, it is the first thing evaluated before undergoing any machine layout or design proposition. Some key factors discussed in the next sub-section are leading design considerations.

2.2 High voltage layout and design

The most significant consideration is the orientation of the layout. Even if the majority of near-field electrospinning setups are built vertically, a proper evaluation to determine orientation is crucial since it is the driving design criteria. Three possible configurations are shown in Figure 2.1 and evaluated in Table 2.2.

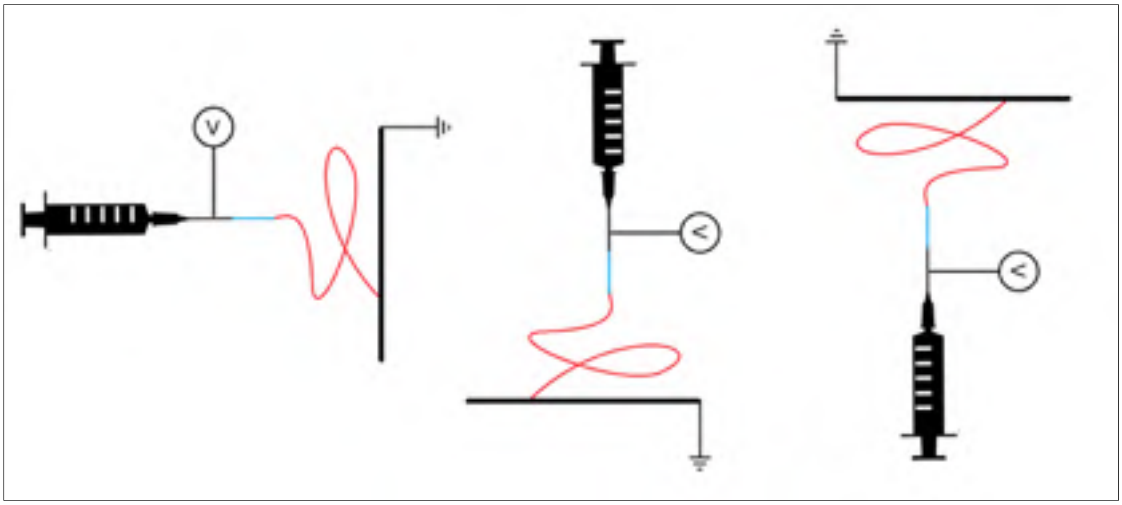

Figure 2.1: Electrospinning layout types (From left to right; Horizontal, vertically assisted, vertically opposed)

Table 2.2 : Typical electrospinning layouts

	Advantages	**Disadvantages**
Horizontal	• Needle purge doesn't affect results(dripping) • Setup reference is simple • Most syringe pumps are horizontal, no need for special mounting brackets	• Cone shape doesn't initiate symmetrically (difficult to calculate) • Near field electrospinning will be more difficult to initiate • Mechanical components need to significantly increase the perpendicularity tolerance • Moving parts are greatly affected by vertical displacement (motor torque differences in 2 directions due to weight)
Vertical 'assisted'	• Gravity on the fluid slightly reduces the required electric force • Axisymmetric process simplifies calculations • Moving parts are easily stacked	• Needle purging affects deposition zone
Vertical 'opposed'	• Needle purge doesn't affect results(dripping) • Axisymmetric process simplifies calculations	• Gravity on the fluid slightly increases the required electric force • Leftover fluid from purging can affect the shape and process (Excess gets stuck to the needle sides due to surface tension) • Moving components are situated above the dispensing needle requiring a stronger structural platform for components

After evaluating all layout configurations, the vertical assisted layout was selected as the most feasible. Although gravitational forces are almost negligible, this layout slightly reduces the required electric field (Shown in Chapter 3). All things considered; horizontal layouts are mainly suited for standard electrospinning. In our case, it is discarded because of near field electrospinning difficulties cited in Table 3.1, most notably fabrication difficulties and process modeling.

2.2.1 Electrical breakdown

The dielectric breakdown strength of air being approximately 3 x 10^6 V/m, it is very important to not place any sensitive components within a distance where breakdown can occur. Since a maximum operating voltage of 50kV was selected, the minimal distance has to be respected to avoid any unwanted electrical component shorts.

$$D_{min} = \frac{50000[V]}{3E6[V/m]} = 16.\bar{6}[mm] \approx 17[mm] \quad (2.1)$$

Since minimal distance to breakdown occurs at less than 17mm for a maximum applied voltage, it is critical that all components are located further, unless they are properly shielded. In order to maintain a safer distance, due to air changes (temperature and humidity), a safety factor of 2 is used throughout the whole machine design.

2.2.2 Electrical field distortion

Even if components are further away than 34mm (Breakdown safety distance, red line in Figure 2.2), the electric field can still be distorted and affect fiber placement (orange line). To avoid this issue, specifically when doing standard electrospinning, conductive components need to be avoided or put at a distance of at least 10 to 20cm (Orange line in Figure 2.2). Most literature will show normal types of electrospinning with a fixed collector around this distance. Since it is practically impossible to have any type of conductive material at a distance of 20cm,

especially anything holding the charged needle or collector, dielectric materials are used instead. In our case to simplify and avoid any issues, anything higher than the grounded collector (stacked actuator setup) is fabricated out of polymers. A logical approach to avoid this situation is prioritized for the machine overall design.

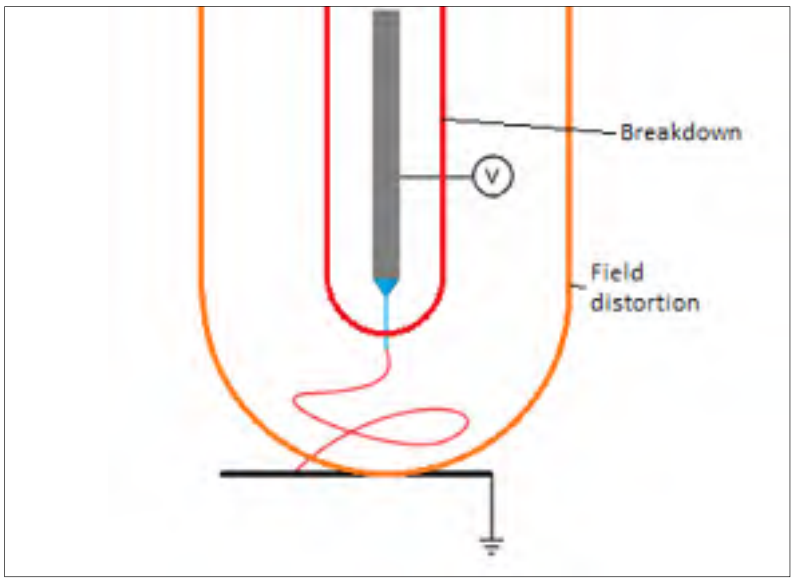

Figure 2.2: Field breakdown and distortion

It must be noted that this precaution is mainly considered in case the test bench is used for fixed electrospinning or a rotating collector. A protective cover must be used to protect high precision rolling elements and sensitive electronics from dust, as well as to protect the user.

2.2.3 High voltage collector design

The most influential part of the process is the shape of the electric field. Classically the preferred setup is illustrated in Figure 1.1. Charging the dispensing needle at a high voltage and grounding a flat collector to capture produced fibers. After evaluating the electric field distribution shown in Figure 2.3, we notice that the electrostatic pull on the collector plate is quite uniform and doesn't vary much from the center axis of the system. This indicates that if the produced fiber deviates from the desired trajectory (centered), the system will not naturally

bring it back. The field distribution is essentially parallel to the collector plate until an angle of around 10 degrees with respect to the center axis (Figure 2.3).

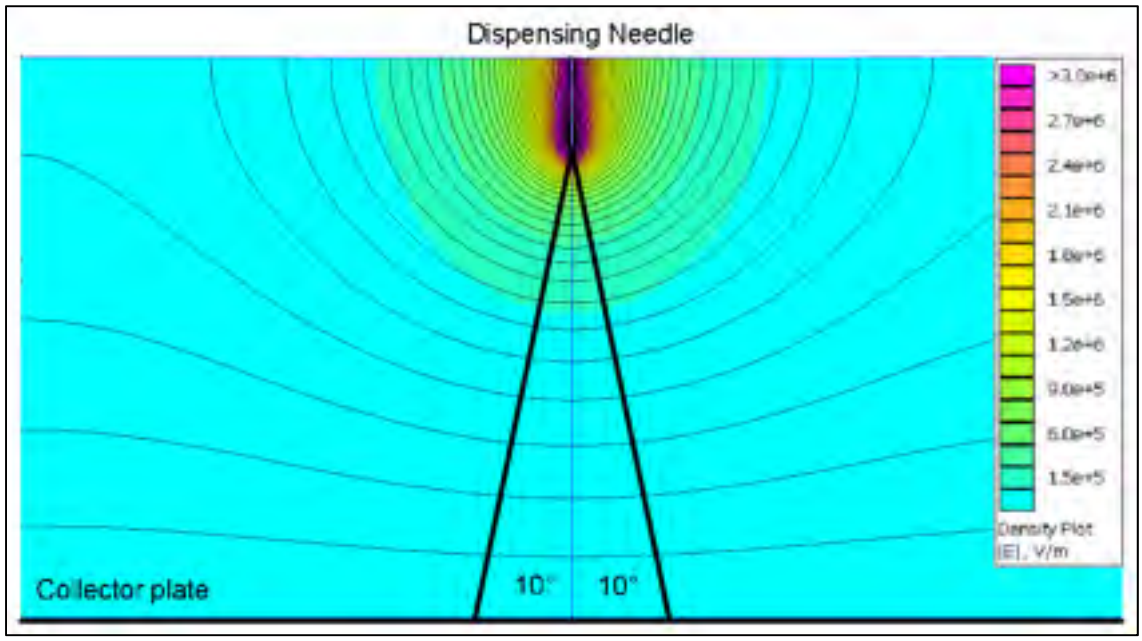

Figure 2.3 : Electric field of a simple setup (10°-line reference)

Further away, the field reduces quicker but still, not sufficiently to force a stray fiber to center itself (Approximate drop of 5-10% field intensity). In order to increase the stability of the process, a needle-to-needle geometry was proposed (Figure 2.4). This would essentially act on the field by focalizing it and anything further away from the center would geometrically see a fast decline in electric field density. Evidently, this is due to the increased distance the field takes and also the direction of the field (perpendicular to sides) away from both needles.

One last element was added to properly control the shape of the field, an external grounding tube to encompass the process and electric field. The idea behind this is to be able to catch the field further away from the process acting like a protecting element. This helps in maintaining the field shape and makes it more robust to external variations. If ever there were interfering elements in the vicinity of the field, the field distortion would be minimized since it would take the preferred grounded geometry path. The proposed novel design uses a moving collector plate made of glass with a fixed needle-to-needle setup (Figure 2.4).

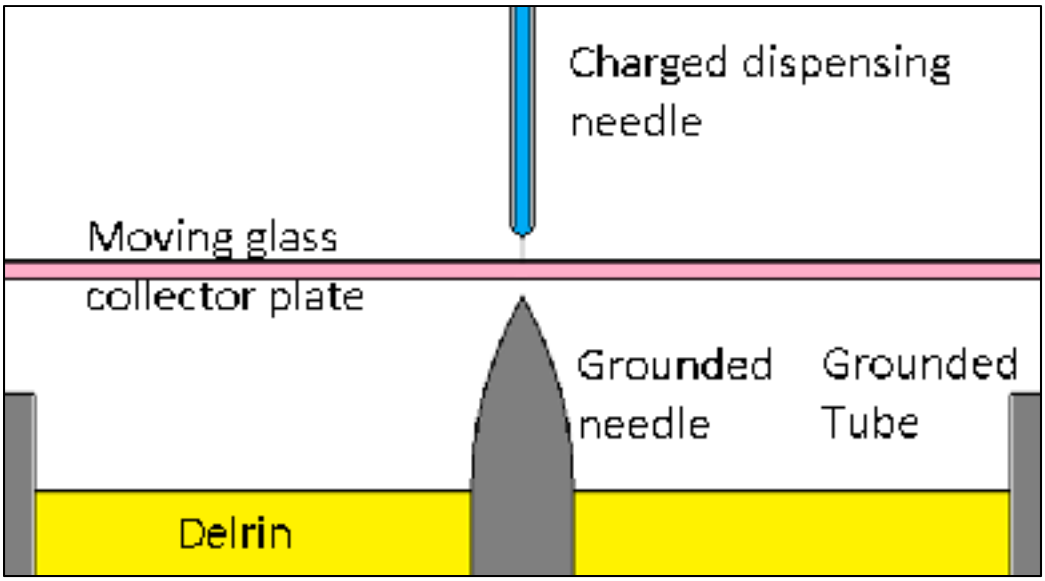

Figure 2.4 : 2D axisymmetric model for novel near-field electrospinning (NFES) setup

2.3 Component choice

Machine design being an iterative process, it is very difficult to propose an optimized way of designing and reuniting all requirements. Each main part of the machine is therefore individually optimised and readjusted to account for certain geometrical variabilities. As a general guideline, most of the machine design can be separated into 4 different categories (one additional to previously mentioned). Afterwards, they can be combined following the proposed sequential design loop in Figure 2.5. It must be noted, that actuator choice is by its own nature an iterative process (Iterative loop between motor sizing and stage design/weight). Since the useable torque output is dependent on rotor inertia, the larger the motor, the higher its inertia. It requires a few iterations to get the motors output torques at high speeds to overcome the required calculated torques (APPENDIX IV0).

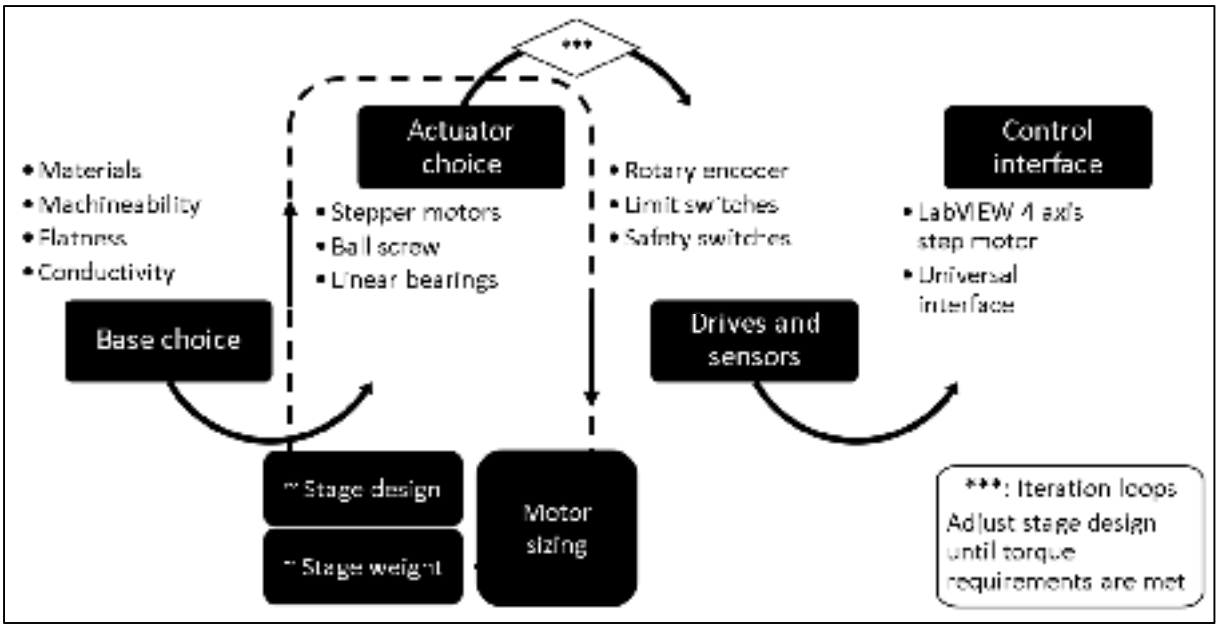

Figure 2.5 : Sequential design loop

Machine base selection is evaluated in depth in APPENDIX IV0. Being the main structure to which every geometrical element is fixed, special attention was given to its selection. Peripheral materials used around the process location are also looked after in terms of conductivity to not alter the process. As for actuator technology choices, only rack &pinion, ball screw and timing belt systems are evaluated due to them being cost effective. All three are compared in order to select the appropriate technology.

2.3.1 Linear actuator and motor choice

Deposition speed and precision being the main requirements, further investigation into what has already been published provides a good indication on the speed range. Although each polymer solution has its own functional set of machine parameters, a study by Chang shows the effect of speed on deposition in Figure 2.6. Given that water soluble polymer PEO was used in this example with a 5% concentration, it would be easy to assume that the required setpoint would to 200 mm/s. However, most of this author's successful near-field electrospinning experiments were done with PVDF solution at a 100 mm/s speed setup. Given the high density and fast evaporation of the PVDF solution, it can act as the extreme design

condition; a maximum speed of up to 200 mm/s will be sufficient to cover most eventualities (Chang, C., PhD Thesis, 2009).

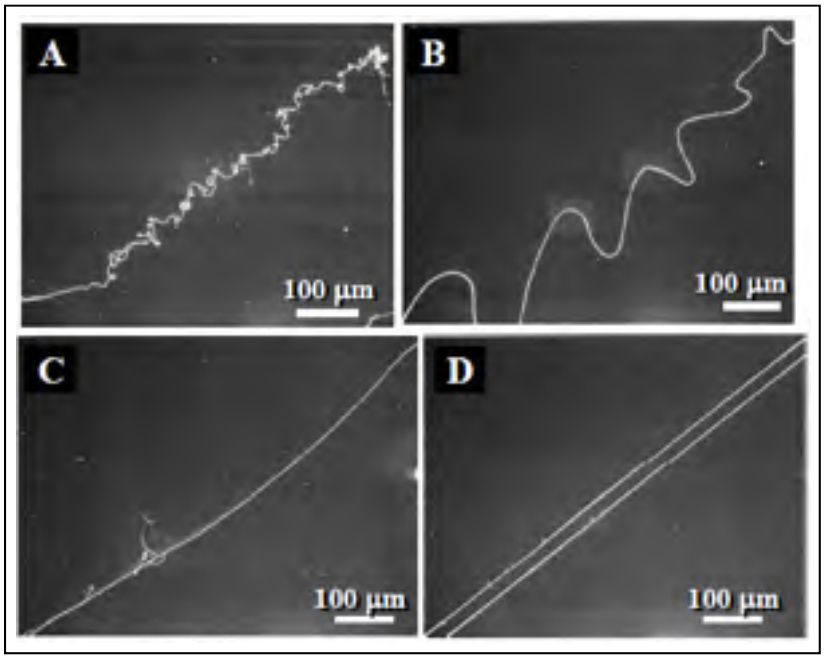

Figure 2.6 : Effect of deposition speed for a 5% PEO polymer solution; A=50 mm/s, B=100 mm/s, C=150 mm/s, D=200 mm/s. (after Chang 2009)

As the evaluation in APPENDIX II0 shows, ball screws with stepper motors and drives were selected for the application. Although the choice of combined ball screw pitch and stepper motor is at its limit, the significantly lower cost justifies its use. In any case, the mechanical structure can be upgraded to accommodate higher performance motor technologies if required. Some modifications may be needed in the form of motor mounts or enclosure modifications to allow larger components if the case requires it.

2.3.2 Materials and precision

Some elements in the design require high accuracy and dimensional stability. The machine base, its actuators and mounts for example. Other elements, which include the Z axis that supports the needle and the high voltage assembly, do not require such a high level of accuracy.

The case being that as long as these last elements do not move in time, they only require an initial precise setup. Any dynamic part, because these machine structures are so rigid and precise, their alignment is critical for proper function. On top of that, since they are responsible for the constructed polymer structures, they also require an overall accuracy.

2.4 Full machine design

All elements combined, as mentioned in sub-chapter 2.2, a vertically assisted layout coupled to a granite surface (AA lab grade)of 24x18 inches was chosen. The sizing of the machine footprint is mainly due to budget constraints. Granite is also dimensionally stable, has a low thermal expansion, and most importantly acts as an electrical isolating layer (APPENDIX III0, base materials comparative). As for linear actuators, a deposition surface of 200mmx200mm was established in order to fit all components into the machine footprint. Most polymer structures produced are so small that it defeats the purpose of having a larger useable workspace. Vertical travel is twice the typical deposition distance of 20cm to give the user the flexibility of incorporating any type of fixed collector. To protect the user from high voltage discharges and isolate the process, a hinged enclosure is installed. Made of 0.5-inch-thick polycarbonate, it is fabricated with vacuum capabilities in mind. With some modifications such as joint sealing and reinforcement, it should be able to withstand moderate vacuum levels. Respecting the design criteria to not affect the electric field, every component above the collector’s deposition surface (z-axis for example) is machined out of high density and dimensionally stable Delrin. Coupled to nylon screws and a machined polycarbonate support, vertical positioning of the needle has minimal interference with the electric field in all forms of electrospinning. The final machine design is shown in Figure 2.7 and Figure 2.8.

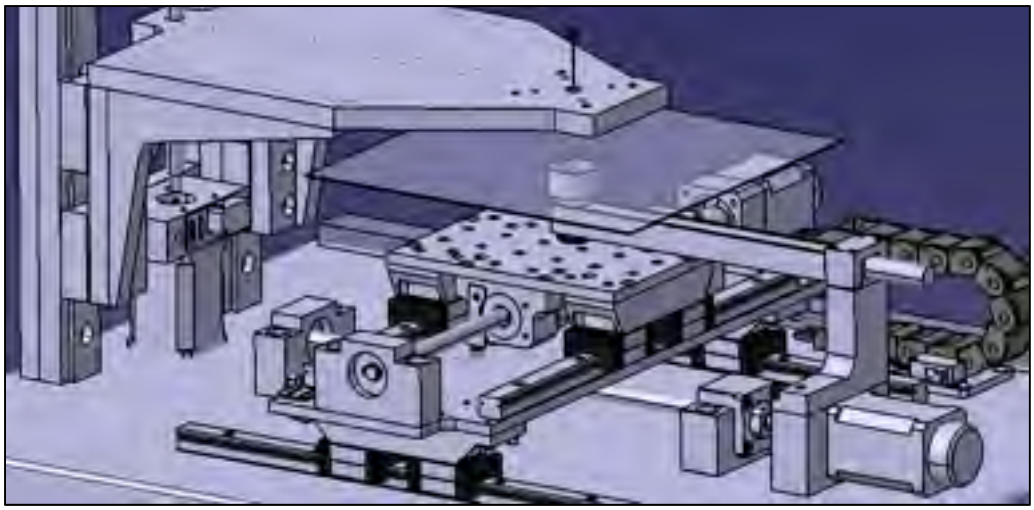

Figure 2.7 : CAD model of final machine design (without collector plate mounts)

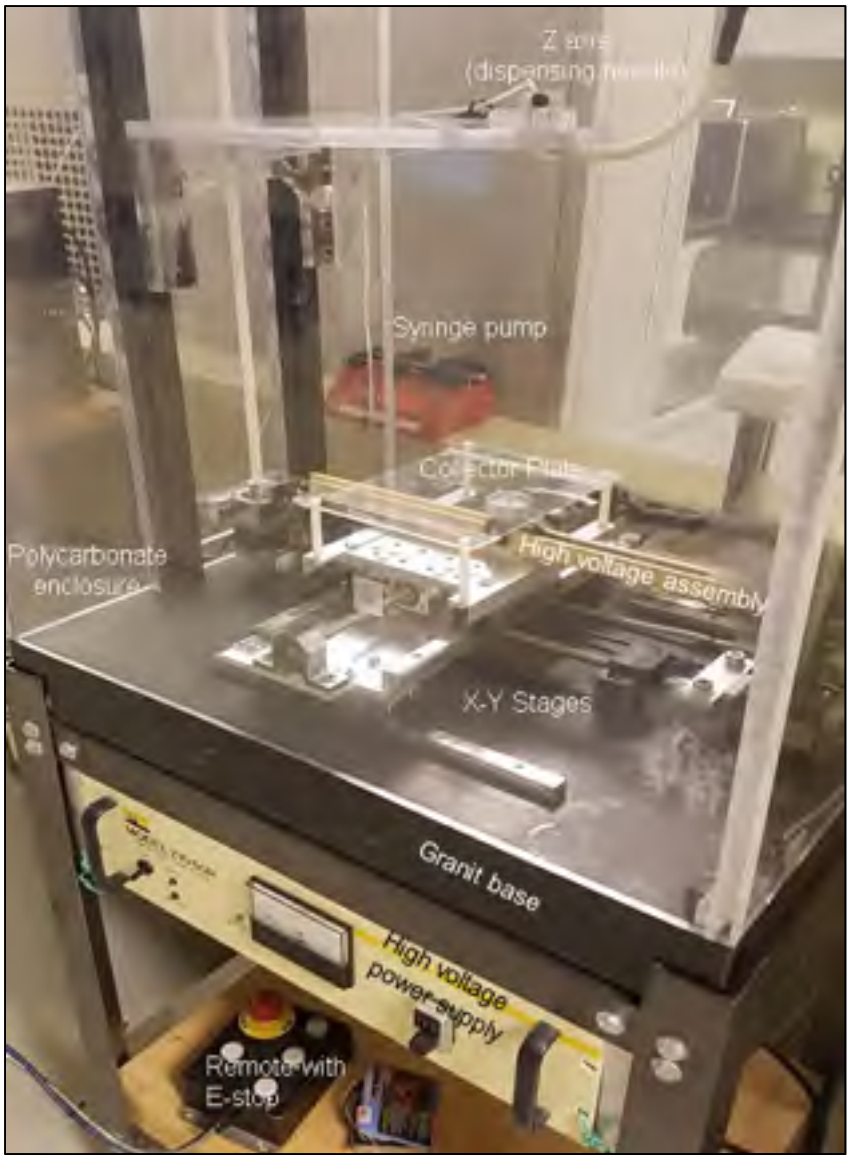

Figure 2.8 : Actual test bench

2.5 Control's and interface

Machine control simplicity was the primary design criteria for the user interface and electrical system. Since the test benches purpose is to produce complex structures that are normally not feasible on standard electrospinning equipment, several approaches were evaluated. From 3D printing to industrial automation, the most flexible programming method is by far g-code oriented controls. Using a point-to-point approach, this standardized trajectory definition can

be done manually, although it would be advantageous to use a specialised computer assisted manufacturing software (CAM). The latter providing fast trajectory generation and a robust approach that can easily be visualized and parameterized. Some key equivalent functions are implemented like, the activation of the high voltage power supply with the coolant activation code.

Since most of the motorization can be handled by off the shelf CNC systems, some more difficult aspects of the instrument-like voltage control and syringe pump communication required a different type of interface. The flexibility of the test bench, being an important factor, LabView controls were selected to be able to integrate future additional systems. In this case, the possibility to integrate high voltage control, pump initiation with flow control, environmental readout and, in the future, environmental controls, exists. Academic licensing made LabView the best available platform. The schematic in Figure 2.9 shows the overall chosen National Instruments components and peripheral equipment.

Figure 2.10 shows the control interfaces main menu and sub control panels. Although all 4 options are presented, actual equipment only has the custom and calibration sub control panels. It was decided that this control method gave the most versatility and the other 2 would eventually be implemented. Since the main process analysed is near field electrospinning, origin placement and precision are very important. It was also determined that both be separated in order to force the user to properly distinguish and understand the test bench dynamics.

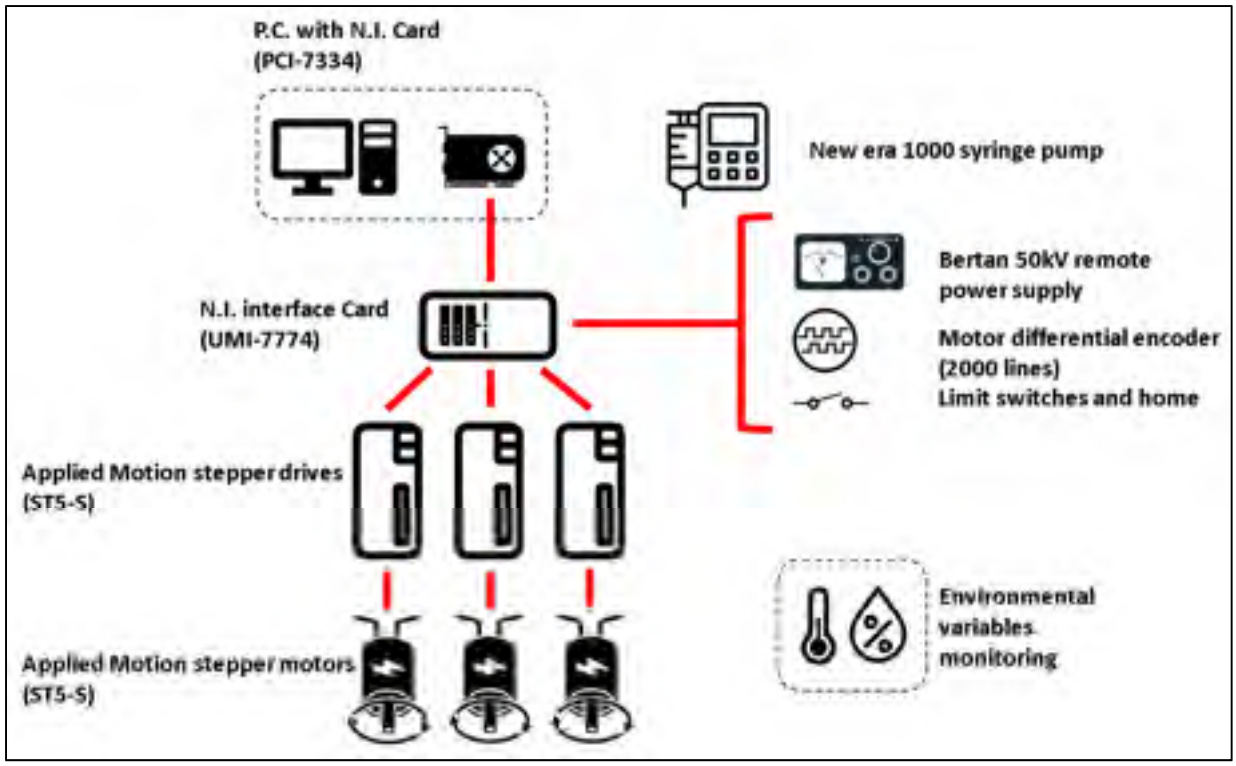

Figure 2.9 : Machine control schematics

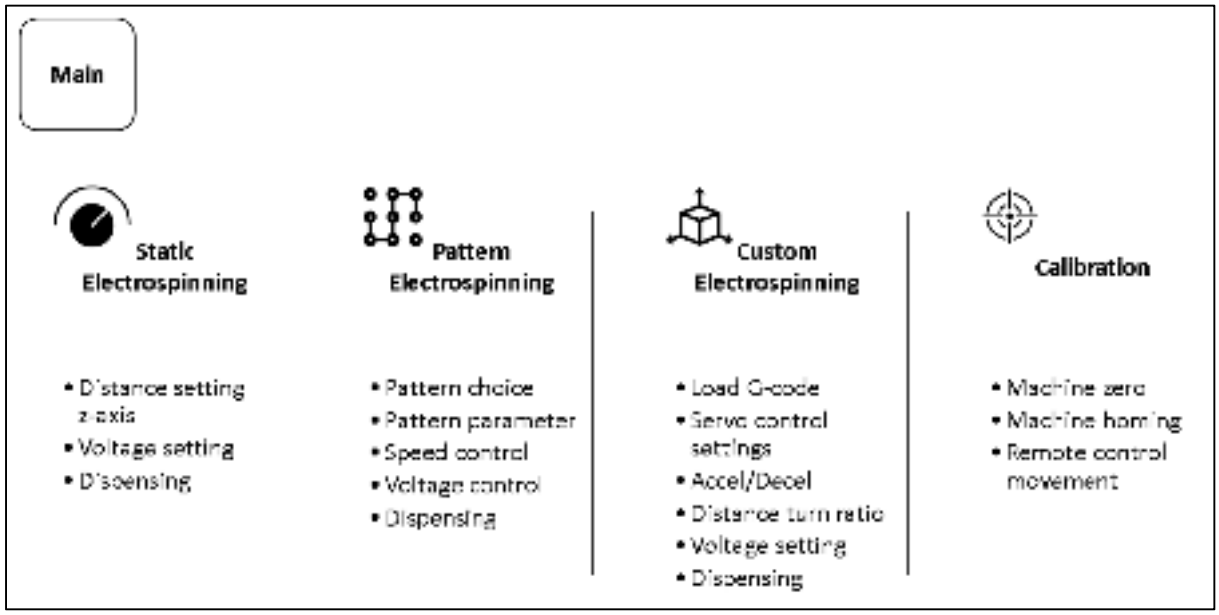

Figure 2.10 : LabVIEW Interface with sub control panels

CHAPTER 3

MODELING OF THE NEAR-FIELD ELECTROSPINNING PROCESS

3.1 Overview

To understand what the polymer solution undergoes, the diverse effects generated by an electric field on a fluid need to be understood. First and foremost, some hypotheses and simplifications are required since the problem gets very complex if non-linear properties are considered.

Before stating theses hypotheses, an evaluation of all physical property changes through the process is summarized in Table 3.1. It's also important to note that changes in heat and mass transfer, evaporation and environmental properties (temperature, pressure, humidity) are not considered.

Table 3.1 : Physical properties breakdown

Physical properties of the fluid and variation during process			
Mechanical	**Electrical**	**Change**	**Effect**
Viscosity		Increase	Viscous forces increase throughout deposition until full solidification due to evaporation
Density		Increase or decrease	Depending on the densities of polymer versus solvent, it will either increase or decrease during solvent evaporation.
Surface tension		decrease	Depending on overall solution variation; it usually decreases due to less surface interactions between solvent and longer molecular chains of polymers
	Resistivity	decrease	Usually increases because most polymers are dielectric.
	Conductivity		Inverse of resistivity
	permittivity	Increase or decrease	Depending on fluid formulation, usually varies from that of the solvent to that of the polymer.

3.2 Hypotheses

3.2.1 Viscosity

For the sake of discussion, the fluid is considered Newtonian throughout the whole electrospinning process. This simplification helps in the estimation of a time dependant analysis. The nature of the fluid could be else such as thixotropic or viscoelastic. But within this work we shall consider the fluid Newtonian.

3.2.2 Surface tension

Surface tension is one of the main contributing forces in the process of electrospinning. As shown in Taylor's electrically driven jets, his predictive equation is the following:

$$V_k^2 = \frac{4H^2}{L^2} * \left(\ln\frac{2L}{R} - \frac{3}{2}\right) * (1.3\pi R\gamma) * (0.09) \tag{3.1}$$

Units being; V=applied voltage between charged plates, H=distance between needle and grounded plate, L=needle length, R=radius of needle, γ=surface tension and the value 0.09 is used to balance the equation so that V_k units are in kilovolts.

Notice all the parameters are length units except for V and γ which represent respectively voltage and surface tension. Essentially, there are 2 main contributing forces which are created by the electrostatic pull and surface tension. In simpler terms, the only thing that is holding the fluid to the dispensing needle, is the interaction to it, which is the surface tension resulting force. This force holding the fluid to the needle is therefore opposing an electrostatic pulling force. The difference between the two, is that the electrostatic force has a relation that is squared depending on its electric field (V/m). In a way, it is important to be able to precisely characterise surface tension and its geometrical parameters. In Taylor's paper, a very important

angle value is used to calculate the axial component of the surface tension resulting force which is 49.3°, present in the 1.3π term in equation 3.1.

To understand the origin of these terms, we calculate the force acting on a half spherical droplet retention, we then get a similar term that is; $2\pi R\gamma$ (Figure 3.1).

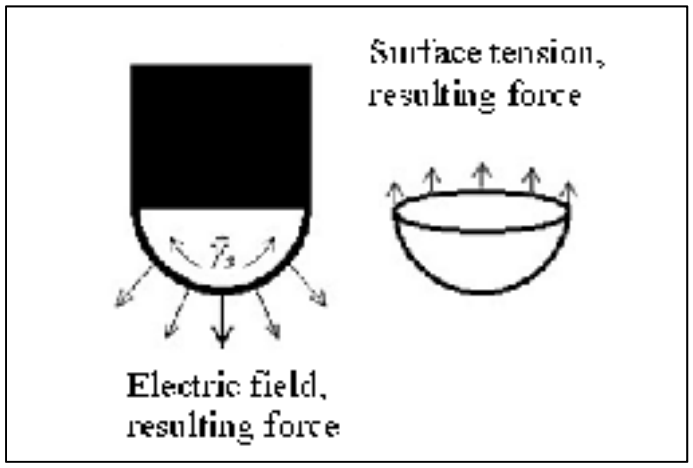

Figure 3.1 : Hemisphere with 2 main acting forces
(Electric field and surface tension related)

Since the shape of the elongated fluid tends to transition towards a cone, this term is adjusted with $\cos\theta_T$ relative to the needle axis ($\theta_T = 49.3$). The use of this angle will be explained during the process calculation and its relation to the chosen polymer solution. This transition from spherical to conical is key in understanding later on, that for the fluid to break away from the needle, we transition from 2 conditions. These 2 conditions being surface tension at the needle and later on, local surface tension at the jet breakaway (cone tip). Even if there is some fluid evaporation happening between the needles exit and the jet formation, this property is assumed constant throughout the process in our model.

3.2.3 Electrical properties

Electrical properties in general are set with fixed values and their variation is not considered. For instance, we can split what goes on in terms of electrical displacement. Two key concepts

are evaluated in order to simplify calculations. One is the example of H_2O, being a polar solvent, when subjected to an electrical field, will mainly polarize. We look at it with the following perspective; its relative permittivity is 80. Since theoretically H_2O does not have free charges that allow electrical transport the electric field will be used to flip the molecules and align them (polarizing the medium). In the latest works of G.I. Taylor, some more complex modeling of this is called the leaky dielectric model. It takes into account the charges in the fluid and how it moves the fluid in a droplet. As a general rule, charges will tend to migrate to the surface of the solution under an electric field. In a similar fashion as capacitor plates will accumulate charges in between them (Collins G., et al., 2012).

3.2.4 The role of permittivity

As mentioned previously, permittivity of the medium plays a key role. The implication of this physical property can be demonstrated by evaluating an electric displacement. Described by 2 components which are an electric field and also the polarization of the medium, this is its simplest expression ($\vec{D}$=electric displacement, ε_0=free space permittivity $\vec{E}$=electric field and $\vec{P}$=polarisation).

$$\vec{D} = \varepsilon_0 \vec{E} + \vec{P} \tag{3.2}$$

Another way of describing electric displacement is by using electrical susceptibility. This term describes the degree to which the medium polarizes:

$$\vec{P} = \varepsilon_0 \chi_e \vec{E} \tag{3.3}$$

Here, ε_0 is the permittivity of free space and $\chi_e$the electrical susceptibility with E being the electric field. If we combine the 2 terms to simplify, we obtain the following:

$$\vec{D} = \varepsilon_0 \vec{E} + \varepsilon_0 \chi_e \vec{E} = \varepsilon_0 (1 + \chi_e) \vec{E} \tag{3.4}$$

As for χ_e, it is equal to the relative permittivity minus one, $\chi_e = \varepsilon - 1$. Obviously, this is the general equation but in reality, the terms when treated under a frequential analysis become much more complex. The reason being, is that no medium polarizes instantaneously but in the case of fluids, specifically water, the time to fully create a dipole moment ranges on the 10 picoseconds. With a time-frame so small and especially in electrospinng, the system takes much more time to form and surpass inertial forces of the fluid that this is negated in any analysis related to steady state.

This analysis is able to identify a fluid's main electric displacement component, either mobile charges will move or the medium will be polarized or, in most cases, both phenomena. The important part is that further in this chapter we notice that the more the electric displacement polarizes due to a higher relative permittivity, the more likely we are to obtain an electric component balance that dictates a critical geometrical value that is the Taylor cones angle.

3.3 Polymer solution choice (PVA)

After carefully evaluating the range of available polymers, PVA and water were chosen for a few simple reasons. The availability of the polymer, the fact that it is biocompatible and its ease of manipulation were key factors in the selection. The last and most important factor was that solutions rarely go over 6% concentrations. Therefore, we assume that the characteristics and dynamics should be closely tied to those of water. This implies characteristics that are almost Newtonian in terms of fluid mechanics. Furthermore, the available literature for this formulation is quite extensive in terms of physical parameters like density, surface tension and permittivity. For the experimental part, a formulation with 4 % PVA is used. Since the focus of this project is the design and fabrication of a test bench it proposes a theoretical approach as a new method of process approximation for a complex and unique collector and high voltage assembly.

3.4 PVA properties

Playing a fundamental role in the electrospinning process, determining the solutions surface tension is the first step in the modeling process. The general tendency is that the addition of PVA tends to lower the surface tension. We can use a thermodynamic approach with the Gibbs adsorption isotherm derivative to explain the variation of the surface tension by adding PVA to water.

$$d\gamma = -\Gamma\, RT\, d(\ln a) \tag{3.5}$$

In this case, the variation of surface tension is a function of the solutes excess denoted by Γ and variation of activity coefficient$a$. This is explained by the fact that the PVA molecules remain at a higher free energy state than the surrounding water molecules that associate with themselves through h-bonding. Because of this, they tend to migrate towards the surface. This is where the weaker (activity) field of the molecules lowers the surface-free energy. The phenomenon was confirmed recently by a HD-VSFG technique (Heterodine-Detected Sum-Frequency Generation spectroscopy, Moll, C.J., et al, 2018). They found that the interfacial water signals become very small at the surface, indicating that the PVA polymer molecules completely take over at the surface, as shown in Figure 3.2.

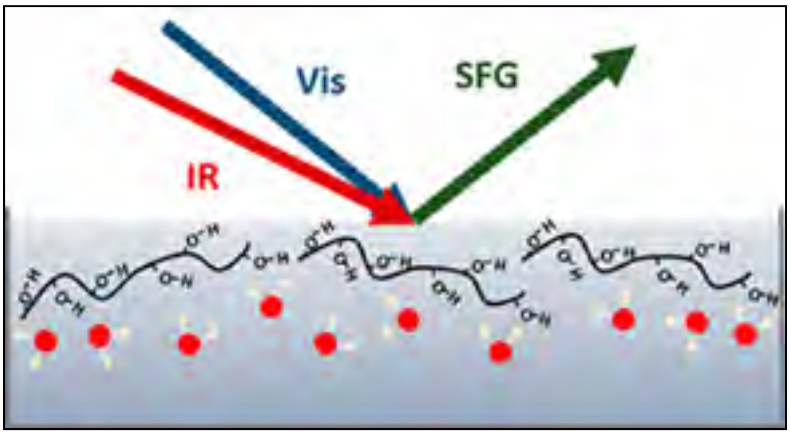

Figure 3.2: Surface structure of PVA solution in water. The interfacial surface of the solutions becomes covered by PVA molecules forming a sort of film (after Moll et al. 2018)

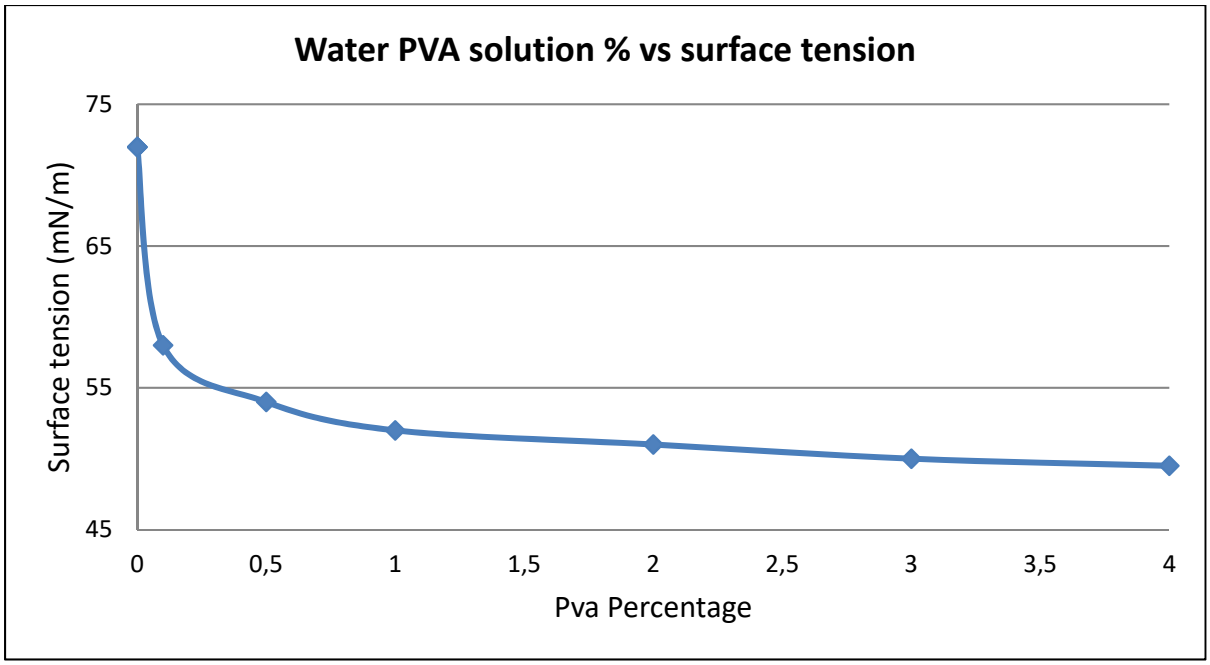

Figure 3.3 : Solution surface tension as a function of PVA concentration (after Bhattacharya, A., et al. 2004; adapted by Victor Cerda-Carvajal)

This indicates that once the air-liquid interface is fully occupied by PVA molecules, the remainder will distribute throughout the solution. It also indicates that through the evaporation of the fluid during the electrospinning process, surface tension will tend towards a stable value.

3.4.1 Solution viscosity

As mentioned previously, the fluid to be electrospun is treated as Newtonian. As a starting point, the viscosity of water is used and modified to evaluate its effect on the overall result. Literature suggest anything from 1,5 to 6 cPs in relation to molecular weight and different concentrations, our case uses an approximated value of 1.8cPs.

3.4.2 Solution density

Since very low solution concentrations are used, a very close to water density value of 1.005kg/L is used throughout.

3.4.3 Solution permittivity

Due to its high solvent fraction, 96%, the solvents (H_20) relative permittivity is usually around 80 at room temperature, the addition of PVA will tend to reduce the relative permittivity, since the solid form is around 7. The relative permittivity value is around 76 for a 4% formulation (Yeow YK et al. 2010).

3.5 Process initiation

3.5.1 Jet angle

Very little literature evaluates this key parameter in depth. Many use the default value of the Taylor cone (49,3deg) from the original paper with water as the main fluid. Just like this thesis, water solutions in very low polymeric concentrations should produce similar results.

A more in-depth analysis (Barrero et al 1999 and Subbotin et al 2015), describe the cone angle being a balance between 4 main electric forces. They are categorized into 2 groups, mobile charges and medium polarization both having radial and tangential components. Due to this, and the fluids flow, an induced current inside the cone creates a certain balance translating to a conical shape of varying angles, depending on the fluid's characteristics.

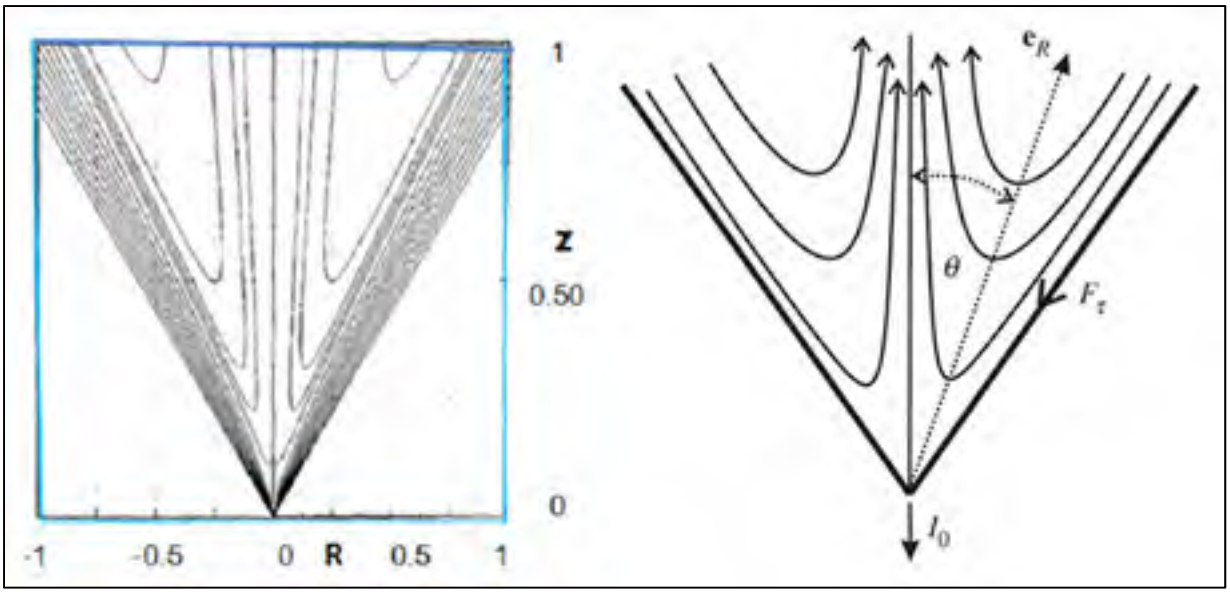

Figure 3.4 : Velocity field inside the Taylor cone. Barrero on the left with dimensionless coordinates Z, R, and Subbotin on the right.

Subottin and Semenov show some interesting results between relative permittivity and associated cone angle. The results of their calculations can be seen in Figure 3.5. It shows the relation between the cone angle and relative permittivity of the fluid taking into account different ratios of mobile surface charges on total charges w. It can be seen that a higher permittivity will have a tendency to have a Taylor cone of 49.3 deg. The higher values tend to correspond with available literature (Ramos A., et al 1994 and Li H., et al 1994). Also, of importance is the charge ratio w, the higher the amount of mobile charges at the surface, the less variable the Taylor cone angle. The red vertical line in Figure 3.5 corresponds to our experimental setup for PVA as a solution.

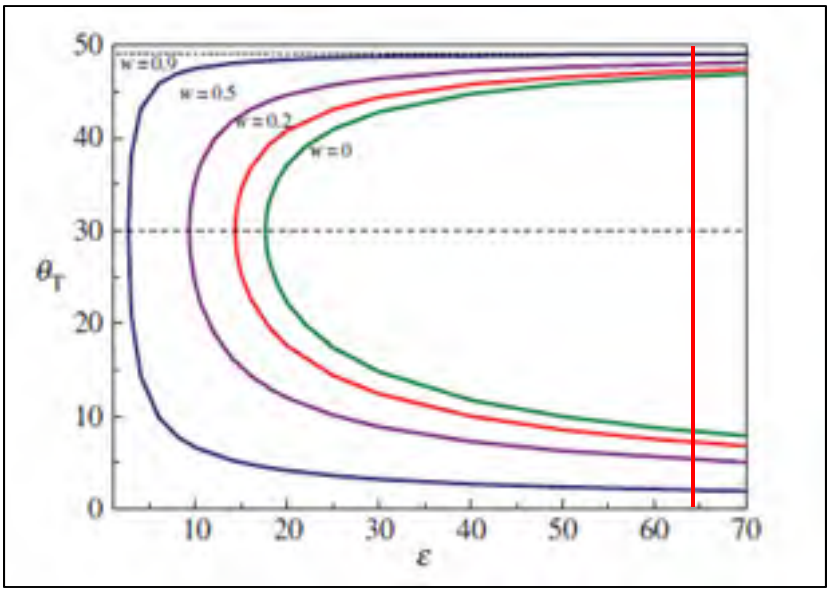

Figure 3.5 : Taylor cone angle with respect to permittivity at different mobile charge fractions (w)

Up to this point only a breakdown of the polymer solutions properties and understanding of the electric field's geometric variance was done. From here on, everything is combined in an effort to evaluate the overall process.

If we look at the process, it can be split up into 2 states, which are process initiation (Jet formation) and steady state. In the first state the available theory is sufficient to understand what needs to be considered. A good start is to evaluate what happens to the fluid from initiation to steady state in terms of geometry.

To get the best chances of properly calculating geometrical factors, before any voltage application to the process, it's important to start off by preloading the system to obtain a half droplet at the end of the dispensing needle (Figure 3.6 a)). Due to the application of the electric field, a charge density is mainly induced on the surface of the half droplet. This charge offsets the surface tension force direction and the droplet changes shape from spherical to conical (Figure 3.6). When the intensity of the electric field associated voltage (V) attains a certain critical value (Vc), the electrostatic force overcomes the surface tension of the polymer solution and forms the liquid jet from the tip of the Taylor cone. Due to the geometrical shape, at the

cone tip, the local electric field is far superior than the rest of the exposed fluid, shown later in Figure 3.7.

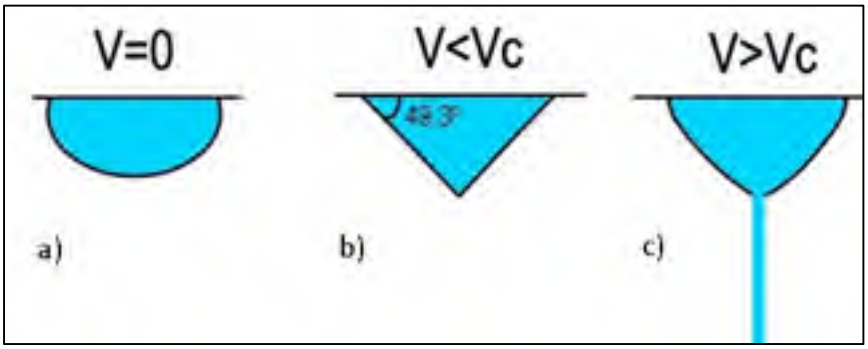

Figure 3.6 : Changes in the polymer droplet with applied voltage; a) initial shape, b) cone formation, c) jet formation (after Koombhongse S, 2001).

When the electric field is applied, the transition to a near conical shape occurs, followed by the jet formation. We can assume that the surface tension resulting force to overcome will be anywhere between $2\pi R\gamma$ (Figure 3.6 a), when V=0 and $2\pi R\gamma \cos(49{,}3)$ (Figure 3.6 c), when $V>V_c$). R being the radius of the dispensing needle and γ the surface tension. The two equations correspond to the hemisphere held by the surface tension and Taylor cone. Since the cosine of 49,3 is approximately 0.65, between the rounded shape of the fluid and the conical shape, the resulting force due to surface tension decreases by about 35%. This considered, it's important to precisely evaluate the electrostatic force that pulls on the fluid, because the shape variation will significantly change the distribution of the field over the fluid.

To simply evaluate this transition, a few electrostatic analyses were done to predict the resulting force on a fluid at different states. Note that every analysis has identical geometries and boundary conditions. These conditions being:

1) 2D axisymmetric analysis;
2) Overall containment zone of 19mm height and a radius of 10mm;
3) 22-gauge needle;
4) 3000 V potential on needle;
5) 5mm distance to a grounding plate (at the bottom of each image of Figure 3.7);

Figure 3.7 is the analysis of a hemisphere going through a parabolic shape and ending with a classic Taylor cone. Comparing each one side by side we can't notice anything too different at a large scale. Zooming each image provides a better understanding, showing that the maximum values are significantly different near the tip of each shape.

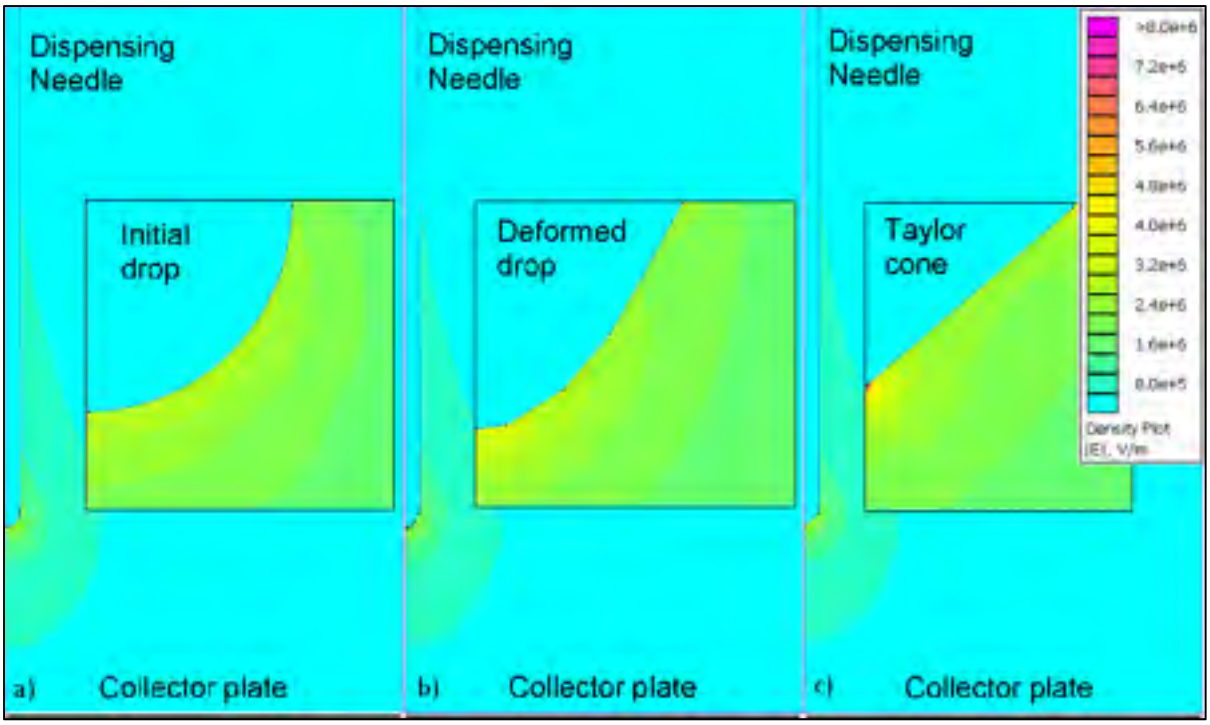

Figure 3.7 : Fluid shape evolution in electric field full scale with needle tip zoomed; a) hemispheric, b) parabolic, c)

We notice that the maximum electric field value for each case varies from $2.8 * 10^{-6}$ (V/m) for the spherical shape to $7.6 * 10^{-6}$ (V/m) for the conical one. Carefully evaluating the transition between states, it is obvious that the geometrical factor is of critical importance. The conical shape demonstrates that along the cone sides, the electric field is somewhat constant but as soon as we get close to the tip it more than doubles, creating a local separation and jet formation. A numerical electrostatic analysis can therefore be used to predict a critical voltage. Although simple cases can be carried out with the use of equation (3.1), this approach is suited for calculating complex shapes, as is the case of this thesis.

It is to be noted that this analysis was done with a non optimised meshing but fine enough for a proper qualitative analysis. Further values that are presented for the electrostatic analysis of the proposed high voltage design are reliable, useable and demonstrated experimentally.

3.6 Steady state

3.6.1 Geometry

Given the previous explanations and overall understanding of near field electrospinning, throughout the analysis, to simplify calculations, axisymmetric 2-dimensional analyses are used throughout. The shape of the jet used is conical with a 3-segment transitional chamfer between the cone and jet.

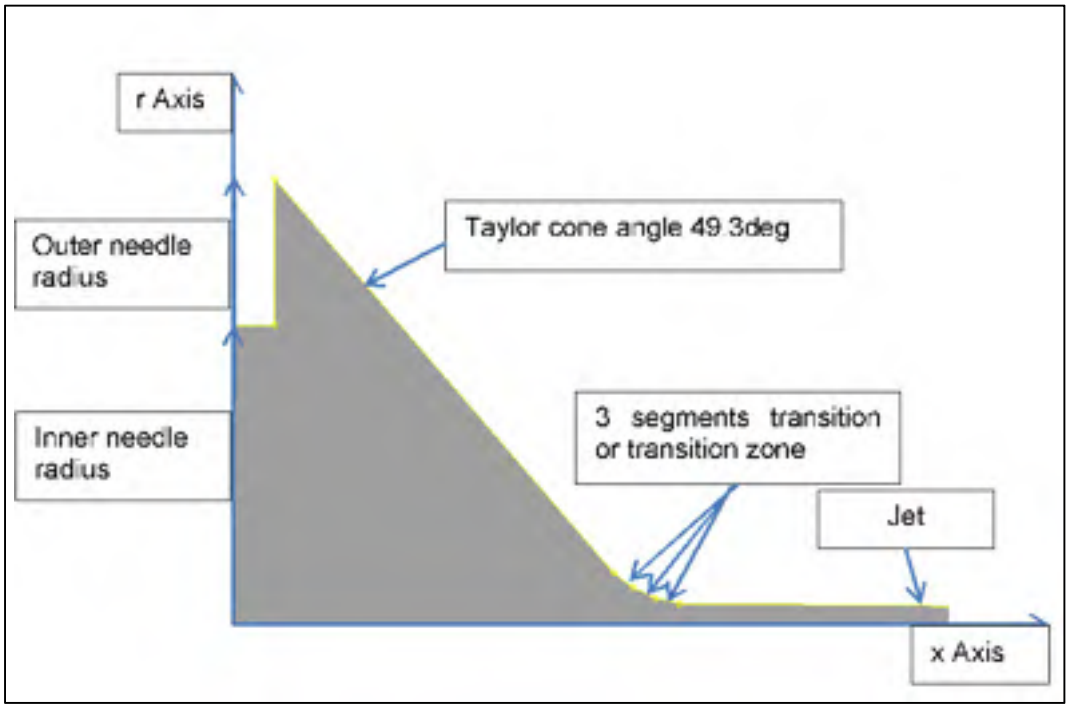

Figure 3.8 : Complete geometry of numerical models with approximated transition zone and fully formed jet

The overall shape when compared to experimental images is similar enough for a valid computational model. An evaluation of the geometric variations is done in order to evaluate

variability and the influence of changing certain parameters, namely the size of the chamfers and the jet diameter. Throughout the analysis a 22-gauge needle is used with the properties of a 4% PVA solution.

3.6.2 Main forces

In similar fashion as Taylors 1969 paper on electrically driven jets, a segmented approach is used to solve the various forces at hand. Four main forces are evaluated in this isolated analysis. Solutions do not take into account any transitions in regime due to their complex nature and it is out of the scope of this thesis. Forces will further on be named as follows: for the electrostatic pull related force ($\vec{F}_{es}$), surface tension ($\vec{F}_{\gamma 1}$), gravity ($\vec{F}_{g}$) and viscous forces ($\vec{F}_{\mu}$) (Carroll C.P. et al., 2011 and Stanger J.J., 2013).They are all combined in order to produce a starting point for machine setups. Balancing the force summation, we get the following:

$$\vec{F}_{es} = \vec{F}_{\gamma 1} + \vec{F}_{g} + \vec{F}_{\mu} + \vec{F}_{\gamma 2} \tag{3.6}$$

An additional term is added as $\vec{F}_{\gamma 2}$, although its contribution is small, the surface tension related term that holds the fiber to the collector plate is added.

3.6.3 Surface tension related forces

In our system, we previously discussed that the Taylor cone produced an angle of 49,3 degrees. As per the relative permittivity of the solution used, it is safe to assume this angle value is reliable and constant. Giving this, we get the following equation for the resulting axial force of the system:

$$\vec{F}_{\gamma 1} = 2\pi R\gamma \cos\theta_{T} \tag{3.7}$$

R denotes the outer radius of the needle size used, γ the surface tension of the solution and θ the Taylor cone angle. As for the surface tension related to the fiber that contacts the collector, it usually is within the order of the following:

$$\vec{F}_{\gamma 2} = 2\pi R_{fiber}\gamma \tag{3.8}$$

$$\frac{\vec{F}_{\gamma 2}}{\vec{F}_{\gamma 1}} = \frac{2\pi R_{fiber}}{2\pi R\cos\theta_T} = \frac{R_{fiber}}{R * 0.65} \tag{3.9}$$

Typically, some of the smallest dispensing needles are 30gauge (152 microns radius) and they are rarely used because they tend to jam due to solidification. Therefore, this case is used to estimate the contribution to the force sum. Typical polymer fibers range between 150 nm to around 2.5 μm.

$$\frac{2.5}{152 * 0.65} \approx 3\% \tag{3.10}$$

Since this value is very low and is also a rare combination (small needle large fiber), mostly because of the needle size used, it is safe to assume it is negligible. Since the calculation is straightforward and simple it is included but the evaluation confirms that its not a parameter that needs any special attention due to its low contribution.

3.6.4 Viscous forces

In Taylors original paper, this aspect was never explored since all experimental data was close to balancing via surface tension only. Since it was only explored for jet formation, steady state adds an additional parameter that is treated with some more sophisticated modeling using a computational fluid dynamics (CFD)solver (ANSYS fluent) to simulate viscous forces.

For computational simplification, a 2D axisymmetric model is used along the needle axis. A pressure-based solver with absolute velocity as well as a steady time solution is used to resolve

the Navier-Stokes equation system. In our case the general form presents itself as the following for mass conservation:

$$\frac{\partial \rho}{\partial t} + \nabla \cdot (\rho \vec{v}) = 0 \tag{3.11}$$

Where, ρ is fluid density, $\vec{v}$ the velocity, all balancing out. Given a 2D axisymmetric condition, cylindrical coordinate systems can be seen as follows, for radial components r and axial being x (Figure 3.9 and Figure 3.10):

$$\frac{\partial \rho}{\partial t} + \frac{\partial}{\partial x}(\rho v_x) + \frac{\partial}{\partial r}(\rho v_r) + \frac{\rho v_r}{r} = 0 \tag{3.12}$$

As for momentum, the general form being the following:

$$\frac{\partial}{\partial t}(\rho \vec{v}) + \nabla \cdot (\rho \vec{v} \vec{v}) = -\nabla p + \nabla \cdot (\bar{\bar{\tau}}) + \rho \vec{g} \tag{3.13}$$

Where$\vec{g}$ is the gravity term, p is pressure and $\bar{\bar{\tau}}$ the stress tensor given by the following equation:

$$\bar{\bar{\tau}} = \mu \left[(\nabla \vec{v} + \nabla \vec{v}^T) - \frac{2}{3} \nabla \cdot \vec{v} I \right] \tag{3.14}$$

μ is the viscosity and I a unit tensor. Substituting the equation system, we obtain the 2D axisymmetric equivalent:

$$\frac{\partial}{\partial t}(\rho v_x) + \frac{1}{r}\frac{\partial}{\partial x}(r\rho v_x v_x) + \frac{1}{r}\frac{\partial}{\partial r}(r\rho v_r v_x)$$
$$= -\frac{\partial p}{\partial x} + \frac{1}{r}\frac{\partial}{\partial x}\left[r\mu\left(2\frac{\partial v_x}{\partial x} - \frac{2}{3}(\nabla\cdot\vec{v})\right)\right] \quad (3.15)$$
$$+\frac{1}{r}\frac{\partial}{\partial r}\left[r\mu\left(\frac{\partial v_x}{\partial r} + \frac{\partial v_r}{\partial x}\right)\right]$$

$$\frac{\partial}{\partial t}(\rho v_r) + \frac{1}{r}\frac{\partial}{\partial x}(r\rho v_x v_r) + \frac{1}{r}\frac{\partial}{\partial r}(r\rho v_r v_r)$$
$$= -\frac{\partial p}{\partial r} + \frac{1}{r}\frac{\partial}{\partial x}\left[r\mu\left(\frac{\partial v_r}{\partial x} + \frac{\partial v_x}{\partial r}\right)\right]$$
$$+\frac{1}{r}\frac{\partial}{\partial r}\left[r\mu\left(2\frac{\partial v_x}{\partial r} + \frac{2}{3}(\nabla\cdot\vec{v})\right)\right] - 2\mu\frac{v_r}{r^2} + \frac{2}{3}\frac{u}{r}(\nabla\cdot\vec{v}) \quad (3.16)$$
$$+\rho\frac{v^2}{r}$$

Where:

$$\nabla\cdot\vec{v} = \frac{\partial v_x}{\partial x} + \frac{\partial v_r}{\partial r} + \frac{v_r}{r} \quad (3.17)$$

Solving options include a least-squared spatial discretization, solved via the SIMPLE algorithm scheme. Some hypotheses are used to set up boundary conditions. Essentially, the model is of fixed geometry, all boundaries are set zero slip conditions for anything touching the needle itself.

As for the exposed fluid (conical shape), its electrostatic analysis gives us key information. Boundary definition is related to the fluid's permittivity. As mentioned in section 3.2.4, most of the electric displacement is the medium's polarisation. Given the solutions high relative permittivity of 76, the effect of the electric field gets quickly attenuated in terms of penetration. Therefore, the majority of the electrostatic pull occurs at the skin (or surface) of the fluid, at the air-fluid interface. Analogous to the electric fields pull and without adding any complex non-linear behavior to the model, it is easier to apply a boundary condition that translates to

this effect. Since surface tension is the primary interaction at the fluids interface with air, molecules will tend to hold on to each other instead of circulating and creating vortices at the surface. Given this, we assume the fluid will travel at a constant speed at its surface separation near the cone, via the electrostatic pull in a uniform fashion. This key simplification allows us to apply a constant moving wall as boundary at the cone tip and modelled jet. Since there is a transition between the cone and jet, the model is made of 3 flat segments that approximate the transition (chamfers, Figure 3.8). Flow rate is calculated based on an evaporating model further discussed in this chapter and an approximate fiber diameter is used for this evaluation.

Using a proper model, convergence and geometric analysis in APPENDIX V, we can see that the total axial forces account for less than 2% in typical processes of low relative viscosities (close to water). Through the variation of several different parameters, we can conclude that geometrically, the transition shape (chamfer size) between the cone and the jet produce negligible differences. Input flow stability is attained with a needle length/radius ratio of 33. Fluid density variation has minimal influence on the process. Overall viscous forces can be extracted with an associated force constant that depends on boundary speed and viscosity for one dispensing needle size which in our case is a 22-gauge needle. This makes further calculations simple to integrate in the equation system with the following ($\overrightarrow{V_s} = skin\ speed\ \left[\frac{m}{s}\right];\ \mu_r = Relative\ viscosity\ to\ water$):

$$\vec{F}_{\mu} = 2.1 * 10^{-6} * \overrightarrow{V_s} * \mu_r \tag{3.18}$$

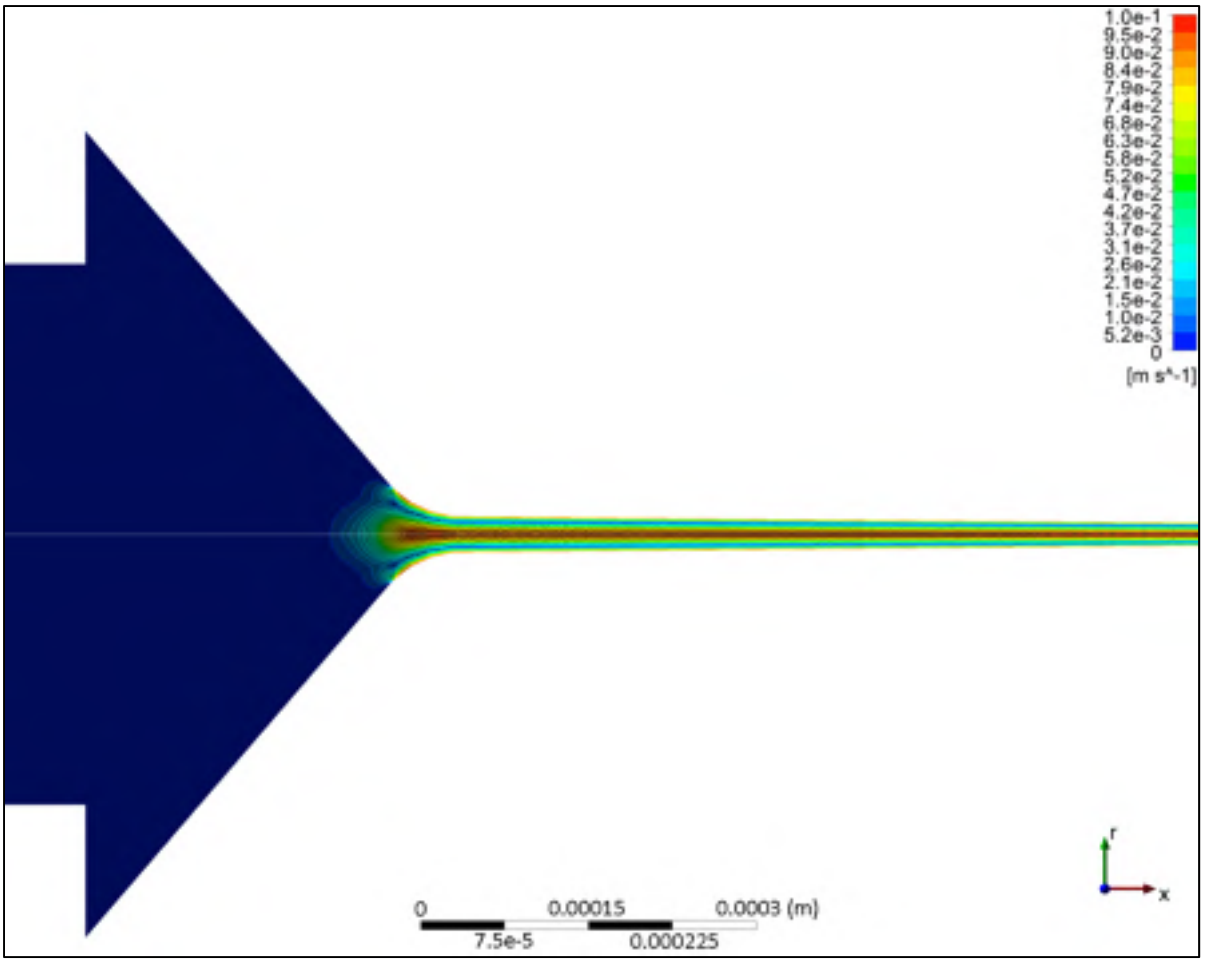

Figure 3.9 : Developed flow speed in steady state

CFD solution shows that fluid axial velocity converges at geometrical changes, which is expected. Although electrically driven fluid currents are not taken into account, given the natural fluid flow, tendency towards the fluid flow shown above is assumed. It has been shown that there exists a radial and tangential component at the surface (Taylor, 1966) that induces internal currents and they resemble to those proposed by Subbotin (Subbotin, 2018) for conical shapes featured in Figure 3.4.

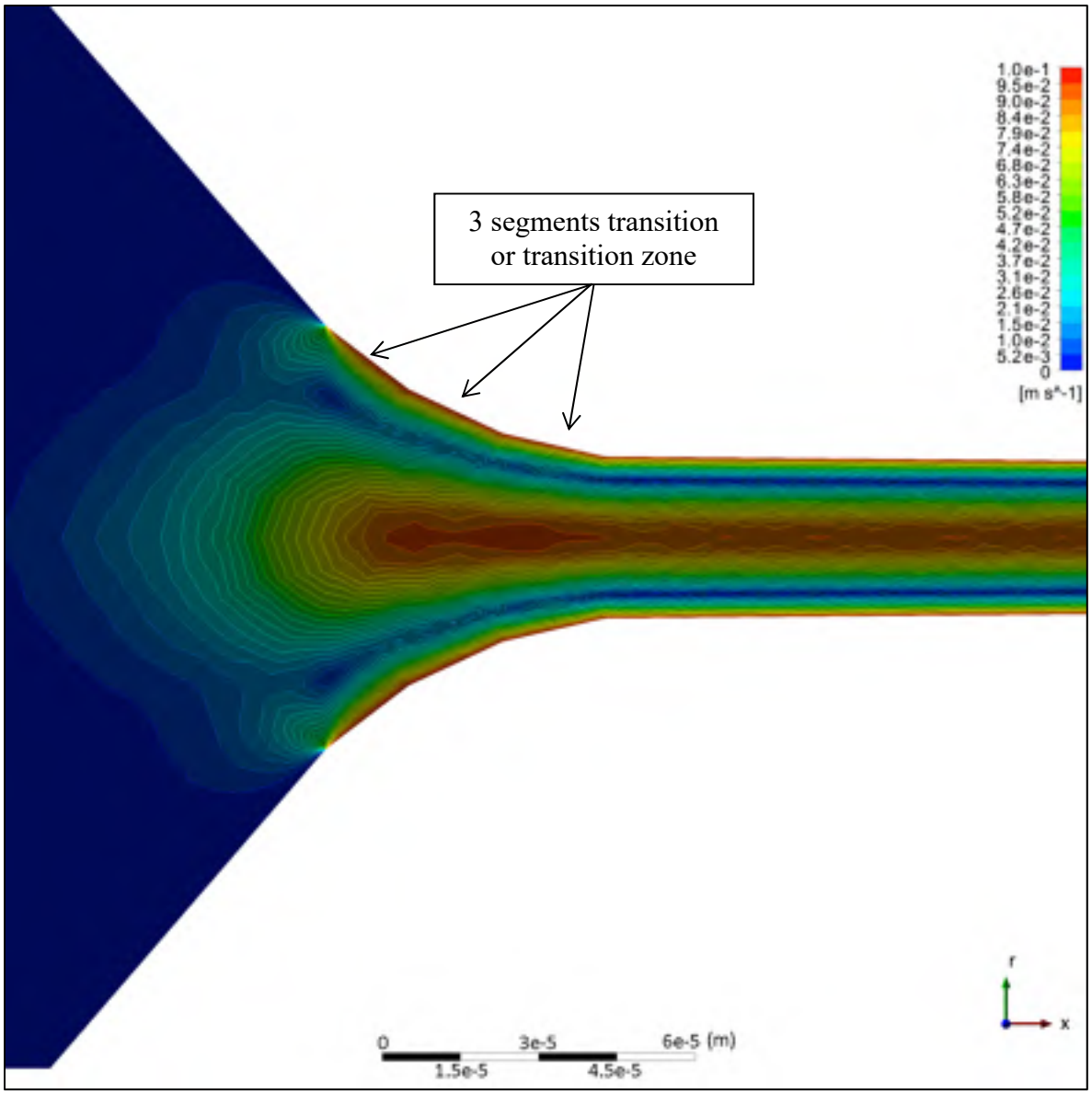

Figure 3.10 : Taylor cone and jet flow speed (Without solidification effect)

We notice in Figure 3.10, 2 separate zones were fluid velocity is high, which corresponds to the center part, near the axis, and at the surface where the fluid separates. These 2 flow regimes inside the jet portion show a very interesting phenomena where we can distinguish a Couette flow at the surface and a Poiseuille type of flow at the center. This is somewhat expected since the outer part is the electrostatic pulling force acting on the air-liquid interface. As for the center part, its the syringe pump pushing fluid to keep the steady state conditions.

3.6.5 Evaporating model

The whole idea behind near-field electrospinning is to be able to approximately capture the fiber where it solidifies or slightly after. Too close and the fiber splatters, too far we get random behavior similar to the more classical electrospinning setups with fixed collectors. In order to approximate solidification distance, a modified Langmuir equation is employed. That of which has been successfully applied for a variety of processes including evaporation to estimate mass transfer (solvent loss) (Katskov, et al. 2010, Safarian, et al. 2013, Cai et al. 2013 and Golecki, et al. 2014). We assume that the solution evaporation behaves like water due to the fact that it composed 96% of the solution. For the approximation of the model, we use standardised tabulated values of water partial pressures. There are two regions of the process where evaporation takes place: the Taylor cone and the jet.

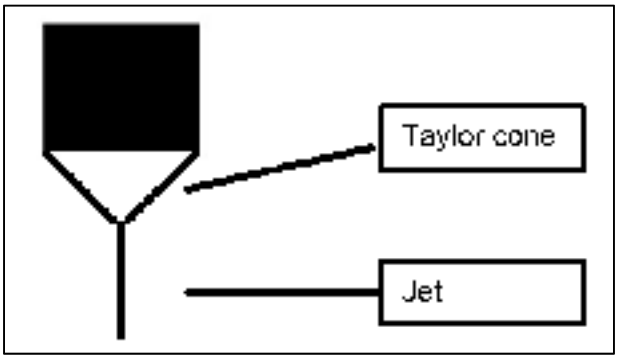

Figure 3.11: Evaporation regions of the process (cone and jet)

The taylor cone remains constant during the whole process in steady state conditions. A first calculation is made with the Langmuir equation bellow, taking a total evaporation area of the Taylor cone surface.

$$\frac{dM}{dt} = \left(P_v - P_p\right)\sqrt{\frac{m}{2\pi kT}} \tag{3.19}$$

Where dM/dt represents the flux of vapor molecules. P_v being the vapor pressure of water and P_p its partial pressure in function of relative humidity and temperature. The terms m, k and T represent respectively the molecular mass of water, Boltzmann constant and absolute temperature.

The second region is calculated by volumetric adjustment along the full length of the jet. The approach is to discretize the entire jet into varying disc sizes (Figure 3.11Figure 3.12). Every disc is subsequently reduced in size by calculating its mass loss from the previous disc, using the Langmuir equation (3.26). Exposure time is calculated by integrating the collector speed, which is the time each disc requires to travel its own thickness.

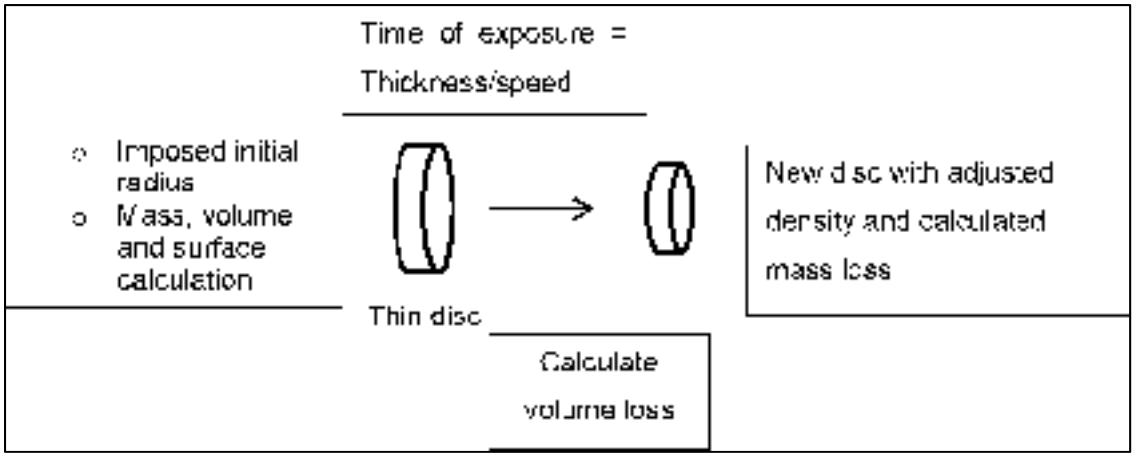

Figure 3.12 : Langmuir based evaporation model

An initial disc definition is required in the algorithm, which are disc initial thickness and radius (Figure 3.12). Disc thickness is set arbitrarily and then iterated until model convergence. The overall solidification distance is computed by summing all the thin discs. The number of discs is equivalent to the number of loops required to meet the criteria where the final disc has the no more solvent mass. This correspond to the point we reach a polymer only fiber diameter. For the initial fiber diameter, we assume a value that once evaporated gives a result similar to a diameter available in the literature. This gives a good starting point for producing solidified fibers.

After several initial diameter permutations, solidification distance changes very little. However, what really affects the distance is the temperature and relative humidity. These environmental parameters mostly affect the mass transfer rate. It must be noted that this is a particular case where the solvent used is water, other types of solution require a different approach. Using the cone size and solidification distance we can set the collector at a reasonable distance from the dispensing needle which in our case is rounded to 1 mm. See APPENDIX VII0 for algorithm.

3.6.6 Electrostatic solution

The last required element to obtain all machine parameters is balancing out the whole equation system with the only controllable external force, the electrostatic generated pulling force. The complex geometry used in this test bench design also requires numerical calculations to determine an electric potential for the power supply setup. Similar to the viscous force's CFD analysis, the model used is 2D axisymmetric. Simplified Maxwell equations are computed with an electrostatic solver and a basic triangular meshing is used. Model convergence and mesh refinement is provided in APPENDIX VI0.

Using Gauss's and Faraday's law, we use the following 2 equations in the numerical solver (E= electric field, D=electric displacement, ρ=charge density):

$$\nabla \cdot D = \rho \tag{3.20}$$

$$\nabla \times E = 0 \tag{3.21}$$

Computational simplifications include: the approximation of the electric displacement by the constitutive relationship, linearly relating the electric field to the relative permittivity ε and a scalar potential in relation to the electric field, where V= voltage field.

$$D = \varepsilon E \tag{3.22}$$

Combining the two previous equations, we can substitute into Gauss's law to produce a second order partial differential equation:

$$\nabla \cdot D = \rho \ \rightarrow -\varepsilon \nabla^2 V = \rho \tag{3.23}$$

All these equations assume that every region has homogeneous properties. Simplifications include an axisymmetric analysis and as previously stated, fixed equivalent solid geometries to mimic the fluid shape in steady state.

Two possible configurations are computed. The first (Figure 3.13), a positively charged dispensing needle with a grounded needle and ring. The second case (Figure 3.14), the grounding needle is positively charged and the dispensing needle grounded. Distance is set between the dispensing needle and glass collector to 1mm, which is the approximated solidifying distance of the polymer solution. All components are taken into account in the solver, including the collector glass where the fibers are deposited, air, aluminium outer cylinder and Delrin® isolating element.

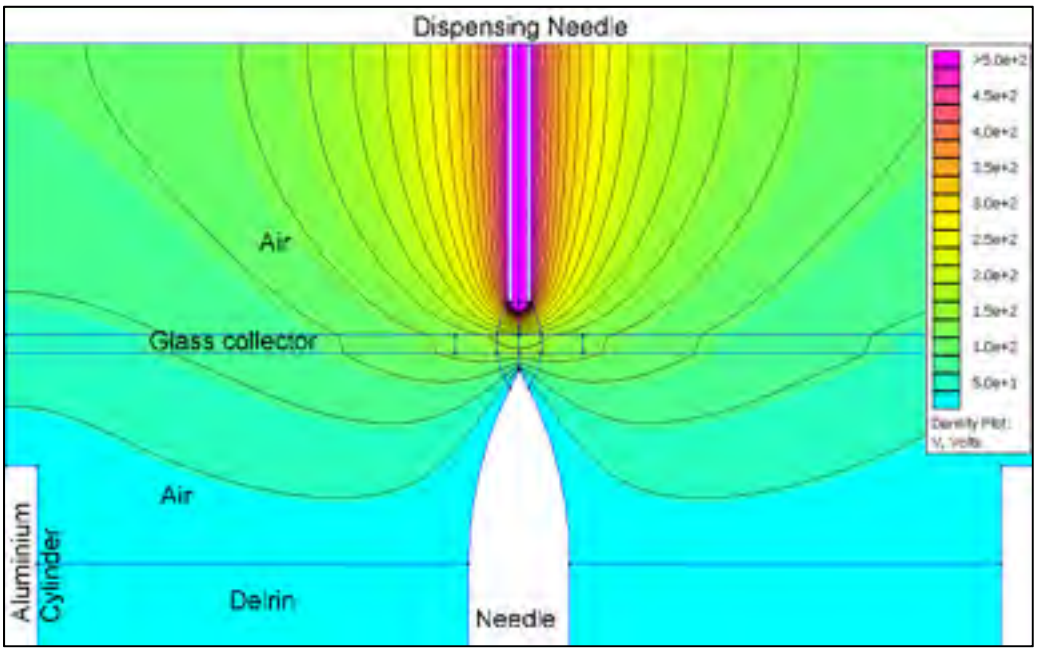

Figure 3.13: Electrostatic FEA results of the voltage distribution in the high voltage assembly (positively charged dispensing needle)

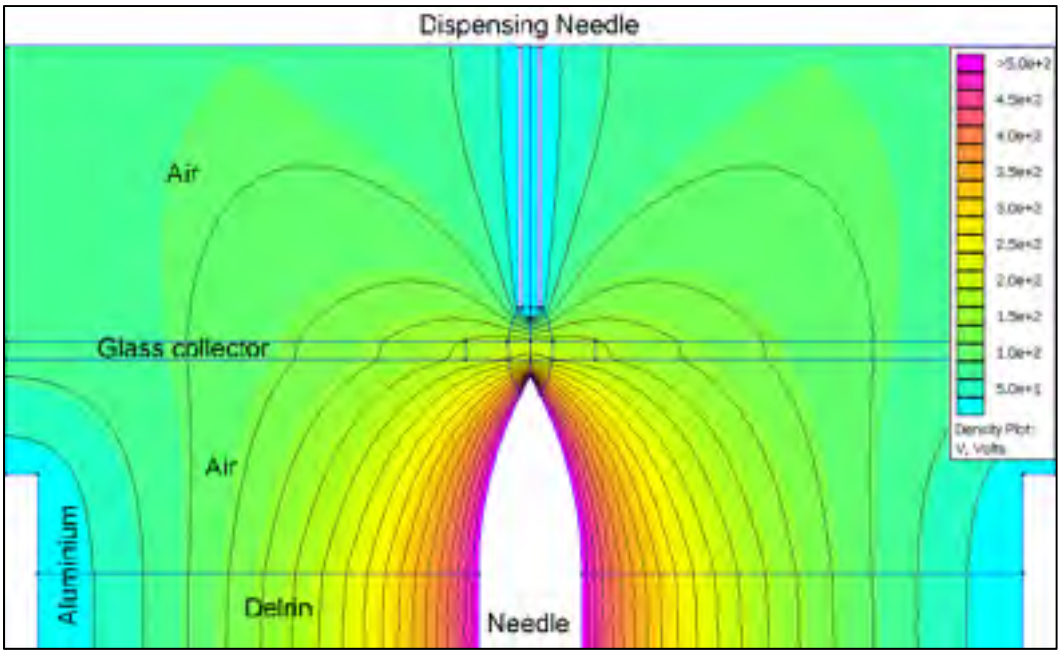

Figure 3.14: Electrostatic FEA results of the voltage distribution in the high voltage assembly (positively charged needle)

We quickly distinguish a very different voltage distribution. Other than the fact that the applied voltage is flipped between the needles, its gradient between the dispensing needle and glass collector is higher in Figure 3.13 vs Figure 3.14., approximately $4kV$ vs $2kV$ over $1mm$.

As for the resulting force, it is computed via a surface integral of the fluids exposed shape. Illustrating the localised electric field (Figure 3.15 and Figure 3.16), shows how it's locally distributed over the exposed fluid.

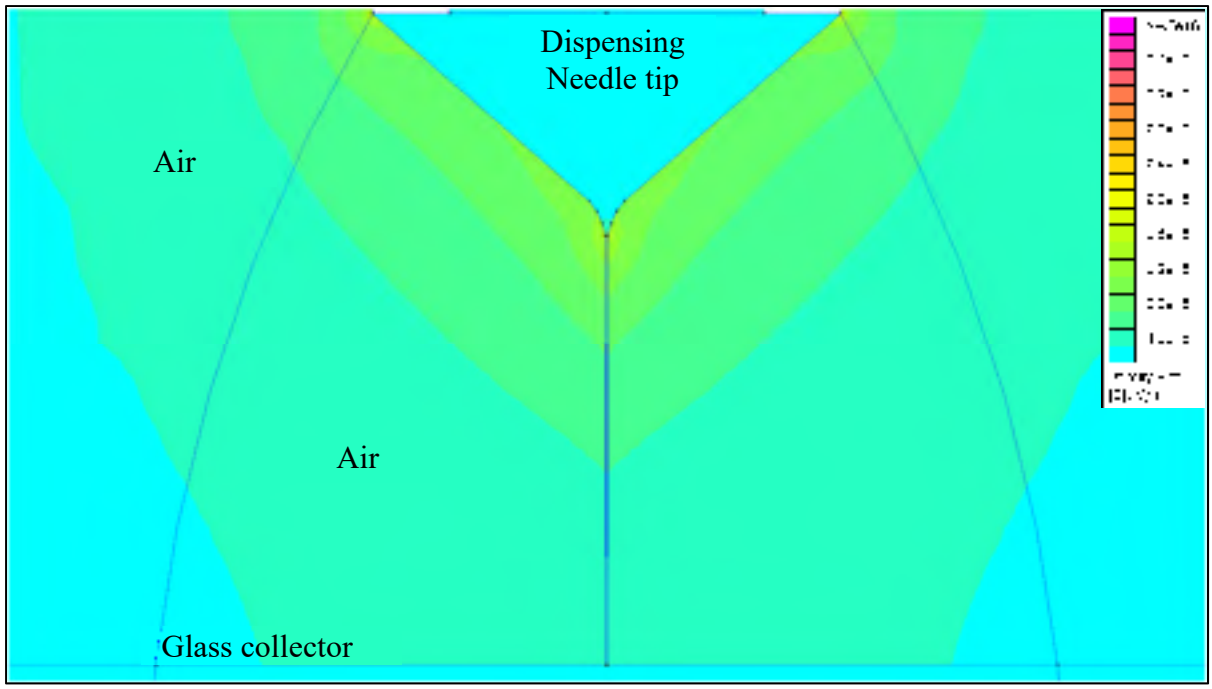

Figure 3.15 : Electrostatic FEA results of the electric field of a charged dispensing needle setup (Zoomed fluid section).

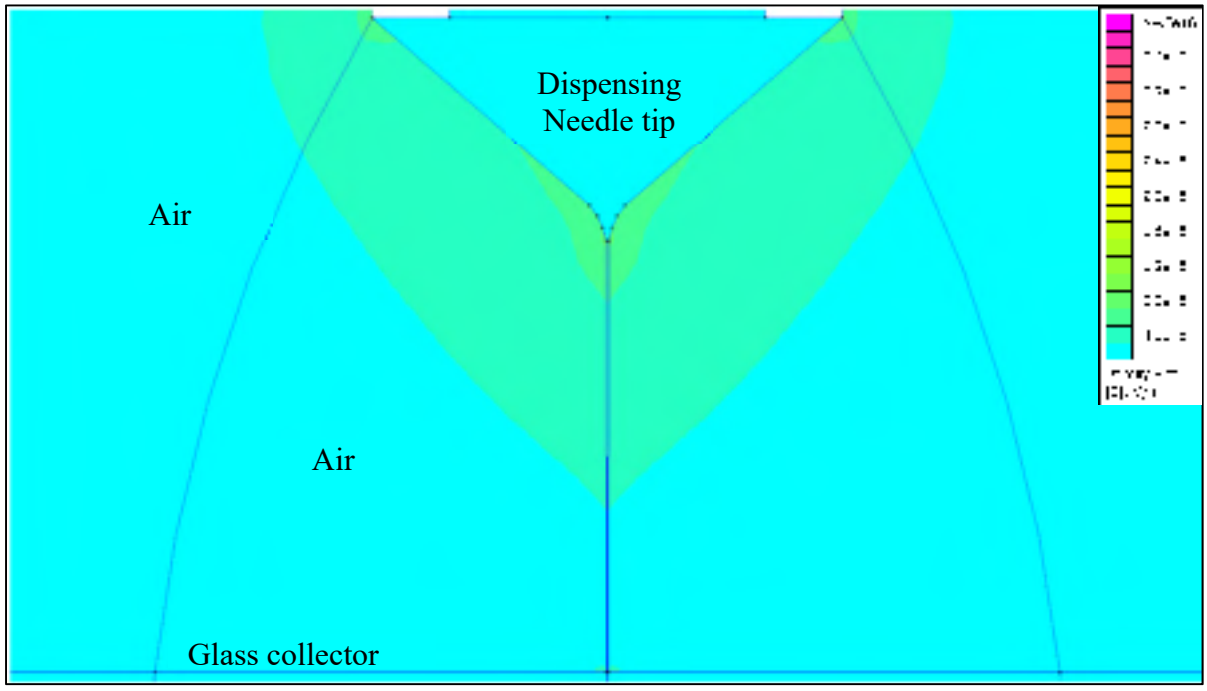

Figure 3.16 : Electrostatic FEA results of the electric field of a charged needle setup (Zoomed fluid section).

For both cases, several electrostatic solutions where generated to extract an equation that is easy to manipulate (Figure 3.17). This allows us to easily predict an associated electric field to balance out our force sum equation 3.6.

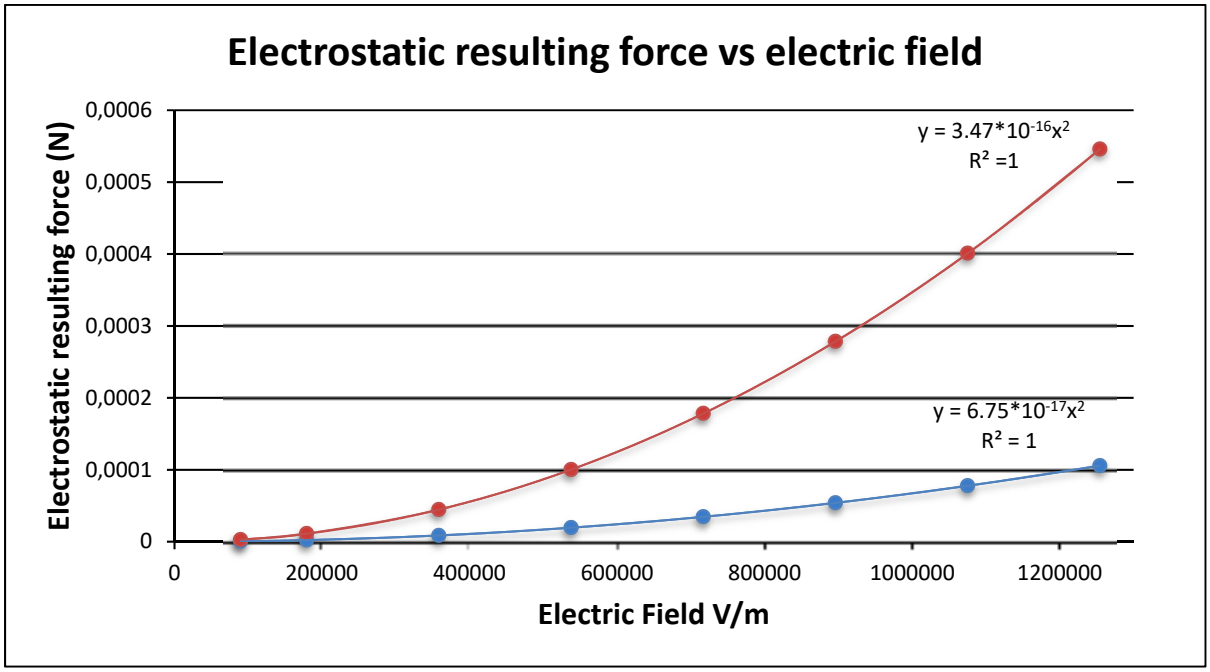

Figure 3.17 : Electrostatic pulling force in function of an applied electric field (charged dispensing needle in red (equation 3.25), charged needle in blue (3.26))

As noted in the 2 equations derived from the numerical model (3.25 and 3.26), its better to charge the dispensing needle to reduce the required voltage. ($\vec{F}_{esC}$ =electrostatic pulling force with charged dispensing needle (N), $\vec{F}_{esG}$=electrostatic pulling force with charged needle (N), $\vec{E}_f$=electric field (V/m))

Charged dispensing needle:

$$\vec{F}_{esC} = 3.47 * 10^{-16} \vec{E}_f{}^2 \tag{3.24}$$

Charged needle:

$$\vec{F}_{esG} = 6.75 * 10^{-17} \vec{E}_f{}^2 \tag{3.25}$$

It is to be noted that equation 3.6 has $\vec{F}_{es}$ as a notation for the electrostatic pulling force. All thought both $\vec{F}_{esC}$ and $\vec{F}_{esG}$ are not the same, they are interchangeable with $\vec{F}_{es}$ depending on where the applied voltage is.

CHAPTER 4

EXPERIMENTAL SETUP

4.1 Overview

Combining the previous analyses to obtain workable machine parameters, it implies further calculations to associate to a specific setup. For a quick reminder, controllable machine parameters are dispensing rates (needles and syringe sizing), process voltage, process distance and collector speed.

In order of importance, catching the fiber at the proper solidification distance is of utmost importance for near field electrospinning. Once this step is determined via the evaporation model to get an approximate collector distance, all other analysis can be combined to get voltage, collector speed and dispensing rates. The following chart puts forth in order, a simplified overview of a whole experimentation setup.

Analysis	Machine Parameter	Physical property
Evaporation	• Collector distance • Flow rate (solvent loss)	• Solution concentration
CFD	• Flow rate • Collector speed	• Viscosity • Density
Electrostatics	• Voltage	• Permittivity of mediums and electric field shape

Figure 4.1 : Machine setup overview

4.2 Machine parameters

After convergence of the solidification model, an initial value at the jet formation shows a solidification distance between 0.3 and 0.5mm. Variations depend mostly on environmental

parameters, specifically temperature and humidity. With Taylor's accepted conical angle of 49,3 deg, the conical portion is of 0,31mm length. As an approximation, 1mm is used through out the whole experimentation and analysis, this longer length is preferred to ensure the likelihood of catching a solid fiber. Although the voltage adjustment can be made during the experiment, the calculations serve as a baseline. In order to properly transfer the electrostatic solution, even if numerically solved to account for a change in medium permittivity (gorilla glass collector plate), the formulation has been adjusted for universal cases and the gorilla glass converted to an equivalent air thickness. All things considered; the following equation system can be used:

$$\vec{F}_{es} = \vec{F}_{\gamma 1} + \vec{F}_{\mu} + \vec{F}_{g} + \vec{F}_{\gamma 2} \tag{4.1}$$

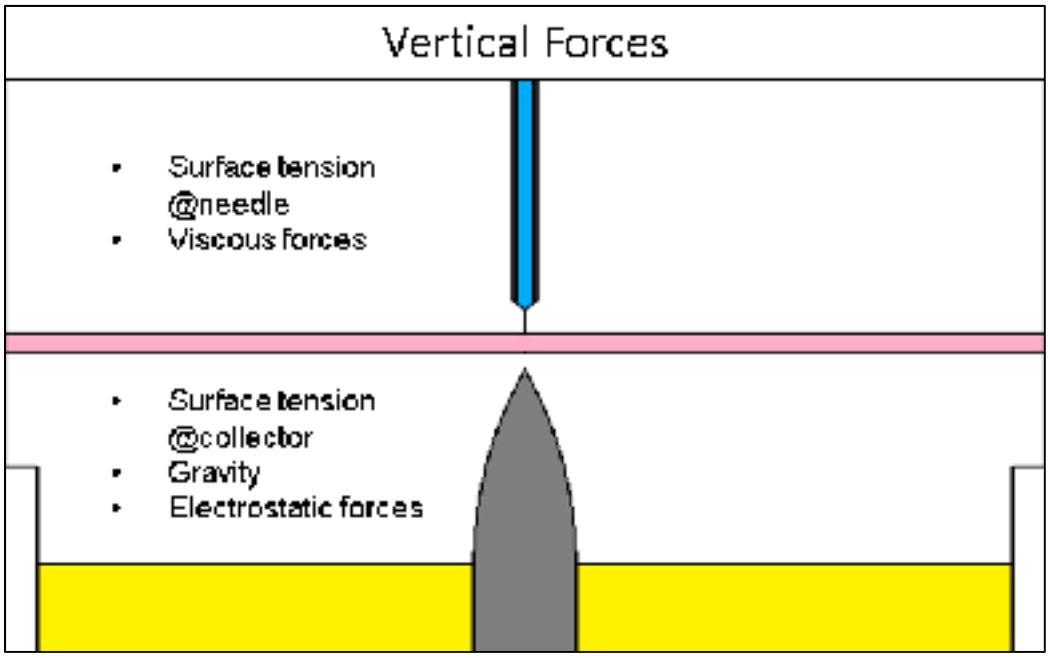

Figure 4.2 : Process forces

$$\vec{F}_{\gamma 1} = 2\pi R\gamma \cos\theta_T \tag{4.2}$$

$$\vec{F}_{g} = \pi R^2 \frac{h}{3}\rho \tag{4.3}$$

$$\vec{F}_{\mu} = 2.1 * 10^{-6}\vec{V}_s\mu_r \tag{4.4}$$

$$\vec{F}_{\gamma 2} = 2\pi R_{fiber}\gamma \tag{4.5}$$

$$\vec{F}_{es} = 3.47 * 10^{-16}\vec{E}_f{}^2 \tag{4.6}$$

$$\begin{aligned} &3.47 * 10^{-16}E_f{}^2 \\ &= 2\pi R\gamma\cos\theta_T - \pi r^2\frac{h}{3}\rho + 2.1 * 10^{-6}\vec{V}_s\mu_r - 2\pi R_{fiber}\gamma \end{aligned} \tag{4.7}$$

After measuring the thickness of the gorilla glass and setting de grounding needle to a distance of 0.5mm from de collector plate, we can now input isolate the required electric field.

$$V = D_{\varepsilon}\sqrt{\frac{2\pi\gamma\left(R\cos\theta_T - R_{fiber}\right) - \pi R^2\frac{h}{3}\rho + 2.1 * 10^{-6}\vec{V}_s\mu_r}{3.47 * 10^{-16}}} \tag{4.8}$$

Solving with the needle charged case and a collector speed of $V_s = 0.1\ m/s$, $\mu_r =$ 1.8, $\rho =$ $1.005\ kg/L$, $h =$ $0.31\ mm$, $R = 0.3556\ mm$, $R_{fiber} = 1.5 * 10^{-6}m$ and an equivalent air distance D_{ε} of $5{,}5mm$ we obtain a required voltage of approximately $2800\ V$. For the other case of using a grounded dispensing needle, it would require approximately $5700\ V$. Due to much lower voltage values, charging the dispensing needle is the setup used in the experimental phase.

The previous equation balancing provides 3 of the 4 required machine parameters which are the collector speed, process distance and process voltage. The last parameter is the flow rate of the fluid provided by the syringe pump.

Using the dispensing needle geometry coupled to the evaporation model, we can calculate the required flow rate at the needle. Syringe sizing and syringe pump setup are determined as per manufacturer recommendations for fluid flow rate.

Given the deposition speed, and initial jet diameter, the jet flow can easily be calculated, there remains the conical part that needs to be treated a little differently since it is stationary. Running the evaporation model, we get an approximate initial fiber of around 6 µm in diameter, deposition speed being 100mm/s we get an approximate flow rate of about 10 µL/h. Reusing the Langmuir evaporation equation applied to the conical surface we obtain a total rate of 1,83ml/h. We notice that the evaporation rate is much higher in the conical region given that its surface is significantly larger than the rest of the process. Although the conical evaporation rate is logically not the same as the jet and transition zone, 1ml/h is a good starting point.

4.3 Machine setup and automation

As described in chapter 2.5, the electrospinning test bench runs similar to a numerical control mill. A standardized g-code format has been implemented for controls and the following sample g-code shows a zig zag trajectory:

(ZIG ZAG);
N130 M3;
N140 G0 X-3.526 Y-5.472;
N160 G1 X13.058 F100.;
N180 Y-5.272;
N190 X-3.526;

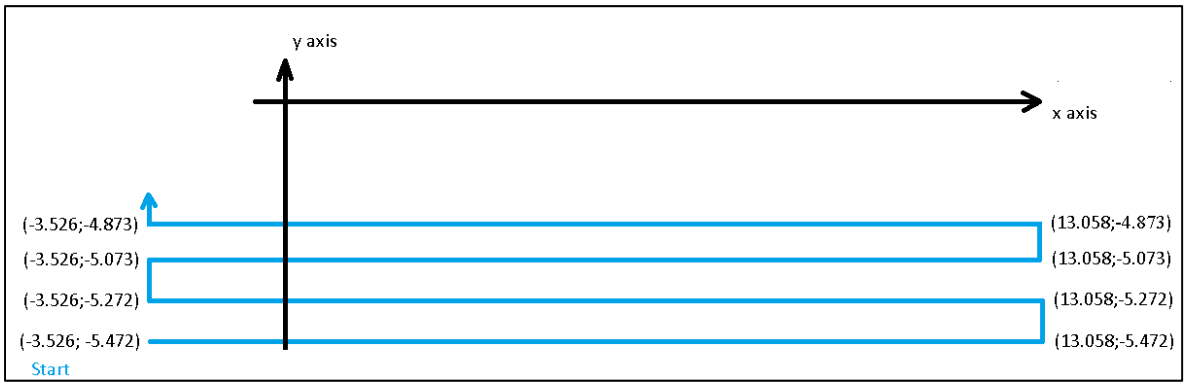

Figure 4.3 : zig zag.nc sample G-Code trajectory

As in any CNC machine it is very important to zero the machine before starting any trajectory (define origin). The depositing glass surface being very wide, zeroing the x-y axis is fairly straight forward and can be done visually depending on the deposition pattern. The most difficult setup is zeroing the z axis. Being the least precise of the axes in the whole system due to material constraints and assembly precision, a set of precision gauges are used to calibrate the height. A 1mm bloc is placed on the collector plate and the z axis limit switch is bypassed to connect the dispensing needle to the gauge bloc through a limit switch, giving a signal when the height is precisely met. A special calibration interface was developed to setup the machines coordinate system.

Accessed through its main menu, the calibration virtual instrument can be accessed as follows:

Figure 4.4 : Machine interface main page (Screwdriver and wrench are the calibration menu)

Figure 4.5 : Machine calibration virtual instrument (2 instrument page tab)

Once the calibration menu accessed, the system can be homed, faults can be reset and machine controller initialized in the homing tab (left image of Figure 4.5). Setting reference locations is done in the manual control mode tab. Enabling the x-y stages allows manual control of the machine with its remote control (Figure 2.8). Once visually placed, the x and y stages position can be reset and they now become its new zero. As for zeroing the z axis, it works the same way, the difference is that is has a zeroing mode which disables the limit switch but keeps the contact output light in use. This allows the user to set the z axis zero to the proper height without faulting the machine or stopping it because a virtual limit switch was hit. The small toggle switches on the right of these menus allow the user to jog the machine with 2 speed modes for each axis.

The next part is the fluid preload. Since the fluidic system needs to be bled to avoid air pockets that could disrupt the process, the final step is obtaining a hemisphere at the needle tip. This last step is done on the syringe pump by preloading the syringes fixing knob.

Figure 4.6 : Fluid preload, hemisphere droplet at end of dispensing needle

Once these steps are done, the g-code (sample in APPENDIX VIII) can be loaded (Figure 4.7) in the custom virtual instrument. Voltage is applied automatically with the equivalent g-code command that is coolant on or activated manually. Once the .nc file loaded, a blinking button on the remote indicates the user the push button to start the cycle. The syringe pump needs to be manually activated, but further development would allow communication with the pc to synchronise and automate the whole process.

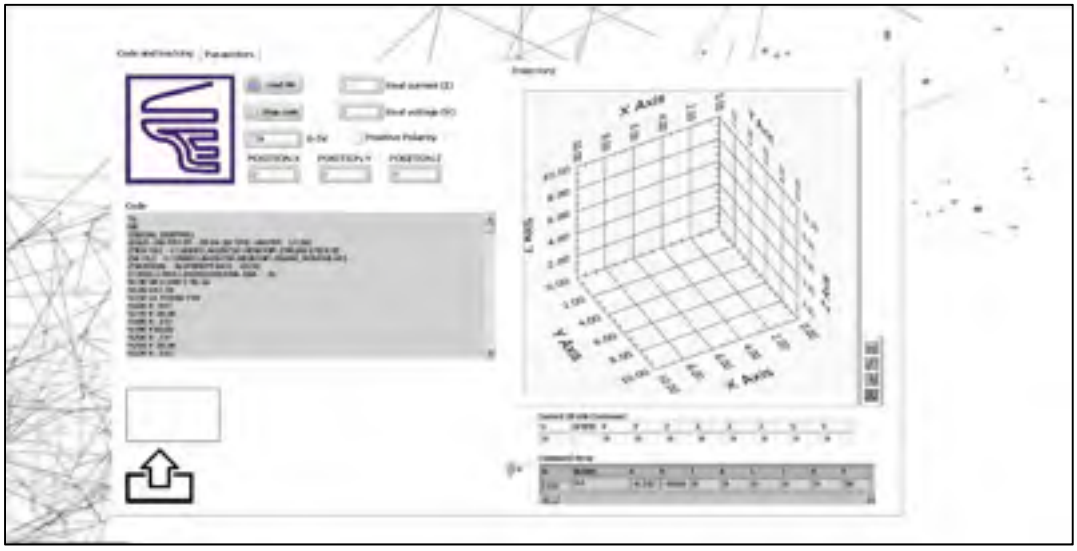

Figure 4.7 : LabVIEW virtual instrument main control page for g-code (custom virtual instrument)

The above figure is the main interface for loading and tracking the g-code that runs the machine patterns.

4.4 Results

Varying the voltage applied to the half droplet in Figure 4.6 showed a deformation of the fluid towards a conical shape around $2200\ V$ which is close to the calculated value in the proposed theoretical approach. Getting to the theoretical value of $2800V$ with all previous points covered, a rough but close enough approximation generated the following results with a repetitive zig zag square trajectory ($95\ \mu m$ spacing).

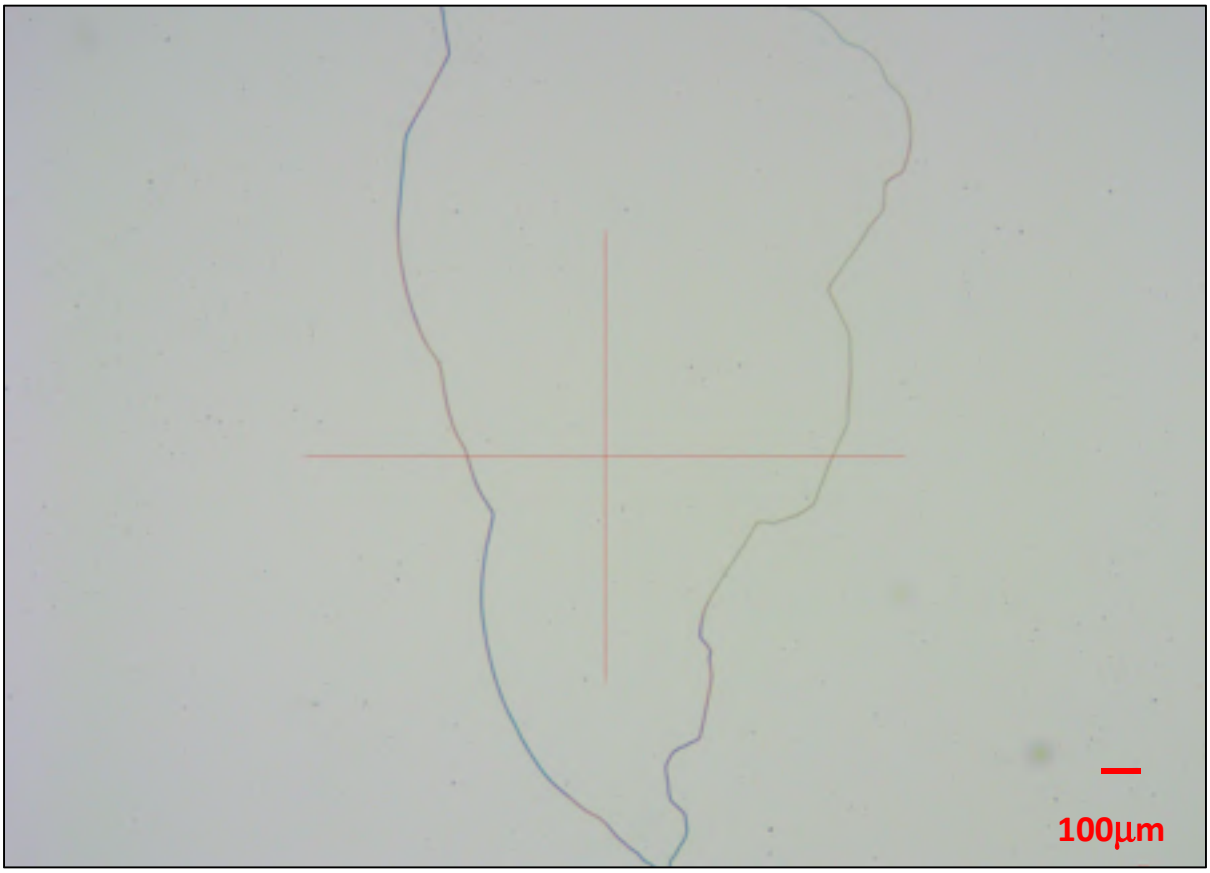

Figure 4.8 : Large fiber caught on a long displacement during initiation (40x)

The production of the large fiber in Figure 4.8 above as compared to the other images presented in this section is due to the solution that dried out for some time before initiating the process. Therefore, locally it had a higher concentration in PVA, producing a significantly thicker fiber than the next two cases.

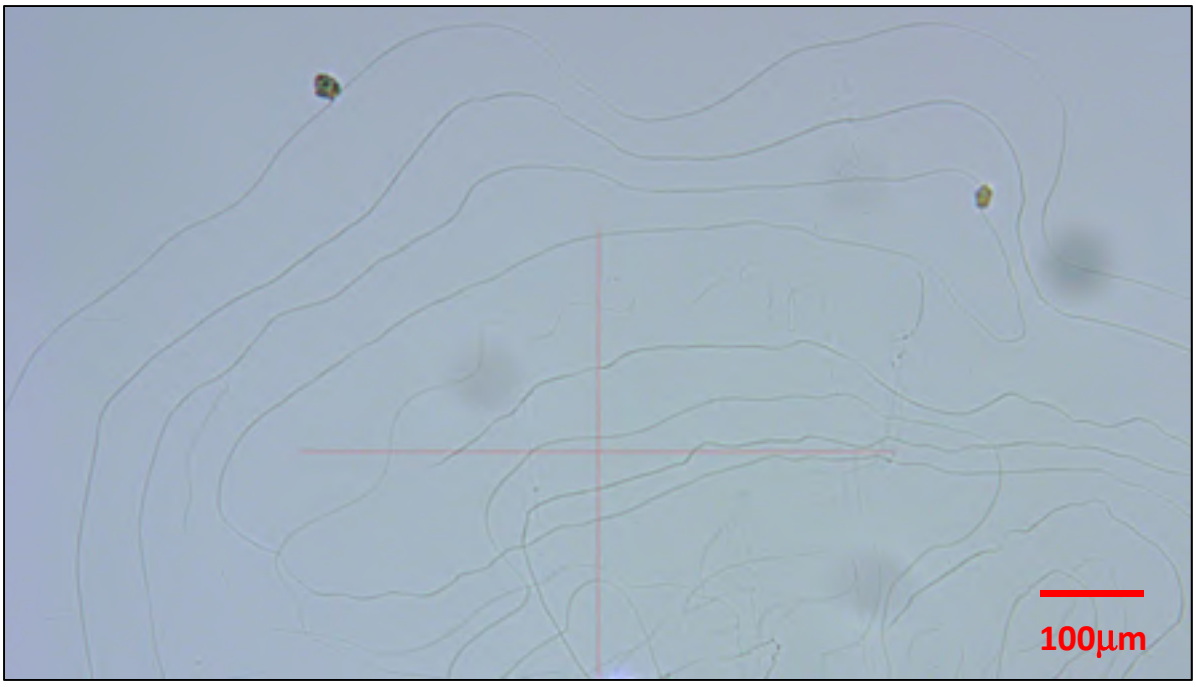

Figure 4.9 : End of a zigzag type of trajectory (100 x)

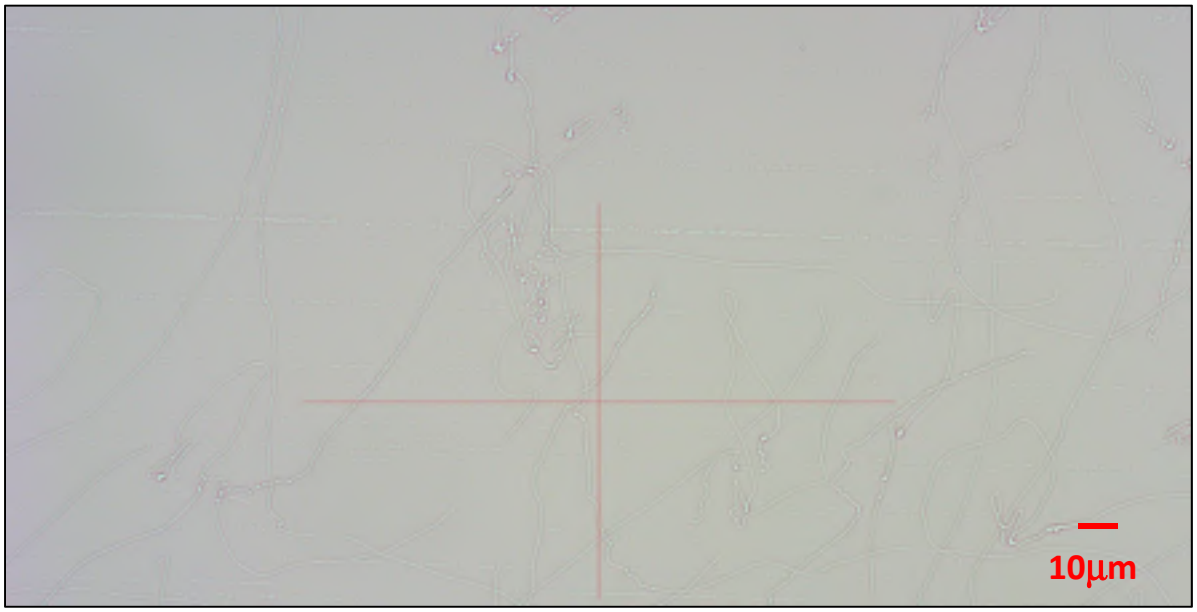

Figure 4.10 : Smallest fibers seen on sample (500x)

CONCLUSION & RECOMMENDATIONS

Overall the test bench satisfied most of the initial requirements. Although certain functionalities were not fully integrated, workarounds were used to carryout the experimental part and proof of concept. The overall design presents a robust base for future development, encompassing high quality and high precision elements for creating patterns and sub-micron sized structures. The novelty of the test bench being the high voltage design to focalise electrospun fibers, also provides a dedicated platform for electrospinning. The main goal, of being to be able to control fiber deposition, as precisely as possible, the equipment gives the end user several options to fine tune fiber production. May it be through increased voltage, to increase the electrostatic pull, adjust the collector speed or change the flow rate. All these elements were properly incorporated and although preliminary test results did not produce straight and parallel fibers, the proposed theoretical model generates useable data and fibers were produced with minimal experimental setup.

The theoretical model proposed a validated approach to machine parameter estimation with a unique CFD model that approximates viscous forces. Although the contribution of the viscous forces are very low, the modeling confirmed this assumption for near water like viscosities. However, it is important to consider viscous forces when either deposition speeds are fast or the solution viscosity is high. The results also seem to correspond with the latest developments in terms of what internal cone flow should look like. Parallel to this, the Langmuir based evaporation model provided a good estimate for the solidification distance. Even if the actual values were lower for the transition from liquid to solid, fiber production occurred. As for the electrostatic solution, FEA values also provided reliable results for the electrostatic pull. Overall the theoretical approach to solve for steady state, with equivalent solid models, was successful.

This being a proof of concept, there is much work to be done in future iterations. For a start, improving the precision and adjustment of the high voltage assembly would improve experimental repeatability. Finalizing the machine interface with added automation would

greatly reduce human manipulation errors and improve experimental efficiency. Much work is still required to identify proper deposition speeds as there is no theoretical model to estimate this value and much of the literature uses a trial and error approach.

Finally, this being a rather simple theoretical model because every physical property was considered as linear, it is not the case for several more advanced applications. This applies to almost every aspect of the theoretical model either it be non-Newtonian fluids, non homogeneous fluid electric properties and different more aggressive solvents. Once these uncertainties are solved, or using some trial and error for specific formulations, it will be possible to create functional elements and materials at submicron scales.

APPENDIX I

SIMPLE ELECTROSTATIC MODEL

The electrostatic model was done with the freeware FEMM. Using the same geometry and boundary conditions for every case in chapter 1 and chapter 2. Each one is done with the same geometry: 10mm radius, 5mm distance to collector and 22 gauge needle of 15mm length. Meshing is done with triangular elements and with a mesh size of 0.01mm for the needle and 0.5mm for the rest. The equation details and coupling are explained in section 3.6.

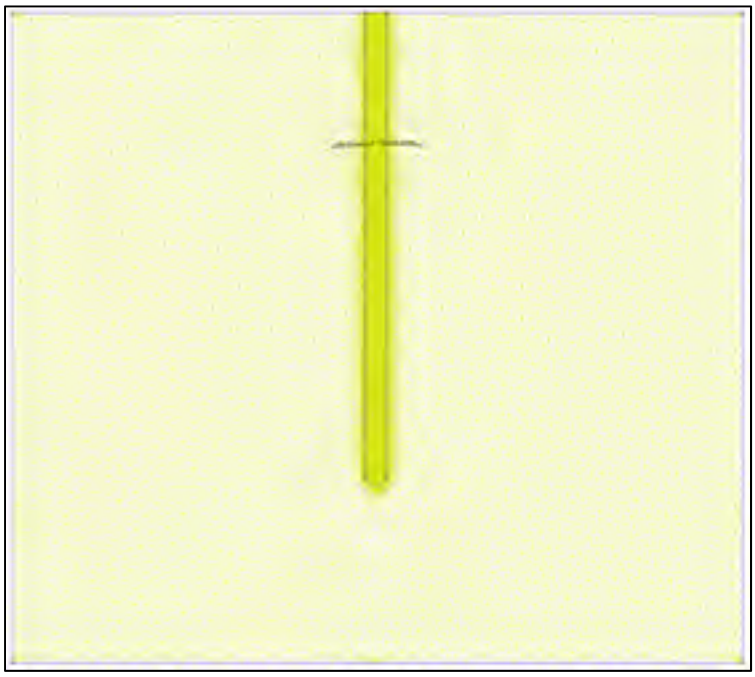

Figure AI-1: Simple electrostatic solution meshing

Boundary conditions are the lower part grounded and entire needle charged with a high voltage. Sides are considered infinitely long so that is simulates most conditions.

APPENDIX II

TEST BENCH DESIGN

Machine design consists of a granite base and modified stand that is precisely levelled on final installation. The overall machine is constructed of 3 main components which are a high precision mechanical structure, industrial grade electrical panel and pc. Overall design description for the mechanical part:

1. All mechanical elements are referenced to the granite surface.
2. Stainless steel inserts in the granite base, lie 0.1mm under surface to keep reference.
3. Bonding agent is a low sag resin.
4. Stacked x-y stage design allows for assembly flexibility but ensures stack-up is controlled. Ground surface MIC-6 aluminium is used for x-y stage components.
5. All Components above the moving collector are made of polymers to avoid electric field distortion.
6. 200mmx200mm deposition surface.
7. 400mm vertical z axis.
8. Preloaded ball screw assemblies, linear bearings and associated pillow blocs.
9. All assembled elements around the high voltage region are assembled with dielectric grease.
10. A full 1/2inch thick enclosed bell type of protection is hinged to the machine base with preloaded coils integrated in the hinges.
11. Precision components for the z axis are machined from delrin for mechanical stability and precision.

Electrical part:

1. Electronics are separated into 2 circuits to isolate motor loads from sensors and control cards.
2. 2 power supplies are used with system protection at 10A for motors and 2.5A for sensors and communication card.

3. Stepper motors are nema 17 sizing, two phases with 200 counts/rev with a parallel wiring configuration for improved high-speed torque.
4. Differential encoders are used for closed loop control (2000 lines/rev).
5. High performance drives that microstep to 52000 counts/rev were selected, with motion and resonance filtering options.
6. A national instruments interface is used to allow third party brands to communicate.
7. All signal wires are shielded and designed for high flex applications.
8. System x-y stage is protected by limit switches and home position sensors.

PC part:

1. A national instruments 4 axis control card was selected.
2. Communication parameters are pre-set with the National Instrument's measurement and automation explorer application.
3. Full s-curve motion and control is implemented in the interface.
4. All system setups are accessible and can be changed for optimised performance.
5. G-code pattern control is doable by loading a .nc file.
6. A remote control allows to jog the axis and calibrate machine.
7. Also included is an e-stop for emergency situations.
8. High voltage protection is also done by a safety switch inside le polycarbonate enclosure.

Table AII-1A: List of primary mechanical components

Component	**Description**	**Part number**
Adjustable Steel stand	4 leg steel stand	Shars SKU 303-9146
Granite base with inserts	AA lab grade 18x24 inch	Shars SKU 303-9132
Linear bearings (rail)	x-y motion	L1S15 0300 (4x)
Linear bearings (chariot)	x-y motion	LAS15CLZ (8x)
Ball screws	Preloaded 10mm x 4mm pitch	W1002FA-3P-C3Z4 (2x)
Support units	For ball screw motor end	WBK10-01A (2x)
Support units	For ball screw free end	WBK10S-01 (2x)

Table AII-1B: List of primary mechanical components

Component	**Description**	**Part number**
Motor mounts	Nema 17 interface	6061-T6 aluminium
Stage spacers	Precision machined spacers	6061-T6 aluminium
Stage platform	Precision ground plates	MIC-6 ¼ inch aluminium
Ballscrew mount	Precision machine and honed	6061-T6 aluminium
Z axis rail and chariot	Precision machined/unbent	Delrin (acetal resin)
Z axis threaded rod and nut	Linear motion z-axis	Delrin (acetal resin)

Table AII-2: List of primary electrical components

Component	**Description**	**Model**
High voltage power supply	0-50 kV reverse polarity	Bertan 210-50R
Syringe pumps	New era brand	NE-1000
National instruments Universal interface	Third party connectable 4 axis interface	UMI-7774
National instruments	PC control card 4 axis stepper	PCI-73334
Digital communication cable	High speed com for Ni PCI-7334 to UMI-7774	68-pin VHDCI
Power supply 1	60w 24VDC power supply	TDK DSP60-24
Power supply 2	150w 24VDC power supply	TDK LS150-24
Home sensor	Inductive proximity sensor	E2B-S08KS02-MC-B1
Stepper drive	High performance stepper drive, applied motion	ST5-S
Stepper motors	Steppers motors, applied motion	HT17-278-D-WAA HT17-275
Stepper encoder	Differential output 2000 lines	WAA encoder

APPENDIX III

MACHINE BASE MATERIAL AND TOLERANCE

Table AIII-1: List of machine base options (materials and description)

Material/ specs	Machineability	Flatness	Dimensional stability (°T, rigidity)	Cost for a surface of 3 sq. Ft.
Aluminium	Quick and easy, cutting tools accessible	0.020¨/12¨	Low thermal expansion, flexible, internal stresses	600$
Steel	Simple, longer cycle times	0.010¨/12¨	Low thermal expansion, rigid, internal stresses	500$
Cast iron	Good machineability, typical machine base material	Requires machining (0.005¨/12¨)	Low thermal expansion, rigid, minimal internal stresses	500$ + cost to rectify
Polymers	Fast machining	0.046¨/12¨	High thermal expansion, Very flexible. Dielectric	600$ (high density machinable)
AA grade granite surface	Difficult to modify, requires diamond like tooling	.000022¨/12	Metrology room dimensional stability. Dielectric	250$

APPENDIX IV

ACTUATOR CHOICE AND SIZING

Linear actuator evaluation:

1.Rack and pinion

Very popular in the automobile industry for steering solutions, these systems provide reliable movement at the cost of a lot of play if not precisely matted. When high precision systems are required for this type of actuator, cost escalates quickly and the overall system precision needs to be insured over the whole assembly. Precision is very good as some cnc routers are equipped with these actuators for long travel distances.

2.Timming belts

Timing belts being the most cost-effective method for linear actuators (Printers, etc) are also the least precise. Due to difficulties in fabricating belts that are reliable and also the pulleys that come along with them require a combination of factors for everything to be reliable and repeatable. First of all, the quality of the belt affects its precision (molded components). Second, they need to be under proper tension to avoid any backlash or position shifting. Although minimal, stretching and wear are issues change the systems precision over time. Finally, the quality of the pulleys and their run out is very important for repeatability and mostly for precision. This drawback is a considerable one, if the objective is to minimize positioning errors.

3. Ball screws

Very compact in design and offering a very efficient package, this is the preferred technology. Regular screw units offer low cost and a high degree of tuning, pitch and screw size. Their main drawback is play, fit and wear, all associated with fabrication tolerances. The more efficient and precise version is the ball screw, offering a wide range of pitch options for a combination of proper speed and resolution, these units provide very low friction. This

translates to a very high efficiency of around 95%. They are very expensive and the main reason for selecting them in this project was a partnership with NSK Americas. Also, if the platform was to be improved in the future, its main structure could be kept the same.

Table AIV-1: Stepper motors vs servo motors analysis

Motor technology evaluation		
Description	**stepper**	**Servomotor**
speed	0-3000 rpm	0-18000 rpm (motor specific)
Torque	Reduced torque with high speeds (typ.: 1/8torque @ 2000 rpm)	Constant until cut-off frequency
Precision	Absolute, non cumulative, closed loop possibility and position correction management	Requires high precision position feedback. Naturally oscillating position around setpoint
Movement quality	Generates vibration, each position is a pulse value (micro stepping reduces the effect)	Constant movement and fluid transitions
Cost/axis	Approx.: 500-1000$ (depending on system performance)	More than 1500$ (depending on system performance)

Motor Sizing calculations:

Pitch determined for a rotation speed of 3000 RPM.

$$Pitch = \frac{V_{Lin}}{\omega_{motor}}$$

$$Pitch = \frac{200mm/s}{3000rpm/\ 60s} = 4mm/turn$$

$$\omega_{fin} = \frac{V_{lin}}{Pitch} = \frac{200}{4} = 50\ Rps\ (314.16\ rad/s)$$

$$\alpha = \frac{\omega_{final} - \omega_0}{\Delta t} = \frac{314.16 - 0}{0.1} = 3141.6 rad/s^2$$

$$\sum T = I * \alpha$$

$$T_{mot} - T_{load} = I_{tot} * \alpha$$

$$T_{Load} = torque\ on\ screw from\ load$$

$$T_{Load} = \frac{m_{assembly} * g * \mu_{bearings} * pitch}{2 * \pi * \nu_{screw\ efficiency}}$$

$$T_{Load} = \frac{2.2 * 9.81 * 0.02 * 0.004}{2 * \pi * 0.95} = 0.000289\ Nm$$

$$I_{tot} = I_{screw} + I_{mot}$$

$$I_{screw} = \frac{0.344 * 0.006^2}{2} = 0.0000062 kgm^2$$

$$I_{tot} = 0.0000062 + 0.0000121 = 0.0000183 kgm^2$$

$$T_{mot} = I_{tot} * \alpha + T_{load}$$

$$T_{mot} = 0.0000183 * 3141.6 + 0.000289 = 0.0577\ Nm$$

Applied motion stepper motor model HT17-278, provides a maximum torque at high speed of 0.07Nm which exceeds the required 0.0577 Nm. An overall mass of 2.2 kg was used with an approximate CAD model that featured most of the final components. As the initial calculation shows, since the system has a very high efficiency, increase in mass doesn't affect the overall required torque by much (1%).

Recommended stepper drive model ST5-S was used in conjunction with the motors to provide a smooth control. Micro stepping and resonance reduction strategies were implemented in in the system.

APPENDIX V

VISCOUS FORCES

Evaluation of viscous forces is done with the ANSYS fluent solver. A 22-gauge needle geometry is used, with 0.3556 mm outer radius and 0.2413 inner radius. Conical shape is set at 49,3 degrees as discussed in chapter 3.5. Meshing is optimized in 3 sections for sizing to reduce computation without affecting results. Mesh refinement is done on: the needle, the cone and the jet. Mesh refinement convergence or divergence is validated through the overall summation of every segments equivalent axial force component.

Table AV-1: Needle mesh convergence/divergence analysis (Scientific notation E-01=*0.1)

needle mesh size (mm)	0.6	0.4	0.3	0.2	0.1	0.09	0.08	0.07	0.06	0.05	0.04	0.03	0.02
Fx tip (N)	2.67 E-07	2.67 E-07	2.67 E-07	2.67 E-07	2.67 E-07	2.67 E-07	2.67 E-07	2.67 E-07	2.67 E-07	2.67 E-07	2.67 E-07	2.67 E-07	2.67 E-07
Fx jet (N)	-5.73 E-07	-5.73 E-07	-5.33 E-07	-5.38 E-07	-6.05 E-07	-5.73 E-07	-5.67 E-07	-5.62 E-07	-5.57 E-07	-5.52 E-07	-5.47 E-07	-5.43 E-07	-6.02 E-07
Fx chamf 1 (N)	-1.05 E-08	-1.05 E-08	-1.04 E-08	-1.05 E-08	-1.05 E-08	-1.05 E-08	-1.05 E-08	-1.05 E-08	-1.05 E-08	-1.05 E-08	-1.05 E-08	-1.05 E-08	-9.88 E-09
Fx chamf 2 (N)	8.27 E-09	8.27 E-09	8.30 E-09	8.30 E-09	8.26 E-09	8.27 E-09	8.28 E-09	8.28 E-09	8.28 E-09	8.29 E-09	8.29 E-09	8.29 E-09	8.22 E-09
Fx chamf 3 (N)	1.98 E-08	1.98 E-08	1.99 E-08	1.99 E-08	1.98 E-08	1.98 E-08	1.98 E-08	1.98 E-08	1.98 E-08	1.98 E-08	1.98 E-08	1.98 E-08	2.11 E-08
Fx cone (N)	5.99 E-08	5.99 E-08	5.99 E-08	5.99 E-08	5.99 E-08	5.99 E-08	5.99 E-08	5.99 E-08	5.99 E-08	5.99 E-08	5.99 E-08	5.99 E-08	5.90 E-08
Ftot (N)	-2.2820E-07	-4.95 E-07	-4.56 E-07	-4.60 E-07	-5.27 E-07	-4.95 E-07	-4.90 E-07	-4.85 E-07	-4.80 E-07	-4.75 E-07	-4.70 E-07	-4.65 E-07	-5.24 E-07

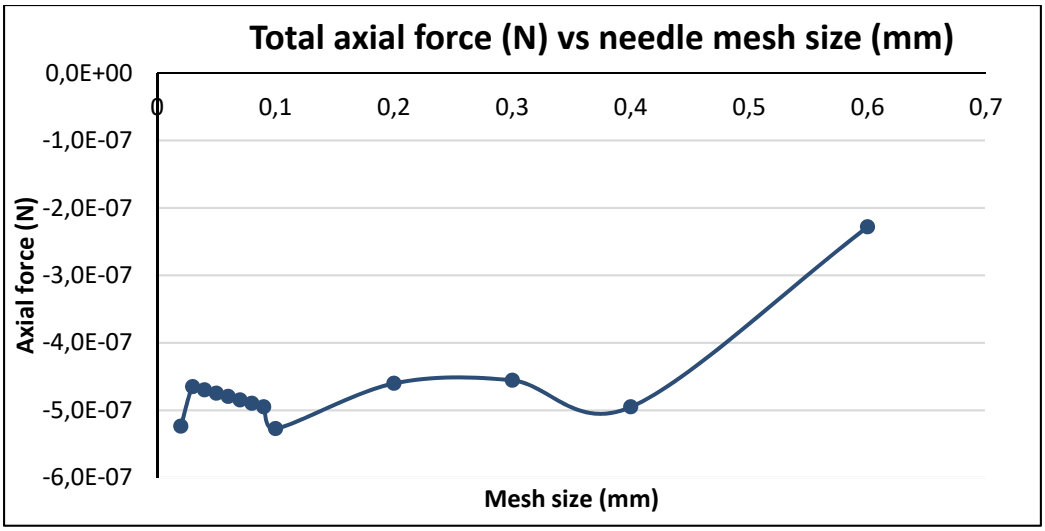

Figure AV-1: Total axial force vs needle mesh size

As a logical standpoint, representing the needle flow with a mesh size that is larger than the needles inner radius is not a good practice since it might forego local flow changes, therefore mesh size higher than 0.25mm is not representative. On the smaller side, meshing under 0.03 mm shows a beginning of divergence, stability can be seen between 0.03mm and 0.1mm.

Table AV-2: Cone mesh convergence/divergence analysis (Scientific notation E-01=*0.1)

Cone mesh size (mm)	0.01	0.008	0.006	0.004	0.002	0.001	0.0005	0.0002	0.00008
Fx tip (N)	2.62E-07	2.62E-07	2.64E-07	2.65E-07	2.67E-07	2.67E-07	2.68E-07	2.68E-07	2.68E-07
Fx jet (N)	-2.81E-06	-2.82E-06	-2.03E-06	-1.39E-06	-5.75E-07	-2.80E-07	-2.13E-07	-1.93E-07	-1.92E-07
Fxchamf 1 (N)	-1.31E-08	-1.33E-08	-1.24E-08	-1.14E-08	-1.03E-08	-9.45E-09	-1.04E-08	-1.04E-08	-1.06E-08
Fxchamf 2 (N)	8.15E-09	7.87E-09	8.18E-09	8.34E-09	7.97E-09	7.76E-09	7.70E-09	8.01E-09	6.92E-09
Fxchamf 3 (N)	2.04E-08	2.04E-08	2.08E-08	1.99E-08	2.10E-08	1.89E-08	1.79E-08	1.48E-08	1.18E-08
Fx cone (N)	3.65E-08	3.96E-08	4.37E-08	5.03E-08	5.99E-08	7.06E-08	8.17E-08	-1.72E-05	-1.97E-05
Ftot (N)	-2.76E-06	-2.76E-06	-1.97E-06	-1.33E-06	-4.96E-07	-1.93E-07	-1.16E-07	-8.57E-08	-7.53E-08

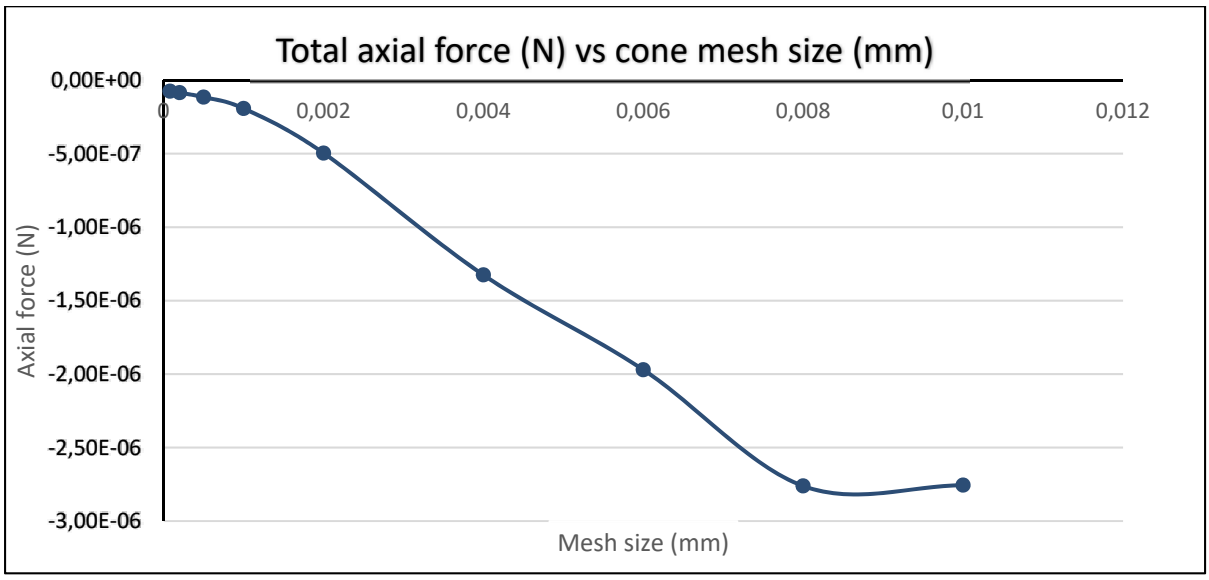

Figure AV-2: Total axial force vs cone mesh size

Comprised of a very large portion where surface flow is null, the transition zone is where most of the process occurs. Therefore, proper representation of this transition zone is important. Cone mesh represents the large portion where the droplet is only deformed, but a its transition, where the fluid breaks away, it is important to have proper representation. Therefore, a very tight meshing is required for convergence. This can be seen on the figure bellow.

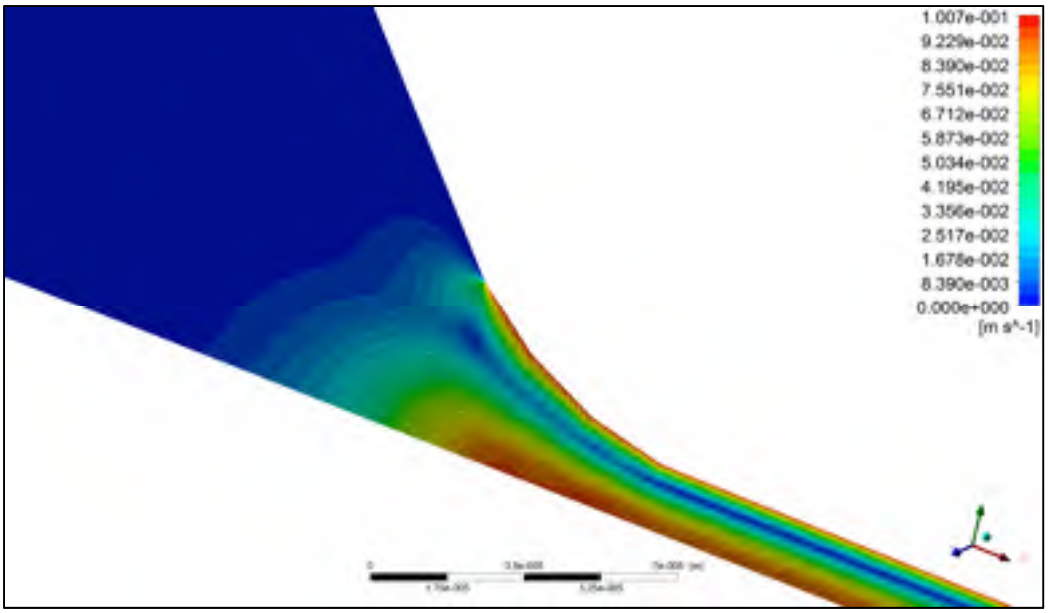

Figure AV-3: Isometric view of zoomed transition zone CFD

The results imply meshing smaller than 0.001mm.

Jet mesh:

Table AV-3: jet mesh convergence/divergence analysis (Scientific notation E-01=*0.1)

jet mesh size (mm)	0.001	0.0008	0.0006	0.0004	0.0002	0.00001	0.000005
Fx tip (N)	2.09E-07	2.26E-07	2.39E-07	2.52E-07	2.63E-07	2.66E-07	2.66E-07
Fx jet (N)	-1.34E-07	-1.52E-07	-1.65E-07	-1.76E-07	-2.01E-07	-4.19E-07	-1.57E-06
Fxchamf 1 (N)	-1.01E-08	-9.90E-09	-9.73E-09	-1.02E-08	-1.01E-08	-1.06E-08	-1.12E-08
Fxchamf 2 (N)	7.88E-09	7.85E-09	8.03E-09	7.88E-09	7.93E-09	8.24E-09	8.35E-09
Fxchamf 3 (N)	2.02E-08	2.09E-08	2.06E-08	2.02E-08	2.10E-08	2.10E-08	2.07E-08
Fx cone (N)	6.06E-08	6.06E-08	6.04E-08	6.06E-08	6.06E-08	6.04E-08	6.04E-08
Ftot (N)	-5.57E-08	-7.22E-08	-8.56E-08	-9.76E-08	-1.21E-07	-3.40E-07	-1.49E-06

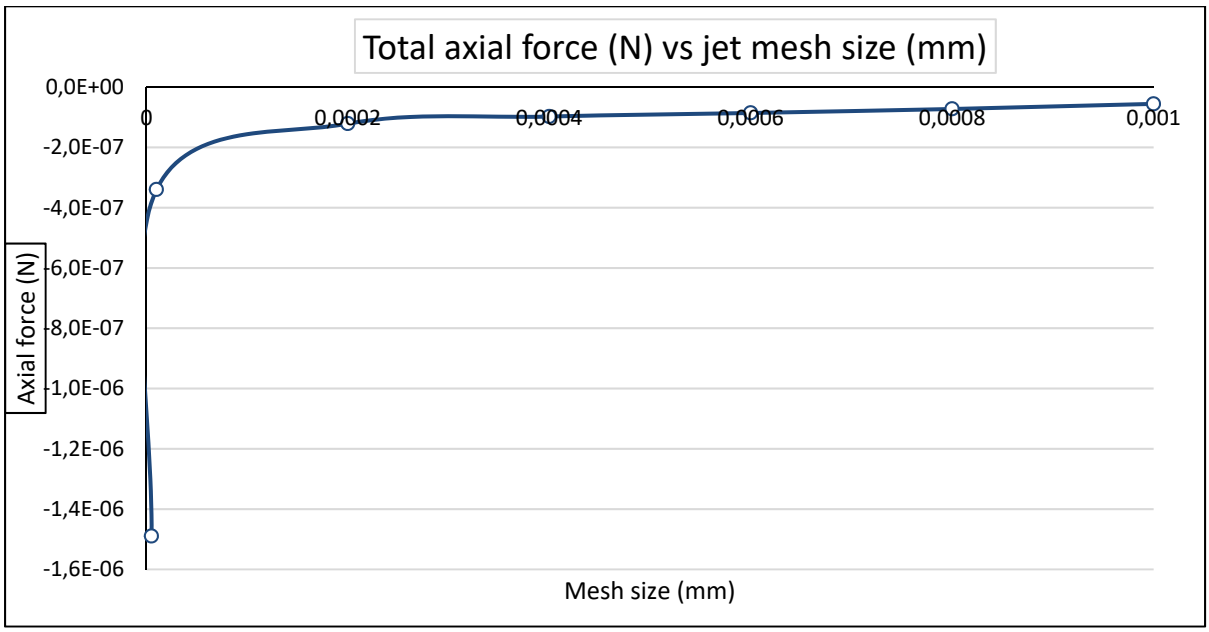

Figure AV-4: Total axial force vs jet mesh size

Divergence occurs around values of 100 nm and lower. As long as the geometry is represented by a meshing that is smaller than the fiber radius, results should be well represented while avoiding divergence.

Table AV-4: Chamfer mesh convergence/divergence analysis (Scientific notation E-01=*0.1)

chamfer length (mm)	0.9	0.8	0.7	0.6	0.5	0.4	0.3	0.2	0.1
# of chamfers	3	3	3	3	3	3	3	3	3
horizontal length (mm)	0.2407								
cone length(mm)	0.1999								
Fx tip (N)	2.65E-07	2.65E-07	2.65E-07	2.65E-07	2.65E-07	2.65E-07	2.65E-07	2.65E-07	2.66E-07
Fx jet (N)	-7.33E-07	-8.64E-07	-9.51E-07	-1.06E-06	-1.05E-06	-1.28E-06	-1.25E-06	-1.32E-06	-1.35E-06
Fxchamf 1 (N)	3.98E-08	2.92E-08	2.06E-08	1.15E-08	1.15E-08	-3.20E-09	-7.70E-09	-1.14E-08	-1.08E-08

Fxchamf 2 (N)	6.21E-08	5.86E-08	5.10E-08	4.45E-08	4.46E-08	2.78E-08	1.75E-08	8.48E-09	-9.82E-11
Fxchamf 3 (N)	-2.51E-08	-2.28E-09	2.33E-08	3.44E-08	3.45E-08	3.67E-08	3.12E-08	1.96E-08	8.05E-09
Fx cone (N)	5.11E-08	5.10E-08	5.11E-08	5.11E-08	5.11E-08	5.06E-08	5.05E-08	5.03E-08	5.03E-08
Ftot (N)	-6.05E-07	-7.28E-07	-8.05E-07	-9.22E-07	-9.07E-07	-1.17E-06	-1.16E-06	-1.25E-06	-1.30E-06

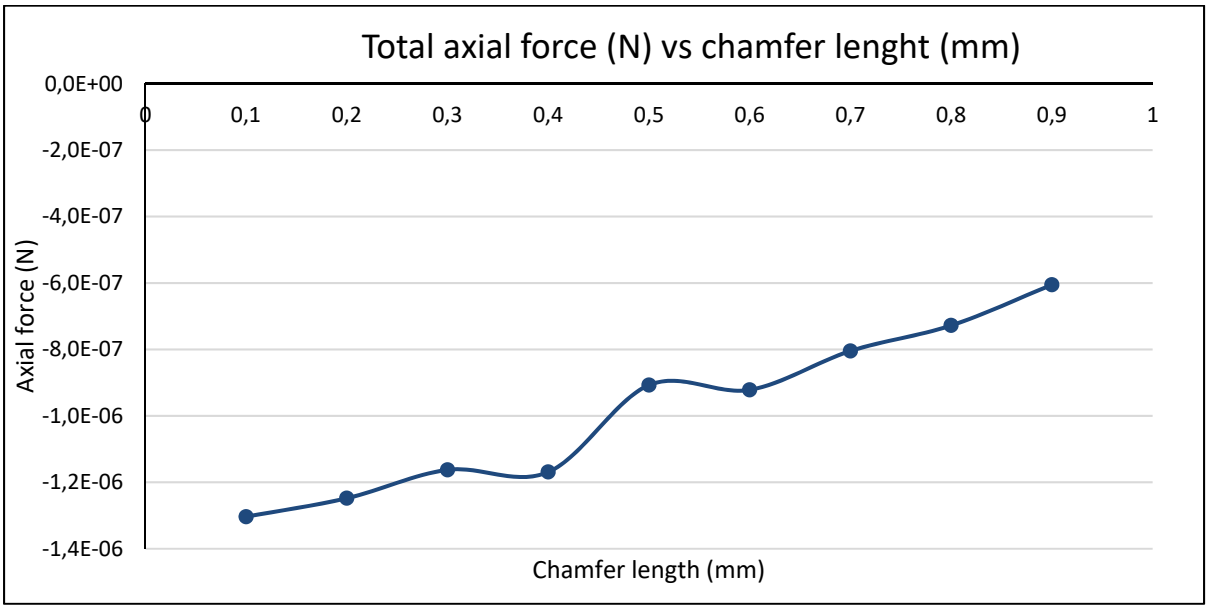

Figure AV-5: Total axial force vs chamfer length

As the scale of the graph above shows, chamfer length produces important changes. This portion is difficult to asses since real life values are very difficult to anticipate. But for the purpose of this analysis, a length that is less that 0.2mm represents an aspect ratio similar to high speed camera pictures of the process.

Jet angle and length analysis:

The process being near field, most distances will be relatively short, under 3mm. The jet angle produced, due to the fluid evaporation also has an influence on the process but are not taken

into account. The two tables bellow show the differences in variation of total axial force with respect to the jet angle.

Table AV-5: Jet length axial force variation analysis (0.5 deg, Scientific notation E-01=*0.1)

jet length (mm) 0,5 deg	1	2	3	4	5	6	7
Fx tip (N)	2.37E-07	2.63E-07	2.71E-07	2.74E-07	2.76E-07	2.77E-07	2.78E-07
Fx jet (N)	-1.96E-07	-2.01E-07	-3.44E-07	-7.45E-07	-1.29E-06	-1.91E-06	-2.65E-06
Fxchamf 1 (N)	-4.01E-10	-1.01E-08	-1.69E-08	-2.20E-08	-2.71E-08	-3.12E-08	-3.75E-08
Fxchamf 2 (N)	1.33E-08	7.93E-09	3.52E-09	8.84E-11	-5.63E-09	-1.19E-08	-1.73E-08
Fxchamf 3 (N)	2.35E-08	2.10E-08	1.72E-08	1.14E-08	5.90E-09	9.17E-10	-5.91E-09
Fx cone (N)	6.04E-08	6.06E-08	6.06E-08	6.03E-08	6.01E-08	6.03E-08	6.04E-08
Ftot (N)	-9.87E-08	-1.21E-07	-2.80E-07	-6.95E-07	-1.25E-06	-1.89E-06	-2.65E-06
variation		23%	184%	604%	1171%	1812%	2580%

Table AV-6: Jet length axial force variation analysis (0.1 deg, Scientific notation E-01=*0.1)

jet length(mm) 0,1deg	1	2	3	4	5	6	7
Fx tip (N)	6.64E-07	9.92E-07	1.12E-06	1.19E-06	1.23E-06	1.26E-06	1.28E-06
Fx jet (N)	-6.52E-07	-9.76E-07	-1.11E-06	-1.17E-06	-1.22E-06	-1.25E-06	-1.28E-06
Fxchamf 1 (N)	1.07E-08	5.18E-09	1.23E-09	-2.13E-09	-4.18E-09	-6.71E-09	-8.34E-09
Fxchamf 2 (N)	1.65E-08	1.51E-08	1.36E-08	1.29E-08	1.07E-08	9.86E-09	9.06E-09
Fxchamf 3 (N)	2.49E-08	2.28E-08	2.35E-08	2.15E-08	2.22E-08	2.06E-08	2.11E-08
Fx cone (N)	6.04E-08	6.05E-08	5.96E-08	5.95E-08	5.97E-08	6.07E-08	6.10E-08
Ftot (N)	-5.39E-07	-8.72E-07	-1.01E-06	-1.08E-06	-1.13E-06	-1.16E-06	-1.20E-06
variation		62%	87%	101%	109%	116%	122%

As the 2 tables above demonstrate, anything over the length of 2 mm will have a large influence but is very unlikely since the benefit of the process is really being close to the collector. Also, the larger the jet angle the higher the influence. The evaporation analysis estimates that most results fall in a jet angle of around 0,3deg. Also, solidification distance occurs at such a small distance that the length variation and angle should be under 1mm.

Density and viscosity and fluid surface speed:

Table AV-6: Density variation analysis (Scientific notation E-01=*0.1)

Density (g/L)	999.2	1200	1400	1600	1800	2000
Fx tip (N)	2.63E-07	2.64E-07	2.64E-07	2.64E-07	2.64E-07	2.65E-07
Fx jet (N)	-2.01E-07	-1.98E-07	-1.84E-07	-1.89E-07	-1.89E-07	-1.86E-07
Fxchamf 1 (N)	-1.01E-08	-8.43E-09	-6.69E-09	-5.00E-09	-3.51E-09	-1.89E-09
Fxchamf 2 (N)	7.93E-09	1.17E-08	1.56E-08	1.70E-08	2.28E-08	2.65E-08
Fxchamf 3 (N)	2.10E-08	2.72E-08	3.38E-08	4.20E-08	4.57E-08	5.17E-08
Fx cone (N)	6.06E-08	6.00E-08	5.92E-08	5.87E-08	5.81E-08	5.75E-08
Ftot (N)	-1.21E-07	-1.07E-07	-8.18E-08	-7.59E-08	-6.55E-08	-5.25E-08

Table AV-7: Viscosity variation analysis (Scientific notation E-01=*0.1)

Pa-s	0.001	0.002	0.004	0.008	0.25
Viscosity (cP)	1	2	4	8	250
Fx tip (N)	2.63E-07	5.26E-07	1.05E-06	2.10E-06	6.56E-05
Fx jet (N)	-2.01E-07	-4.34E-07	-9.06E-07	-1.87E-06	-5.97E-05
Fxchamf 1 (N)	-1.01E-08	-2.65E-08	-5.94E-08	-1.25E-07	-4.07E-06
Fxchamf 2 (N)	7.93E-09	-6.91E-10	-1.56E-08	-4.42E-08	-1.75E-06
Fxchamf 3 (N)	2.10E-08	1.50E-08	7.31E-09	-5.71E-09	-7.47E-07
Fx cone (N)	6.06E-08	1.22E-07	2.44E-07	4.87E-07	1.52E-05
Ftot (N)	-1.21E-07	-3.24E-07	-7.30E-07	-1.55E-06	-5.10E-05

Table AV-8: Surface speed variation analysis (Scientific notation E-01=*0.1)

Speed (m/s)	0.05	0.1	0.15	0.2
cP	8	8	8	8
Fx tip (N)	1.05E-06	2.10E-06	3.15E-06	4.20E-06
Fx jet (N)	-9.38E-07	-1.87E-06	-2.76E-06	-3.62E-06
Fxchamf 1 (N)	-6.38E-08	-1.25E-07	-1.83E-07	-2.37E-07
Fxchamf 2 (N)	-2.52E-08	-4.42E-08	-5.68E-08	-6.24E-08
Fxchamf 3 (N)	-7.62E-09	-5.71E-09	6.38E-09	2.93E-08
Fx cone (N)	2.43E-07	4.87E-07	7.31E-07	9.75E-07
Ftot (N)	-7.91E-07	-1.55E-06	-2.26E-06	-2.92E-06

Increasing density barely increases the overall results and since PVA solutions rarely go over 6% concentration, any approximation of density is sufficient and even not always necessary as the density of water can be used. As for fluid viscosity and speed, both these parameters generate linearly variable results. They both directly and proportionally affect the viscous forces. They can be treated as coefficients that can be used as relative speed and viscosity to a base speed and water respectively.

The final model to be used, has the following parameters:

Table AV-9: Final CFD analysis parameters and results (Scientific notation E-01=*0.1)

Parameters	**Value**	**Units**
Inner radius	0,0003556	m
Outer radius	0,0002413	m
Cone angle	49,3	deg
Jet length	0,5	mm
Chamfer length	0,2	mm
Density	1004.6	g/L
Viscosity	1.78	Cp
Skin speed	0,1	m/s
Jet Radius	1.63E-06	m
Rad needle inlet	0,0003556	m
Area jet	8.35E-12	m^2
Speed	0.1	m/s
Density	1004.6	kg/m^3
Flow rate	8.39E-10	kg/s
Tip	2.675e-07	N
Jet	-5.502e-07	N
Chamfer 1	-2.284e-08	N
Chamfer 1	-2.366e-08	N
Chamfer 1	-9.448e-08	N
Cone	6.024e-08	N
Total	-3.634E-07	N

APPENDIX VI

ELECTROSTATIC SOLUTION

Model convergence indicates that mesh sizing can be coarse for air and Delrin that does not surround the process or sharp geometrical changes. Full equations and coupling are detailed in 3.6.6. Mesh size is 0.0001mm for the fluid portion at the needle end and 0.01mm for a parabolic region around the process to create a transition. The rest of the process is meshed to 0.5mm. The software meshes al transitions automatically. Equivalent vertical forces are extracted with a surface integration through all the air-fluid interface.

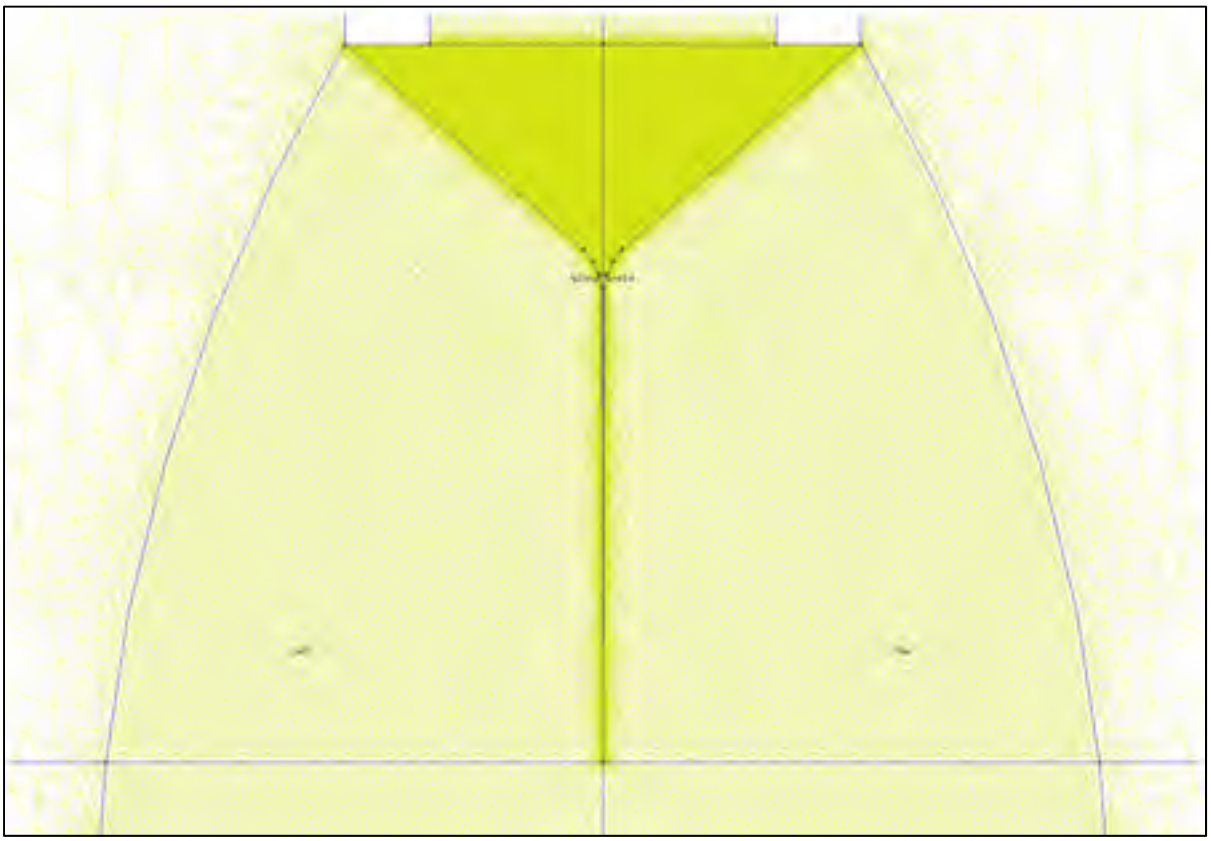

Figure AVI-1: Simple electrostatic solution meshing

Several results were computed from the electrostatic solution to get a sum of forces applied in the axial direction. The following table shows the change in electrostatic pull with respect to

the applied electric field for both cases of which either the dispensing needle is grounded or charged.

Table AVI-1: Final FEA analysis with voltage variation for 2 cases
(Scientific notation E-01=*0.1)

Applied voltage (V)	**Electric Field (V/m)**	**Force (N) (Charged dispensing needle)**	**Force (N) (grounded dispensing needle)**
500	89605.73477	5.40E-07	2.79E-06
1000	179211.4695	2.16E-06	1.11E-05
2000	358422.9391	8.64E-06	4.46E-05
3000	537634.4086	1.94E-05	1.00E-04
4000	716845.8781	3.46E-05	1.78E-04
5000	896057.3477	5.40E-05	2.79E-04
6000	1075268.817	7.78E-05	4.01E-04
7000	1254480.287	1.06E-04	5.46E-04

APPENDIX VII

EVAPORATION MODEL

Matlab script:

```
% Hertz-knudsen evaporation model to estimate fiber distance to
% Solidification. Constant rate evaporation and density readjustment
% Variable reset and initialisation
% Scientific notation E-01=*0.1
clear;
clc;
% Environmental variables
Param.rel_hum=.70;
Param.temp=20;
Param.pva_percent=0.04; %Solution
% Pressure of water saturation table in Pa, index=1 degree
Param.Psat_table=[611.213
658.593
705.973
759.7475
813.522
874.419
935.316
1004.13
1072.944
1150.5415
1228.139
1315.4605
1402.782
1500.848
```

```
1598.914
1708.8305
1818.747
1941.7085
2064.67
2201.966
2339.262
2492.282
2645.302
2815.5395
2985.777
3174.835
3363.893
3573.4915
3783.09
4015.068
4247.046];

Param.radius_ini=5E-6;%mm
Param.Length=4E-3;%mm
Param.delta=0.00001E-3;%mm
Param.R=8.3144598;
Param.speed=0.1;%m/s
Param.masse_mol=.01801528;%kg/mol(water)
Param.iter_max=round(Param.Length/Param.delta);%iters
Target_rad=300E-9; % mm
% Results structure initialisation
Results.rad=size(1,Param.iter_max);
Results.density=1;
Results.length=1;
```

```
Results.iter=1;
for ii=1:1:1000
        [ Param, Results ] = evap_calc( Param, Results );
        if Results.rad(Results.iter)<= Target_rad
           break
        end;
        Param.radius_ini=Param.radius_ini-0.01E-6;%mm;%mm
end;
%_____________________________________________________________
Function [ Param, Results ] = evap_calc( Param, Results )
Psat=Param.Psat_table(Param.temp);
ptot=(Psat-Psat*Param.rel_hum);

radius=Param.radius_ini;%mm
% density = (0.2629*pva_percent+1.002)*1000;
density = (0.2629*Param.pva_percent+1.002)*1000;
m=ptot*sqrt(Param.masse_mol/(2*pi*Param.R));
vol_ini=Param.delta*radius^2*pi;

masse_ini=vol_ini*density;
m_pva=masse_ini*Param.pva_percent;

for iter=1:1:Param.iter_max
vol_ini=Param.delta*radius^2*pi;
masse_ini=vol_ini*density;
%Surface calc
   surface=pi*radius*2*Param.delta;
   %Mass and volume calc
   masse=m*Param.masse_mol*surface*Param.delta/Param.speed;%masse en g
pva_percent_mod=m_pva/(masse_ini-masse);
```

```
%vol_perdu=masse/water_density;
   if pva_percent_mod>= 0.95
      break;
   end;
%Volume reduction
%Density increase New pva percentage
   density = (0.2629*pva_percent_mod+1.002)*1000;
vol_ini=(masse_ini-masse)/density;
%density=(masse_ini-masse)/vol_ini;
Results.rad(iter)=radius;
Results.density(iter)=density;
   radius=sqrt((vol_ini/Param.delta)/pi);
Results.iter=iter-1;
end;

% Jet angle:
Results.angle=atan((Param.radius_ini-radius)/(iter/Param.iter_max*Param.Length));
Results.length=((iter/Param.iter_max)*Param.Length);
return;


masse=mmol*surf*temps
```

APPENDIX VIII

SAMPLE G-CODE

```
O0
(ZIG ZAG)
N130 M3
N140 G0 X-3.526 Y-5.472
N160 G1 X13.058 F100.
N180 Y-5.272
N190 X-3.526
N200 Y-5.073
N210 X13.058
N220 Y-4.873
N230 X-3.526
N240 Y-4.673
N250 X13.058
N260 Y-4.474
N270 X-3.526
N280 Y-4.274
N290 X13.058
N300 Y-4.074
N310 X-3.526
N320 Y-3.875
N330 X13.058
N340 Y-3.675
N350 X-3.526
N360 Y-3.475
N370 X13.058
N380 Y-3.275
N390 X-3.526
N400 Y-3.076
N410 X13.058
N420 Y-2.876
N430 X-3.526
N440 Y-2.676
N450 X13.058
N460 Y-2.477
N470 X-3.526
N480 Y-2.277
N490 X13.058
N500 Y-2.077
N510 X-3.526
```

N520 Y-1.877
N530 X13.058
N540 Y-1.678
N550 X-3.526
N560 Y-1.478
N570 X13.058
N580 Y-1.278
N590 X-3.526
N600 Y-1.079
N610 X13.058
N620 Y-.879
N630 X-3.526
N640 Y-.679
N650 X13.058
N660 Y-.479
N670 X-3.526
N680 Y-.28
N690 X13.058
N700 Y-.08
N710 X-3.526
N720 Y.12
N730 X13.058
N740 Y.319
N750 X-3.526
N760 Y.519
N770 X13.058
N780 Y.719
N790 X-3.526
N800 Y.919
N810 X13.058
N820 Y1.118
N830 X-3.526
N840 Y1.318
N850 X13.058
N860 Y1.518
N870 X-3.526
N880 Y1.717
N890 X13.058
N900 Y1.917
N910 X-3.526
N920 Y2.117
N930 X13.058
N940 Y2.317
N950 X-3.526
N960 Y2.516

N970 X13.058
N980 Y2.716
N990 X-3.526
N1000 Y2.916
N1010 X13.058
N1020 Y3.115
N1030 X-3.526
N1040 Y3.315
N1050 X13.058
N1060 Y3.515
N1070 X-3.526
N1080 Y3.714
N1090 X13.058
N1100 Y3.914
N1110 X-3.526
N1120 Y4.114
N1130 X13.058
N1140 Y4.314
N1150 X-3.526
N1160 Y4.513
N1170 X13.058
N1180 Y4.713
N1190 X-3.526
N1200 Y4.913
N1210 X13.058
N1220 Y5.112
N1230 X-3.526
N1240 Y5.312
N1250 X13.058
N1260 Y5.512
N1270 X-3.526
N1280 Y5.712
N1290 X13.058
N1300 Y5.911
N1310 X-3.526
N1320 Y6.111
N1330 X13.058
N1340 Y6.311
N1350 X-3.526
N1360 Y6.51
N1370 X13.058
N1380 Y6.71
N1390 X-3.526
N1400 Y6.91
N1410 X13.058

```
N1420 Y7.11
N1430 X-3.526
N1440 Y7.309
N1450 X13.058
N1460 Y7.509
N1470 X-3.526
N1480 Y7.709
N1490 X13.058
N1500 M5
N1510 m30
```

APPENDIX IX

MACHINE USER GUIDE

For future reference and users, this guide shows the step by step approach to perform a successful experiment with the designed test Bench.

Once all the software configurations made, open the labVIEW project Testbench and load the electrospinning_unit.vi. This will open the main menu with all subpages and sub vi's. This will load the following interface:

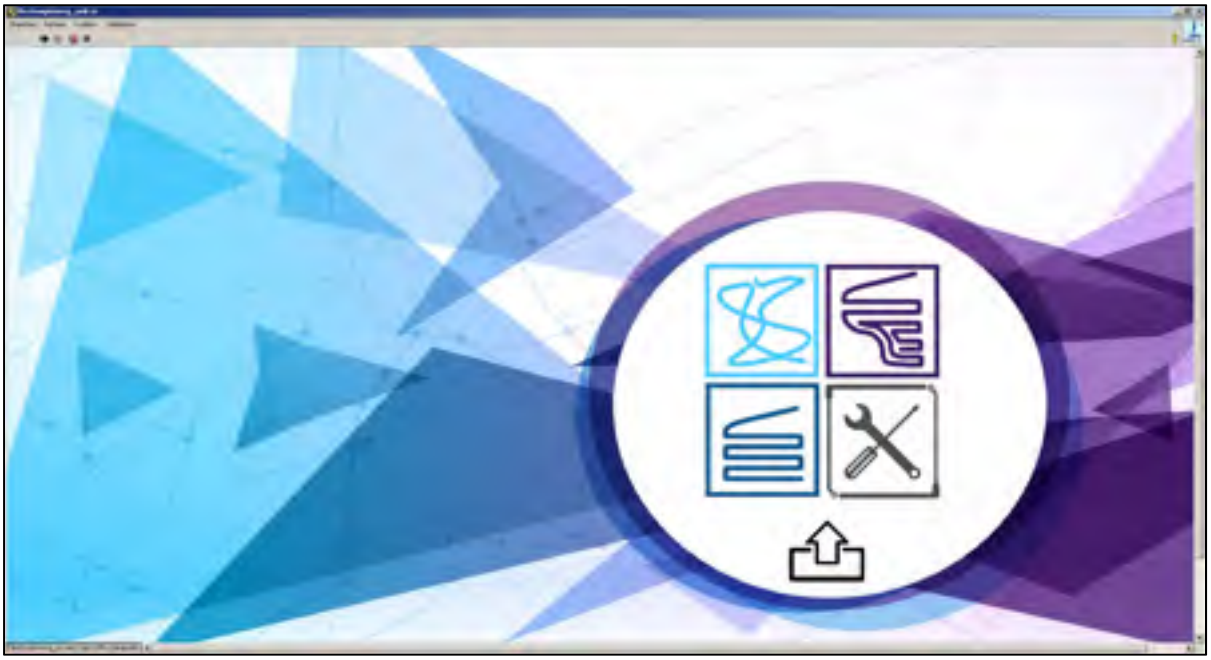

In order to successfully launch an experiment system calibration needs and initialisation needs to be done via the calibration.vi. Click on the calibration logo:

This will launch the calibration vi:

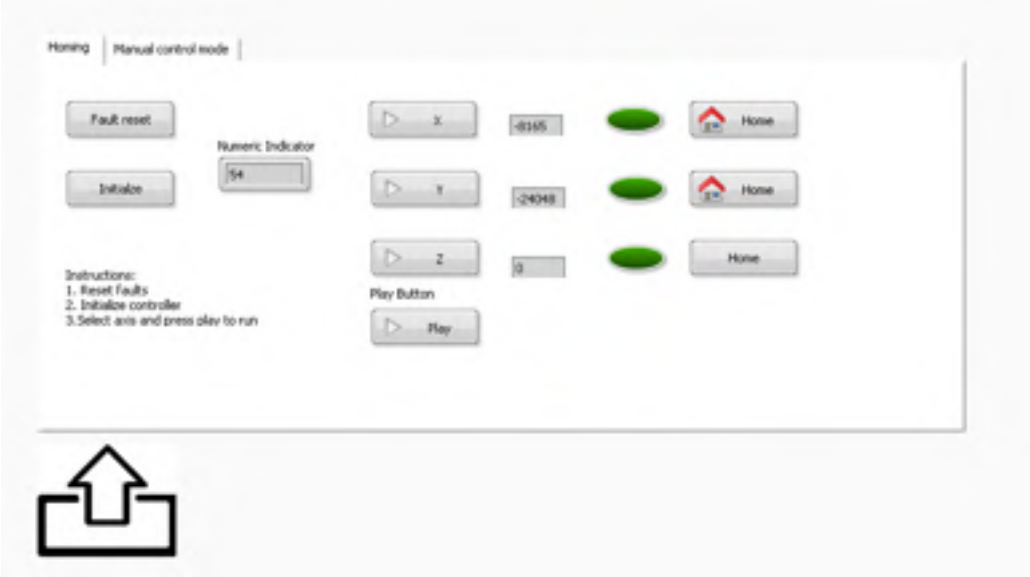

Initialise system or fault reset with buttons. Go to manual control mode to set system origin:

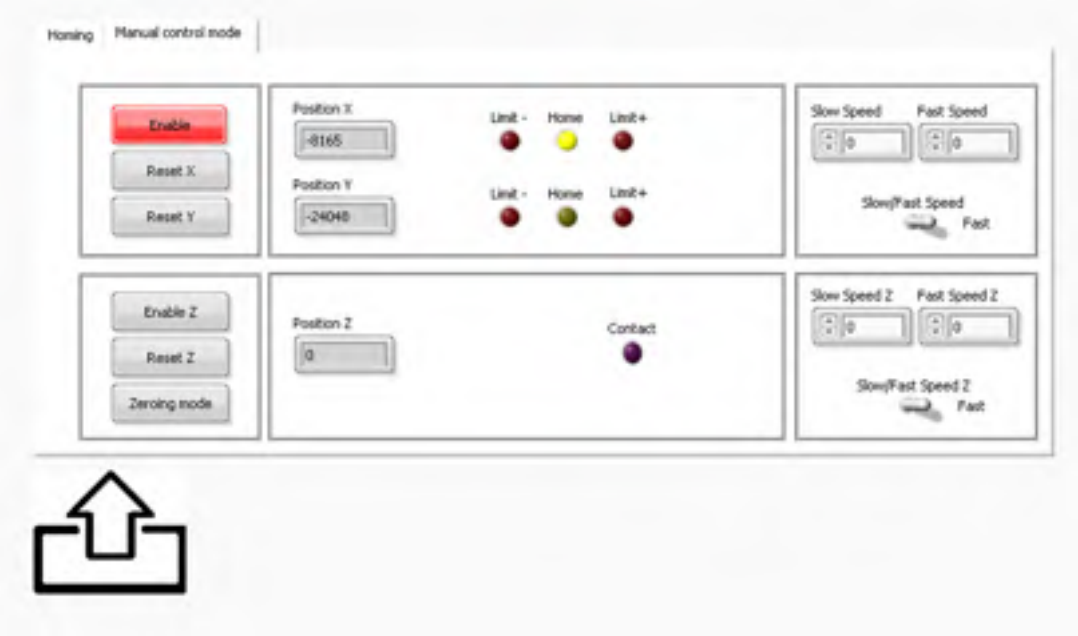

Enable axis to reset position counts. At this point, you can use the controller with text in visible orientation. Set jogging speeds in the right field and click enable to use controller to move the

axis to the desired origin. Once origin set, click the reset buttons of x and y to confirm origin. Click on enable to disable x-y drives. Repeat for Z axis, a set of shims can be used for setting desired deposition height with contact condition. If this method is used, selecting zeroing mode will enable user to bypass the z axis limit switch and use it as precise contact condition.
Once system initialized, exit sub-vi by clicking the exit logo

Once back to the main menu display, click the custom logo to load a .nc file with the desired deposition pattern:

Custom deposition vi will load:

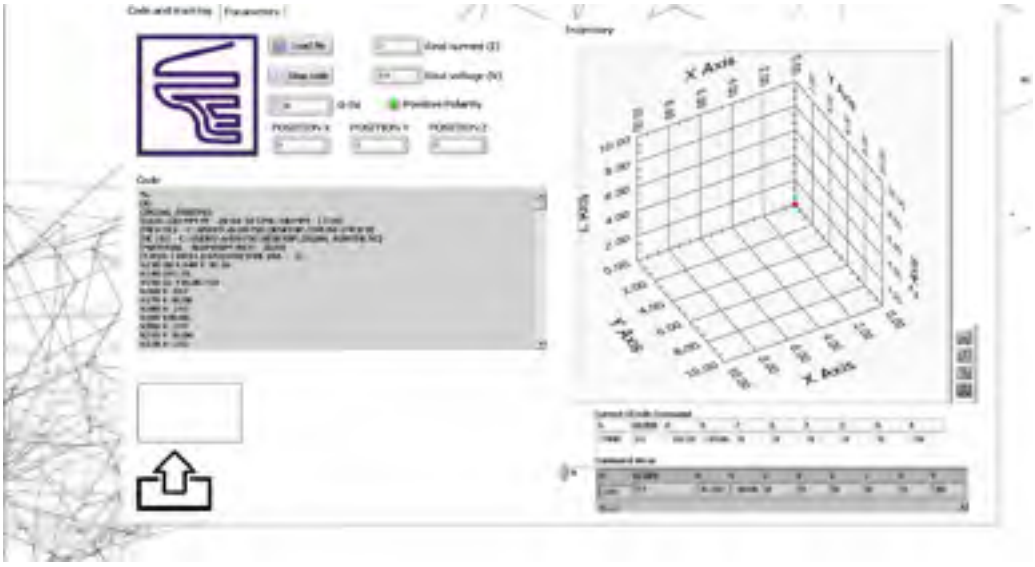

It is very important to set dynamic parameters before any pattern load. Click on the parameters tab and make sure the following parameters are filled exactly:

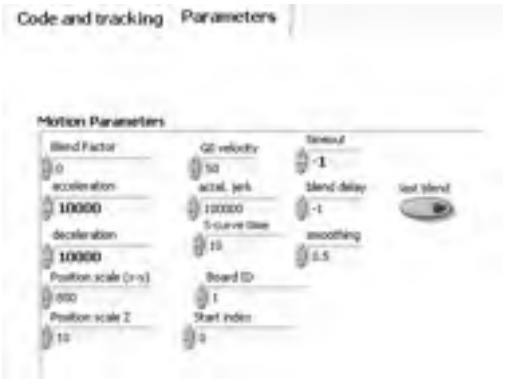

Once filled return to code and tracking tab, click on load file. Select the file and accept. Once this process done, a light will start blinking on the remote control indicating the system is waiting for the user to confirm launch. Verify that all is ok then press button and system will launch. It is the user's responsibility to start the power supply and syringe pump at the proper time.

BIBLIOGRAPHY

Atkinson, A.C., 1996, "Usefulness of Optimum Experimental Designs", Journal of the Royal Statistical Society. Series B, Vol. 58, No. 1, pp. 59-76, https://www.jstor.org/stable/2346165.

Barrero, A., Gañán-Calvo, A.M., Dávila, J., Palacios, A., and E.Gómez-González, A., 1999, The role of the electrical conductivity and viscosity on the motions inside Taylor cones, Journal of Electrostatics, Volume 47, Issues 1–2, June 1999, Pages 13-26; https://doi.org/10.1016/S0304-3886(99)00021-2

Bhattacharya, A., and Ray, P., 2004, "Studies on surface tension of poly (vinyl alcohol): Effect of concentration, temperature, and addition of chaotropic agents", Journal of Applied Polymer Science 93(1):122 – 130.

Bhattacharya, S., Lou, X., Hwang, P., Rajashankar, K.R., Wang, X., Gustafsson, J.A., Fletterick, R.J., Jacobson, R.H., and Webb, P., 2014, Structural and functional insight into TAF1-TAF7, a subcomplex of transcription factor II D. Proc. Natl. Acad. Sci. USA A 111 (25):9103-8.

Cai, Y., and Gevelber., 2013 "The effect of relative humidity and evaporation rate on electrospinning: fiber diameter and measurement for control implications", Journal of Materials Science, 48 (22) pp 7812–7826.

Carroll C.P., and Joo, Y.L. 2011 "Discretized modelling of electrically driven viscoelastic jets in the initial stage of electrospinning", J.Appl. Phy. 109 094315. Doi:10.1063/1.3582119.

Chang, C., PhD thesis 2009, DirectWrite piezoelectric nanogenerator by near-field electrospinning, University of Berkely, California.

Cooley, J.F., "Apparatus for electrically dispersing fluids". No. 692,631. Patented Feb. 4, 1902

Doshi, J., and Reneker, D.H., 1995 "Electrospinning process and applications of electrospun fibers," Journal of Electrostatics, vol. 35, no. 2-3, pp. 151–160. View at Google Scholar

Dotivala A.C., Kavya P. Puthuveetil, K.P., and Christina Tang, C., 2019, "Shear Force Fiber Spinning: Process Parameter and Polymer Solution Property Considerations", Polymers 11(2), 294; https://doi.org/10.3390/polym11020294

Electrospin Tech, "Salt Additives to improve Electrospinnability", last updated: 29 January 2019.

Fryer, C., Scharnagl, M., and Helmsa, C., 2018 "Electrostatic alignment of electrospun PEO fibers by the gap method increases individual fiber modulus in comparison to non-

aligned fibers of similar diameter", AIP Advances 8, 065023; https://doi.org/10.1063/1.5027812.

Golecki, H.M., Yuan, H., Glavin, C., Potter, B., Badrossamay, M.R., Goss, J.A., Phillips, M.D., and Parker, K.K., 2014 "Effect of Solvent Evaporation on Fiber Morphology in Rotary Jet-Spinning" Langmuir. 11; 30(44): 13369–13374. doi: 10.1021/la5023104

Guocheng Zhu, L Y Zhao, L T Zhu, X Y Deng and W L Chen. 2017. «Effect of ExperimentalParameters on Nanofiber Diameter from Electrospinning with Wire Electrodes». *InIOP Conf. Series: Materials Science and Engineering* ***230*** *(2017) 01204, International Conference on Materials Sciences and Nanomaterials*

Katskov, D.A., and Darangwa, N., 2010, "Application of Langmuir theory of evaporation to the simulation of sample vapor composition and release rate in graphite tube atomizers. Part 1. The model and calculation algorithm", Journal of Analytical Atomic Spectrometry 25(7); DOI: 10.1039/c002017f

Kiefer, J., 1986, "Optimum Experimental Designs", Journal of the Royal Statistical Society. Series B Vol. 21, No. 2, pp. 272-319, https://www.jstor.org/stable/2983802.

Koombhongseet al., Ph.D. Thesis, University of Akron, 2001, Ref. 130. Changes in the polymer droplet with applied potential, adapted from Koombhongseet al., Ph.D. Thesis, University of Akron, 2001

Lee, J.S., Choi, H.H., Ghim,H.D., and Kim, S.S., 2014, "Role of Molecular Weight of Atactic Poly(Vinyl alcohol) (PVA) in the Structure and Properties of PVA Nanofabric Prepared by Electrospinning", Journal of Applied Polymer Science 93(4):1638 – 1646; DOI: 10.1002/app.20602

Li H, Halsey TC, Lobkovsky A. 1994 Singular shape of a fluid drop in an electric or magnetic field.Europhys.Lett. 27, 575–580. (doi:10.1209/0295-5075/27/8/004)

Marcio Luis Ferreira Nascimento, Evando Santos Araújo, ErlonRabelo Cordeiro, Ariadne Helena Pequeno de Oliveira and HelinandoPequeno de Oliveira. 2015. «A Literature Investigation about Electrospinning and Nanofibers: Historical Trends, Current Status and Future Challenges», *Recent Patents on Nanotechnology*, *9,* 000-000

Moll, C.J., Meister, K., Kischner, L., and Baker, H.J., 2018, Surface structure of solution of poly (vinyl alcohol) in water, J. Phys. Chem. B122, 47. 10722-10727. doi: 10.1021/acs.jpcb.8b08374.

Nascimento, M.L.F., Araujo, E.S., Cordeiro, E.R., de Oliveira, A.H.P., and de Oliveira, H.P., 2015, "A Literature Investigation about Electrospinning and Nanofibers: Historical Trends, Current Status and Future Challenges", Recent Patents on Nanotechnology, Volume 9, Issue 2. DOI: 10.2174/1872210509021508191515 32

Pawlowski KJ, Barnes CP, Boland ED, Wnek GE, Bowlin GL "Biomedical Nanoscience: Electrospinning Basic Concepts, Applications, and Classroom Demonstration," Mater Res Soc Symp Proc 827, 17 (2004)

Pillay, V., Dott, C., Choonara, Y., E., Tyagi, C., Tomar, L., Kumar, P., du Toit, L., C., and Ndesendo, V.M.K., 2013, A Review of the Effect of Processing Variables on the Fabrication of Electrospun Nanofibers for Drug Delivery Applications, Journal of Nanomaterials, Volume 2013, Article ID 789289, 22 pages http://dx.doi.org/10.1155/2013/789289

Qin, X-H., Yang, E-L., Li.N., and Wang, S-Y., 2007, "Effect of different salts on electrospinning of polyacrylonitrile (PAN) polymer solution", Journal of Applied Polymer Science 103(6):3865 – 3870. DOI: 10.1002/app.25498

Ramos A, Castellanos A. 1994 Conical points in liquid-liquid interfaces subjected to electric or magnetic fields. Phys. Lett. A 184, 268–272. doi:10.1016/0375-9601(94)90387-5.

Robb, B., and B. Lennox, B., 2011, "The electrospinning process, conditions and control" in Electrospinning for Tissue Regeneration.

Safarian, J., and Engh, T.A., 2013, "Vacuum Evaporation of Pure Metals", Metallurgical and Materials Transactions A, 2, pp 747–753.

Short Views on Insect Biochemistry and Molecular Biology *Invited Review,* Vol.(2) 429 – 448, 2014 Chapter – 19, Application of Nanoparticles in sustainable Agriculture: Its Current Status, *ISBN: 978-1-63315-205-2*

Stanger J.J., 2013 "Experimental assessment of charge flow in electrospinning" Ph.D. Thesis, University of Canterbury.

Subbotin, V., and Semenov, N., 2015, Electrohydrodynamics of stationary cone-jet streaming, Proc. Roy. Soc., A 471 https://doi.org/10.1098/rspa.2015.0290

Taylor, G.I., 1964, "Disintegration of water drops in an electric field", Proc. Roy. Soc. Lond. A 280, 383-397, https://doi.org/10.1098/rspa.1964.0151

Taylor, G.I., 1966. "The Force Exerted by an Electric Field on a Long Cylindrical Conductor". Proc.Roy. Soc. A. 291 (1425): 145–158. doi:10.1098/rspa.1966.0085.

Taylor, G.I., 1966 "Studies in electro hydrodynamics. I. The circulation produced in a drop by an electric field", Proc. Roy. Soc., A 291 (1425) pp. 159-166. https://doi.org/10.1098/rspa.1966.0086

Taylor G.I., 1969, "Electrically driven jets", Proc. R. Soc. Lond. A 313 (1515), 453-447. doi:10.1098/rspa.1969.0205. JSTOR 2416488.

Yeow, Y.K., Abbas, Z., Khalid Kaida, K., and Rahm, M. Z.A., 2010, Improved Dielectric Model for Polyvinyl Alcohol-Water Hydrogel at Microwave Frequencies, American Journal of Applied Sciences 7 (2): 270-276.

Zander, N.E, 2013, "Hierarchically Structured Electrospun Fibers", Polymers 5(1):19-44, OI: 10.3390/polym5010019

Zheng, J-Y., Zhuang, M-F., Yu, Z-J., and Zheng, G., 2014, The Effect of Surfactants on the Diameter and Morphology of Electrospun Ultrafine Nanofiber, Journal of Nanomaterials, 2014(6):1-9: DOI: 10.1155/2014/689298

Zhu, G., Zhao, L.Y., Zhu, L.T., Deng, X.Y., and W L Chen, W.L., 2017. "Effect of Experimental Parameters on Nanofiber Diameter from Electrospinning with Wire Electrodes". In IOP Conf. Ser.: Mater. Sci. Eng. 230 012043